https://doi.org/10.1016/j.mser.2020.100578

Recent Progress in Group III-Nitride Nanostructures: from Materials to Applications

Fei Chen,[1,2] Xiaohong Ji,[1,*] Shu Ping Lau[3,*]

[1] *School of Materials Science and Engineering, State Key Laboratory of Luminescent Materials and Devices, and Institute of Optical Communication Materials, South China University of Technology, Guangzhou 510641, China*

[2] *College of Materials and Environmental Engineering, Hangzhou Dianzi University, Hangzhou 310018, China*

[3] *Department of Applied Physics, The Hong Kong Polytechnic University, Hong Kong, China*

ABSTRACT: Group-III-nitride semiconductors, including AlN, GaN, InN and their ternary, quaternary compounds, are promising electronic and optoelectronic materials for the applications in light emitting diodes, lasers, field emitters, photodetectors, artificial photosynthesis, and solar cells. Owing to their direct bandgaps ranging from near infra-red to deep ultraviolet. In recent years, the growth of group-III nitride nanostructures has been extensively explored. Herein, we provide a comprehensive review on the rational synthesis, fundamental properties and promising applications of group-III nitride nanostructures. Group-III nitride nanostructures with diverse morphologies, their corresponding synthesis methods and formation mechanisms involved are systematically compared and discussed, as well as the detailed factors that influence the optical and electrical properties of the nanostructures. The recent achievements gained in the fields of III-nitride nanostructures are highlighted, including light emitting diodes, laser diodes, photodetectors, solar cells, artificial photocatalysis, nanosensors, and nanogenerators. Finally, some perspectives and outlook on the future developments of III-nitride nanostructures are commented.

Keywords: III-nitride semiductors; nanostructures; GaN; InN; AlN; synthesis methods; optoelectronic applications.

*) Corresponding authors : jxhong@scut.edu.cn (XH Ji); apsplau@polyu.edu.hk (SP Lau)

Nomenclature

AlN	aluminium nitride
GaN	gallium nitride
InN	indium nitride
AlGaN	aluminium gallium nitride
InGaN	indium gallium nitride
AlInN	aluminium indium nitride
LED	light emitting diode
LD	laser emitting diode
PD	photodetectors
UV	ultraviolet
DUV	deep ultraviolet
IR	infrared
NIR	near infrared
FE	field emission
1D	one dimensional
2D	two dimensional
3D	three dimensional
NW	nanowire
NR	nanorod
NB	nanobelt
NC	nanocolumn
NT	nanotube
NF	nanoflower
RT	room temperature
WZ	wurtzite
ZB	zincblende
E_g	band gap
DFT	density functional theory

NH_3	ammonia
Ar	argon
N_2	nitrogen
VT	vaporation temperature
DT	deposition temperature
VLS	vapor-liquid-solid
VSS	vapor-solid-solid
VS	vapor-solid
CNTs	carbon nanotubes
RE	rare earth
CVD	chemical vapor deposition
(PA)MBE	(plasma-assisted) molecular beam epitaxy
MOCVD	metal organic chemical vapor deposition
DC	direct current
RHEED	reflection high-energy electron diffraction
UHV	ultra high vacuum
AAO	anodic aluminum oxides
MWCNT	multi-walled carbon nanotubes
SEM	scanning electron microscope
MQW	multiple quantum wells
TEM	transmission electron microscope
HRTEM	high-resolution transmission electron microscope
PL	photoluminescence
EL	electroluminescence
CL	cathodoluminescence
QE	quantum efficiency
SE	secondary electron
XAFS	X-ray absorption spectroscopy
CCT	correlated color temperature
CRI	color redering index

IQE	internal quantum efficiency
SKPM	scanning Kelvin probe microscopy
PV	photovoltaic
PCE	power conversion efficiency
APCE	absorbed photon conversion efficiency
AQE	apperant quantum efficiency
C-AFM	conductive atomic force micrographe

1. Introduction

After the first demonstration of high-efficient blue light emitting diodes (LEDs) in 1994 and laser diodes (LDs) in 1996, GaN-based III-nitrides have become prominent materials for optoelectronic devices and high-power electronics. Commercialized III-nitrides based blue and green LEDs are basic components for full color displays since 1995, and the GaN blue LD (405 nm) has become a new standard for data storage (Blue-ray technology). Consequently, the combination of the blue LED with phosphors has revolutionized the solid-state lighting technology, offering an efficient and environmental-friendly alternative to the general lighting market. The Nobel Prize in Physics 2014 was awarded jointly to I. Akasaki, H. Amano and S. Nakamura, for the invention of efficient blue LEDs based on III-nitrides, which have enabled bright and energy-saving white light sources. Group III-nitride semiconductors have been viewed as one of the most important families of semiconductor materials for modern electronics and optoelectronics (Figure 1).

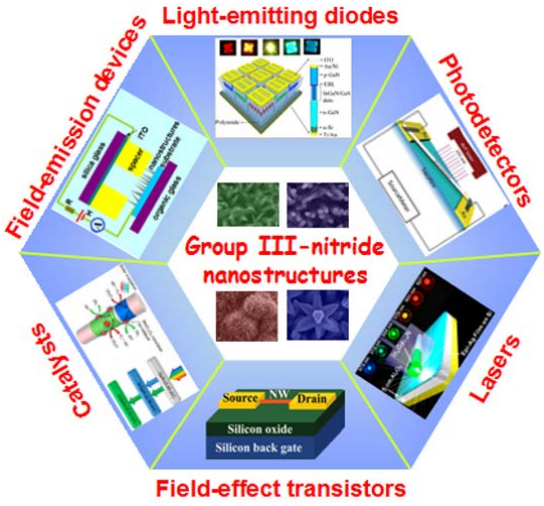

Figure 1 Versatile applications of group III-nitride nanostructures.

The binary group III-nitrides (AlN, GaN, and InN) can be either wurtzite (WZ) or zincblende (ZB). WZ is a hexagonal and stable structure under normal ambient conditions. [1] ZB is a cubic and meta-stable structure, which can only be obtained under certain conditions. For an example, stabilization of cubic GaN films was achievable in molecular beam epitaxy (MBE) within a narrow process window.[2-3] Alternatively, ZB binary group III-nitrides

consists of tetrahedrally coordinated M (M=Al, Ga, and In) and N atoms stacked in the ABCABC pattern, while the same building blocks are stacked in the ABABAB pattern in WZ, as depicted in Figure 2. In addition, AlN, GaN and InN also suffer phase transitions directly from the WZ phase to the rocksalt phase at sufficiently high pressures.[4] The discusssions in this review generally only concern the WZ phase.

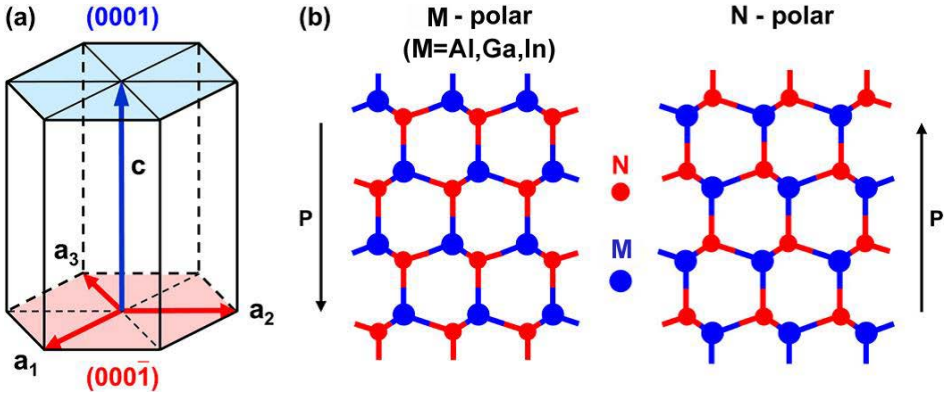

Figure 2 (a) Hexagonal unit cell and (b) atomic structure of M (M=Al, Ga, In)- and N-polar binary nitrides.

Table 1 Basic material parameters of wurzite bulk AlN, GaN, and InN.[5]

Parameter	AlN	GaN	InN
Bandgap E_g (T=0) (eV)	6.25	3.51	0.69
Bandgap E_g (T=300 K) (eV)	6.14	3.43	0.64
Lattice constant a (T=300 K) (nm)	0.3112	0.3189	0.3533
Lattice constant c (T=300 K) (nm)	0.4982	0.5185	0.5693
Coefficient of thermal expansion $\triangle a/a$ (10^{-6}/K)	4.2	5.6	3.8
Coefficient of thermal expansion $\triangle c/c$ (10^{-6}/K)	5.3	3.2	2.9
Melting point (°C)	3487	2791	2146
Static dielectric constant ($\varepsilon_S/\varepsilon_0$)	8.5	8.9	10.5
High-frequency dielectric constant ($\varepsilon_\infty/\varepsilon_0$)	4.6	5.4	6.7
Exciton binding energy (meV)	60	34	9
Exciton Bohr radius (nm)	1.4	2.4	8
Electron Effective mass at band edge m^*_e/m_0	0.32	0.20	0.07
Electron mobility (T=300 K) (cm^2/Vs)	300	900	4400
A_1(TO) phonon (cm^{-1})	611	532	447
A_1(LO) phonon (cm^{-1})	890	734	586
E_1(LO) phonon (cm^{-1})	912	741	593
E_1(TO) phonon (cm^{-1})	671	559	476
E_2(high) phonon (cm^{-1})	657	568	488
E_2(low) phonon (cm^{-1})	249	144	87

The band structure of a semiconductor material describes ranges of energy that an electron is “forbidden” or “allowed” to have and it determines important electronic and optical properties of the semiconductor. Figure 3 depicts the representative band structures of WZ AlN, GaN, and InN simulated using density functional theory (DFT) calculations.[6] Theoretically, the bandgap of group III-nitride WZ phases are direct. The optical properties are related to the band structure, its dispersion and probabilities of inter-band optical transitions, which are experimentally distinct.[7-9] Some basic parameters of WZ AlN, GaN and InN are summarized in Table 1

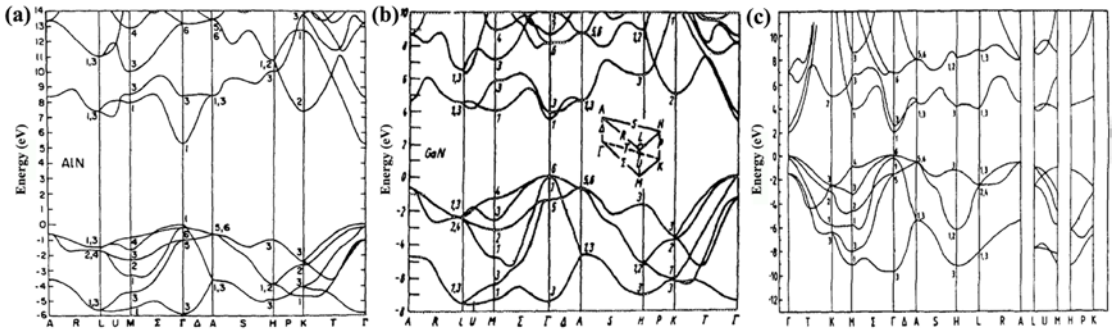

Figure 3 Calculated band structure of wurtzite binary nitrides: (a) AlN; (b) GaN; (c) InN.[6]

According to Vegard’s Law, the bandgap of ternary group III-nitride alloys, including AlGaN, InGaN, and AlInN, can be tuned by adjusting the compositions.[10] Based on the relationship between the bandgap and compositions, the bandgap of $Al_xGa_{1-x}N$, $In_xGa_{1-x}N$, and $Al_xIn_{1-x}N$ alloys over the entire composition range can be well fitted by Eq. (1):

$$E_g(x)= E_g(0)\cdot x+ E_g(1)\cdot(1-x)-b\cdot x\cdot(1-x) \qquad (1)$$

where $E_g(0)$ and $E_g(1)$ are the optical bandgaps of ternary nitride alloys with x = 0 and 1, b is the bowing parameter, which reflects the effects of strain, doping and composition fluctuation. Therefore, it is critical to measure E_g over a large range of composition to obtain an accurate assessment of b.[11]

Numbers of theoretical models have been developed to predict optical and electronic properties of group III-nitride ternary alloys.[11-14] Teles et al. calculated the bandgaps of $Al_xGa_{1-x}N$, $In_xGa_{1-x}N$, and $Al_xIn_{1-x}N$ by combining first-principle calculations within the

LDA-1/2 (local-density approximation (LDA) together with the half occupation (transition state)) approach with the generalized quasi-chemical approach (GQCA).[14] The investigated comparison of LDA, LDA-1/2, and experimental results of bandgap of the three ternary alloys shown in Figure 4 demonstrated well matched LDA-1/2 predictions and the experimental results.

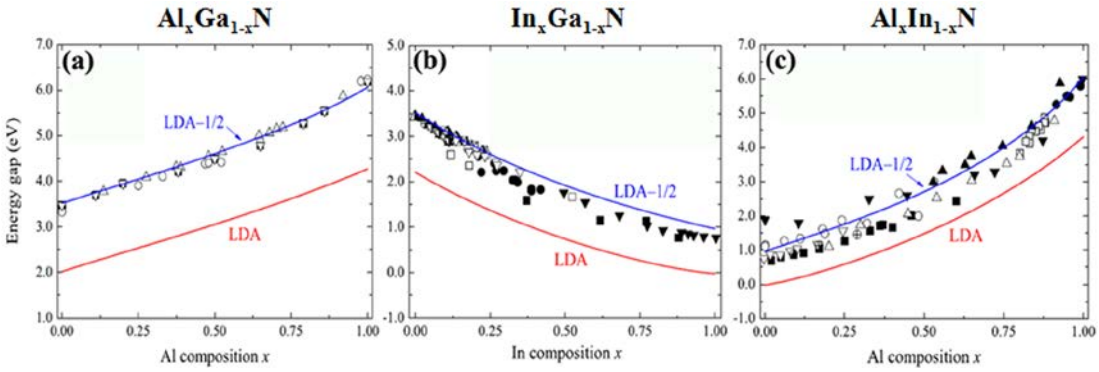

Figure 4 Simulated energy gap of (a) $Al_xGa_{1-x}N$, (b) $In_xGa_{1-x}N$, and (c) $Al_xIn_{1-x}N$: comparison between LDA (red line) and LDA-1/2 (blue line) calculations.[14]

With the rapid development of nanoscience and nanotechnology, the synthesis and applications of group III-nitride nanostructures have been thoroughly investigated in recent years. In this article, we will present a comprehensive review of the state-of-the-art research activities related to group III-nitride nanostructures, including the synthesis, fundamental properties and potential applications. We will start by reviewing the synthesis methods of abundant group-III nitride nanostructures, after which we will focous on the electrical, chemical and physical properties of the synthesized nanostructures, and the prospects of diverse group III-nitride nanostructures in various functional device applications. We will finish with an outlook on present challenges and perspectives of further investigations of nanostructured group III-nitrides.

2. Synthesis and growth mechanisms

2.1 Growth mechanisms

The growth of the group III-nitride nanostructures is based on the vapor phase techniques, which can be categorized into three types: vapor-liquid-solid (VLS), vapor-solid (VS), and vapor-solid-solid (VSS).

2.1.1 Vapor-liquid-solid

The VLS growth mechanism is widely employed to fabricate various types of 1D group III-nitride nanostructures by CVD method. To illustrate the growth procedure more clearly, the schematic is shown in Figure 5(a). The growth sequences of the NWs based on VLS mechanism can be divided into three stages: (I) the catalyst particles deposited on the surface of a substrate react firstly with the metal source (Al, Ga or In) to form the eutectic alloy at a certain temperature; (II) nucleation occurs when the liquid eutectic alloy becomes supersaturated with the source metal vapor; (III) grow along one particular crystallographic orientation due to the continuing supplement of reactive vapor, resulting in the formation of 1D NWs. One of the most distinct features of the 1D nanostructures fabricated by the VLS growth mechanism is the presence of a metal nanoparticle at the tip of the nanostructures.

The VLS growth mechanism is very successful in synthesizing large numbers of 1D nanostructures (single and heterostructured NWs) with uniform crystalline structures. The disadvantage of the VLS method may be the contamination caused by the intentional use of metal catalysts, which may result in the destruction of the material performances. However, the influence of the contamination for specific properties of the 1D nanostructures can be minimized by appropriately selecting the catalysts and the post-treatment process.

2.1.2 Vapor-solid

The anisotropic growth of group III-nitride nanostructures by VS mechanism is generally guided by the following factors, different growth rates of various crystal planes, the preferential accumulation of specific planes, and the presence of crystal defects. In addition, a

decrease in the Gibbs free energy may result in recrystallization, or a decrease in supersaturation accelerates the spontaneous growth of 1D nanostructures. In a typical VS growth process, the vapor precursors are first generated by evaporation, decomposition or chemical reaction, then transport to the substrate. Nucleation of the growth species on substrate occurs due to the supersaturation of vapor. Eventually, the desired 1D semiconductor nanostructures can be obtained by a series of processes, including adsorption, diffusion, desorption, and subsequent deposition of the species. The diameter and shape of the as-synthesized 1D nanostructures are largely dependent on the experimental parameters and controlled by the crystal growth kinetics.

A large number of 1D group III-nitride nanostructures were grown *via* VS growth mechanism,[15- 20] the corresponding schematic of the VS growth mechanism during the CVD-growth of III-nitride NWs is illustrated in Figure 5(b). The metal vapor is generated by evaporation of metal precursors or decomposition from the chlorides, then transport to the deposition zone and condense into metal cluster on the substrate. Whereafter, the initially condensed metal clusters (solid phase) form as the nucleation sites when the metal vapor is saturation. Finally, the nucleation sites anisotropically grow along the preferential axis, forming the 1D morphology.

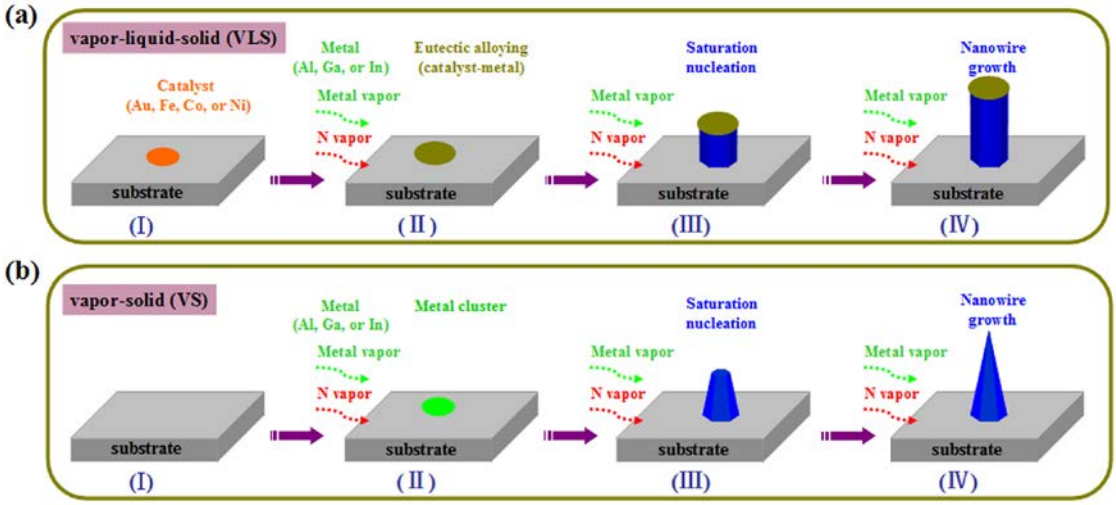

Figure 5 Schematic diagrams of the 1D group III-nitride nanostructures based on (a) VLS and (b) VS growth mechanism.

2.1.3 Vapor-solid-solid

VSS is an analogous growth mechanism to VLS with the distinct difference of catalyst states. In VSS, the catalyst is in solid-state, while in VLS the catalyst is in liquid-state. It was first proposed in 2000 by Kamins et al.[21] in Ti-catalyzed silicon NWs. Subsequently, VSS was applicable to explain the growth of group III-nitride nanostructures.[22-23]

2.2 Synthesis techniques

A variety of synthesis techniques have been developed to fabricate group III-nitride nanostructures. They can be classified into two broad categories: top-down and bottom-up strategies. Till now, multifarious WZ nitride nanostructures have been demonstrated such as nanowires (NWs), nanorods (NRs), nanobelts (NBs), nanotubes (NTs), nanocones, nanotowers, and so on, as shown in Figure 6. In this section, we will briefly summarize the most well-developed physical and chemical vapor techniques that emerged during the past few years with a focus on “bottom-up” strategy for the growth of 1D group III-nitride nanostructures.

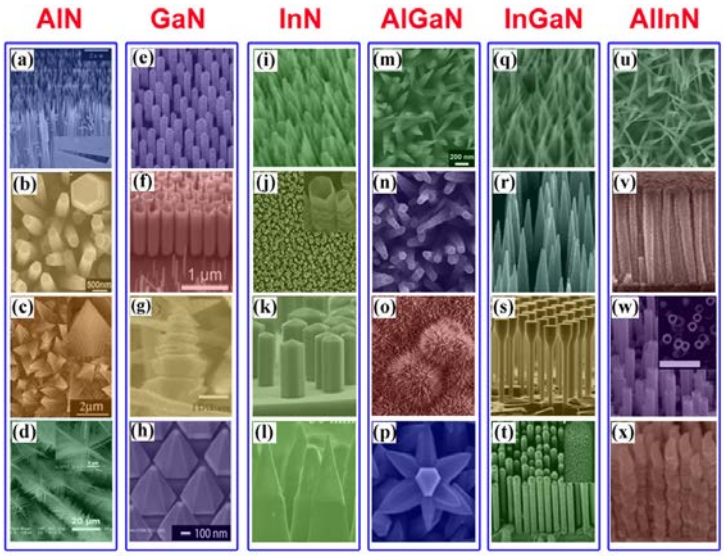

Figure 6 Diverse morphologies of group III-nitride nanostructures: (a)-(d) AlN nanocones[24](a), nanoclomuns[25] (b), nanopyramids[26] (c), sixfold-symmetrical hierarchical nanostructures[27](d); (e)-(h) GaN NWs[28] (e), nanotubes[29] (f), nanotowers[30] (g), nanocones[31] (h); (i)-(l) InN NWs[32](i), NTs[33](j), NCs[34] (k),

nanotowers[35] (l); (m)-(p) $Al_xGa_{1-x}N$ nanocones[36] (m), nanotowers[19](n), NFs[19](o), six-fold symmetry heptapods[19](p); (q)-(t) $In_xGa_{1-x}N$ NWs[37] (q), nanotips[38] (r), nanonails[39] (s), nanotrees[40] (t); (u)-(x) $Al_xIn_{1-x}N$ nanocones[41] (u), NCs[42] (v), NTs[43](w), nanospirals[44].

2.2.1 Chemical vapor deposition

Chemical vapor deposition (CVD) is a vapor-phase growth method, which essentially involves the volatile precursors at different pressures with specific flow rates, dissociations of reactive gases, and chemical reactions so as to fabricate the target compounds on the substrates. For CVD processes, a series of parameters can be adjusted to control the growth, including (1) the type of the precursor materials, which may determine the phase and stoichiometry of the products; (2) the evaporation temperature of the source materials, mainly considering the volatility and saturated vapor pressure of the precursors; (3) the pressure of the growth chamber, to control the evaporation rate and vapor pressure of the precursors; (4) the species, size and amount of catalyst, which will influence the size and morphology of the products; (5) the substrate temperature, which will strongly determine the type of product obtained; (6) the carrier gas and its flow rate, to allow certain chemical reaction to occur during vapor transportation and to adjust the growth rate; (7) the type of substrate, which can tune the electrical performance and flexibility of the products; (8) the growth time, which will affect the yield and size of the products. In principle, it is possible to construct any solid material into 1D nanostructures by precisely controlling the synthesis conditions. Various CVD techniques have been developed to synthesize III-nitride nanostructures.

2.2.1.1 Simple compound involved CVD

It is usually available for the III-nitride nanostructures grown from the metal (Al, Ga, or In) vapors in the presence of NH_3 using atmospheric CVD method.[15] Various AlN nanostructures,[45-48] including NBs, NRs, nanorings, nanotips, branched nanostructures, and oriented nanostructures[25] were reported. In these works, the growth temperature and NH_3 flow rate played a crucial role in the structural and morphological evolution. A

surface-diffusion controlled mechanism based on the VS process was proposed as the underlying principle of AlN nanostructures' growth. Simultaneously, this strategy was also applied to fabricate GaN NWs and NRs,[49-51] and InN NWs and NTs,[52], and other irregular nanostructures.[53]

In addition, the direct reaction of metal vapor under the flowing gas of NH_3 was also applied to synthesize the 1D ternary III-nitride nanostructures. For an example, WZ alloyed AlGaN NWs over the entire compositional range had been grown on catalyst-free Si(100) substrates by using NH_3 vapor and a mixture of Al powder and molten Ga droplets.[54] During the growth process, the composition of ternary alloyed NWs could be controlled through adjusting the mass ratios of Ga to Al in the mixture. Similarly, the InGaN NCs on amorphous SiO_2 substrates were produced through varying In content and substrate temperatures using plasma-enhanced evaporation.[55] The overall reactions of binary and ternary III-nitrde nanostructures using metal (Al, Ga, or In) vapors and NH_3 were expressed by Eqs (2)-(6). In general, the diameter of the nanostructures was dependent on the growth temperature and NH_3 flow rate, and the NW length was principally dependent on the growth time.

$$2Al\ (g) + 2NH_3\ (g) \rightarrow 2AlN\ (s) + 3H_2\ (g) \quad (2)$$

$$2Ga\ (g) + 2NH_3\ (g) \rightarrow 2GaN\ (s) + 3H_2\ (g) \quad (3)$$

$$2In\ (g) + 2NH_3\ (g) \rightarrow 2InN\ (s) + 3H_2\ (g) \quad (4)$$

$$2Al\ (g) + 2Ga\ (g) + 2NH_3\ (g) \rightarrow 2AlGaN\ (s) + 3H_2\ (g) \quad (5)$$

$$2In\ (g) + 2Ga\ (g) + 2NH_3\ (g) \rightarrow 2InGaN\ (s) + 3H_2\ (g) \quad (6)$$

2.2.1.2 Chloride-assisted CVD

Due to the low vaporization and low decomposition temperature of group-III metal chlorides, III-nitride nanostructures can be easily obtained through chloride-assisted CVD. Since 1997, Haber et al. employed $AlCl_3$ as a growth promoter to synthesize AlN nanowhiskers,[56-57] and found that the formation of AlN nanowhiskers were strongly dependent on the presence of $AlCl_3$. The yield of nanowhiskers was significantly enhanced

with the addition of $AlCl_3$. Subsequently, $AlCl_3$, $GaCl_3$, or $InCl_3$ were widely employed as the growth promoters to synthesize III-nitride nanostructures through CVD method. Our group demonstrated large-scale single-crystalline AlN nanotips and NRs on Si, [58-59] flexible graphite sheet,[20] carbon cloth[18] substrates, and the growth of AlN-MoS_2 core-shell NWs[60] *via* the catalyst-free CVD using $AlCl_3$ and NH_3 as the precursors. Typical scanning electron microscopy (SEM) images of AlN nanostructures are shown in Figure 7. The distance between source material and substrate was 4-5 cm, and the growth temperature was ~1000 °C. We found that the self-catalytic Al, resulted from the decomposition of $AlCl_3$ at the very beginning of the reaction, acted as nucleation sites, and then formed AlN with subsequently absorbed N ions from the decomposition of NH_3, leading to the growth of AlN nanostructures with various configurations on the substrates.

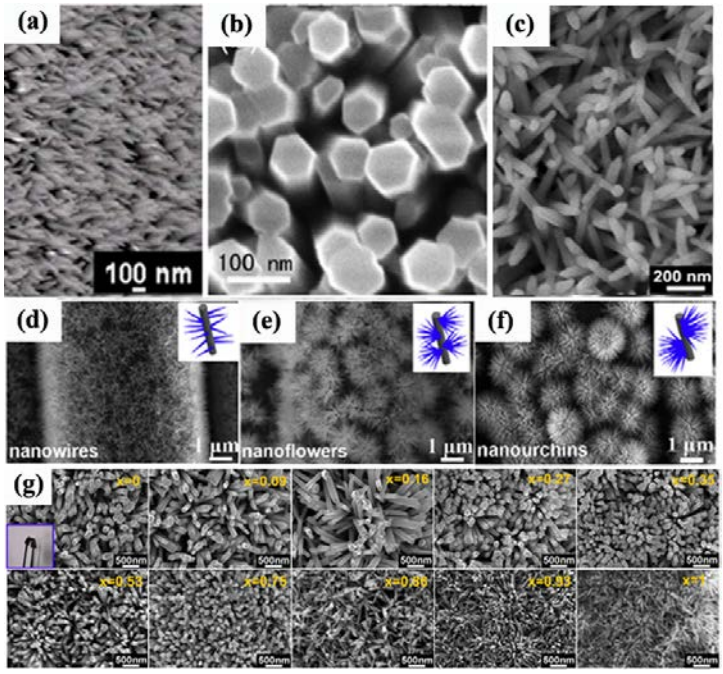

Figure 7 (a)-(c) The typical SEM images of the large-scale AlN nanotip arrays,[58] AlN NR arrays,[59] and AlN NWs on graphite sheet;[20] (d)-(f) the SEM images of the AlN nanostructures with different morphologies on carbon cloth;[18] (g) the SEM images of $Al_xGa_{1-x}N$ nanocones across the entire composition range.[36]

Chen et al. reported the fabrication of well-aligned GaN NCs through the chloride-assisted CVD.[61] 1D GaN nanostructures evolved from nanoneedles to NCs with hexagonal top facet with the growth temperature increasing from 750 °C to 900 °C, and the

diameter of GaN NCs was gradually increased.[62] A VS growth process of the aligned GaN NCs includes heterogeneous nuclei formed on Si substrate, followed by the epitaxial growth of NCs occurred on the nuclei along the preferential [001] direction.

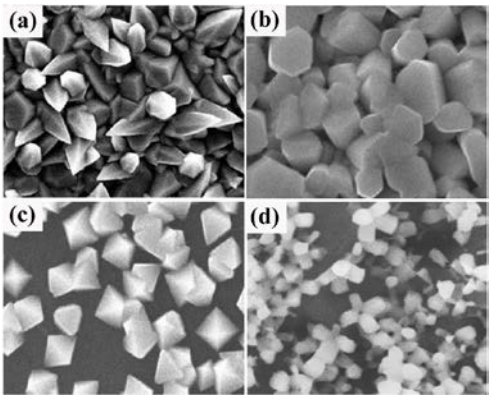

Figure 8 SEM images of the InN nanostructures obtained at different VT and DT: (a) nanocones obtained at VT = 470 °C and DT = 550 °C, (b) hexagonal nanoprisms obtained at VT=470 °C and DT=600 °C, (c) octahedrons obtained at VT = 480 °C and DT = 550 °C, (d) four-fold-symmetrical hierarchical nanostructures obtained at VT = 480 °C and DT = 580 °C.[63]

However, the synthesis of InN nanostructures through the chloride-assisted CVD suffered crucial problems of low dissociation temperature, resulting in their low growth rate below 500 °C and upward dissociation trend at the temperature higher than 600 °C.[64] Zhang et al. reported the InN nanostructures with various morphologies using $InCl_3$ and NH_3 as the sources, as shown in Figure 8.[63] The InN nanostructure was strongly influenced by In flux and the deposition temperature.

Chloride-assisted CVD was fulfilled on the fabrication of $Al_xGa_{1-x}N$ nanostructures. Our group has systematically studied $Al_xGa_{1-x}N$ nanostructures with various morphologies, including NRs,[65] nanotowers,[17] nanonails, NFs, six-fold symmetry heptapods, and three-fold symmetry tetrapods [19] by tuning the evaporating temperatures of $AlCl_3$ and $GaCl_3$, flow rate of NH_3, the substrate temperature when NH_3 was introduced, and the growth temperature. The composition manipulation of $Al_xGa_{1-x}N$ NWs ranging from x = 0 to 1 is realized by adjusting the VT of $AlCl_3$ and $GaCl_3$ in our group,[66] as shown in SEM images in Figure 7(g). $AlCl_3$, $GaCl_3$ and substrates were placed separately in three adjacent temperature zones, and NH_3 was introduced to the deposition zone through an inner small

quartz tube. The evolution of $Al_xGa_{1-x}N$ nanostructures from nanonails to complex configuration were systematically investigated in terms of the saturation vapor pressure of the precursors by tuning the growth parameters. A VS growth mechanism combined with the surface diffusion process was responsible for the formation and evolution of the series of nanostructures.[17]

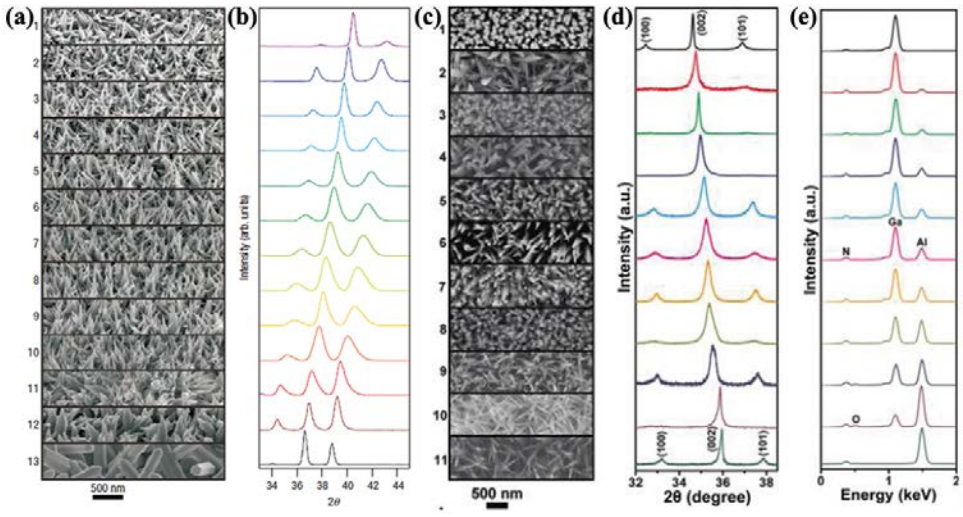

Figure 9 (a)-(b) SEM images and (100), (002) and (101) XRD peaks of the $In_xGa_{1-x}N$ NWs with the entire composition range;[37] (c)-(e) the SEM images, XRD and EDS patterns of $Al_xGa_{1-x}N$ NWs in the whole composition range.[36]

Composition tunable $In_xGa_{1-x}N$ NWs were reported by Yang's group using chloride-assisted CVD in 2007.[37] The synthesis process allowed independent vapor pressure control of both metal sources to balance the chemical potentials of the different chemical species at the growth front, keeping them in the (III) chlorides. Using N_2 carrier gas to tune the In ratio quite finely as the $In_xGa_{1-x}N$ grew on a sapphire substrate. The SEM images and XRD patterns of the $In_xGa_{1-x}N$ NWs in the whole compositional range are provided in Figure 9(a) and (b). Figure 9(c)-(e) shows SEM, XRD and EDS results of the $Al_xGa_{1-x}N$ nanocones on Si substrate across the whole composition range from He's group.[36] In their work, the $AlCl_3$, $GaCl_3$, and NH_3 precursors were separately located at three neighboring temperature zones in order to minimize the influence of each other. To get a single phase $Al_xGa_{1-x}N$ nanocone, the matchable VT were optimized to be 70-90 °C for $GaCl_3$ and 130 - 150 °C for $AlCl_3$, and the temperature of the deposition zone was set at 700 °C. By adjusting the VT of $GaCl_3$ and $AlCl_3$ precursors, the partial pressures of $GaCl_3$ and $AlCl_3$

vapors could be modulated. Thus, the $Al_xGa_{1-x}N$ nanocones across the entire composition range were obtained.

Due to the successful growth of $In_xGa_{1-x}N$ and $Al_xGa_{1-x}N$ nanostructures, chloride-assisted CVD was considered as an important technique for the fabrication of ternary nitrides nanostructures. However, the In content was limited in the range of 0 - 0.5 due to the difficulty in In supplying and the instability of InAlN with high In content, suggesting that a low-temperature growth method should be adopted to further increase the In content. Recent work of Du et al. reported different $In_xAl_{1-x}N$ nanostructures with a composition range of $0<x<0.5$ by chloride-assisted CVD method, as shown in Figure 6(u).[41] Typically, $AlCl_3$, $InCl_3$ and a Si (100) substrate were placed separately in the three zones along the gas flow direction, which was very similar to the reports of the growth of $In_xGa_{1-x}N$ and $Al_xGa_{1-x}N$ nanostructures.[16-17, 19, 37] The VT of $AlCl_3$ was set at 130 °C, the $InCl_3$ source was heated in the range of 300 - 500 °C to adjust the vapor pressure ratio of $InCl_3$ to $AlCl_3$, and the growth temperature was fixed at 700 °C. By tuning the vapor pressure ratio of $InCl_3$ to $AlCl_3$, the morphology of $In_xAl_{1-x}N$ nanostructures evolved from nanocones, to NCs, to nanobrushes, and finally back to nanocones along with the composition (x) regulation in the range of $0 < x <0.5$.

2.2.1.3 Metalorganic chemical vapor deposition (MOCVD)

In 2003, Yang et al. reported the synthesis of high-quality GaN NWs *via* metal-initiated MOCVD.[67] Trimethylgallium (TMG) and NH_3 were used as Ga and N precursors, respectively. The precursors of MOCVD process experienced pyrolytic reactions in a furnace at elevated temperatures, where the metallic atom was deposited on the substrate while the organic compound was removed from the reaction chamber. A silicon substrate and *c*-/*a*-plane sapphires with thermally evaporated thin films of Ni, Fe, or Au were used as substrates. The NWs growth occurred at substrate temperature of 800 - 1000 °C following VLS growth mechanism. Subsequently, selected area growth of GaN NW and NR arrays by MOCVD was demonstrated.[8, 68] Figure 10 (a) and (b) show the SEM images of the as-grwon GaN NW arrays using a SiN mask, and the GaN NR arrays with three tapering

portions using a patterned-hole template through pulsed growth mode could be observed. The location, orientation, and diameter of the GaN NW or NR were controlled by using a selective growth mask. The utilization of a pulsed MOCVD process not only kept the diameter of NWs constant under high group V/III ratio (1500), but also obtained NRs with multiple sections of different cross-sectional size under low group V/III ratio (75).

The growth of AlN NWs by MOCVD was reported by Cimalla et al.[69] . At the temperature below 1000 °C, the Kirkendall effect during the alloying of Al and the catalyst resulted in the formation of 3D nanostructures like lamellas and NFs. The growth temperature above 1000 °C was necessary to grow the AlN NWs.

InN NFs grown by MOCVD was reported by Kang et al.[70] The sapphire substrate was nitrided under an NH_3 flow at 1050 °C for 3 min before the growth. Nitrided sapphire substrate was helpful in improving the quality of the InN NFs. Due to the introduction of hydrogen in the MOCVD system, segragated metallic In unintentionally exists. As a result, the metallic In form was enhanced by the hydrogen, which induced VLS growth of InN NFs.

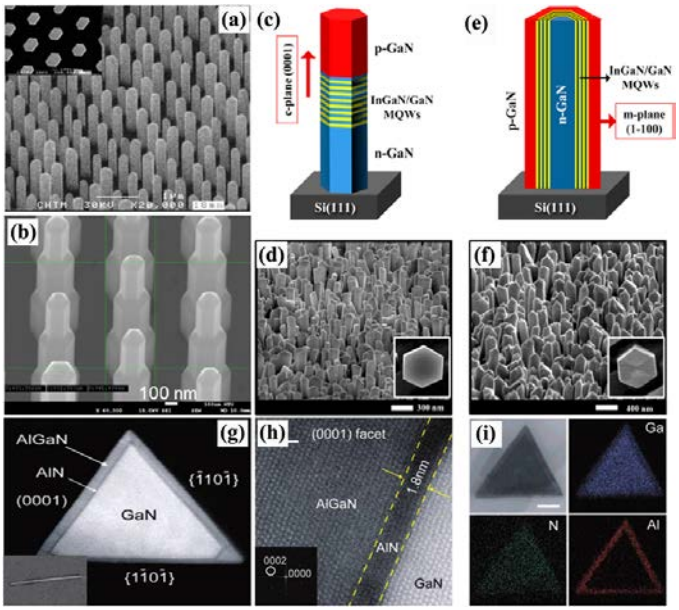

Figure 10 The characterization of group III-nitride nanostructures obtained by MOCVD: (a) SEM image of the GaN NWs using the SAG method;[8] (b) SEM image of the GaN NR array with three tapering portions;[68] (c)-(f) schematic diagrams and SEM images of the *c*-plane (uniaxial) oriented (c)-(d) and *m*-plane (coaxial) oriented InGaN/GaN MQW NWs (e)-(f);[71](g)-(i) HAADF-STEM, lattice-resolved HAADF-STEM, SAED, and EDX elemental mappings of GaN/AlN/AlGaN NWs.[72]

Ternary nitrides nanostructures, such as AlGaN NWs,[73] InGaN nanotips,[74] InGaN nanodots/nanorings/nanoarrows,[75] InGaN nanoneedles,[76] InGaN NRs,[77] AlInN NTs[43] synthesized by MOCVD were reported. MOCVD is not only a feasible method to fabricate 1D ternary nitrides nanostructures, but also can be integrated to the fabrication of MQWs. For example, Lieber's group reported the rational synthesis of GaN/AlN/AlGaN radial NW heterostructures, as shown in Figure 10(g)-(i), by sequential shell growth immediately following NW elongation using MOCVD.[72] In contrast, Ra et al.[78] fabricated InGaN QWs within doped GaN NWs, where pulsed-flow MOCVD was used to create different layers: a core of *n*-doped GaN NW, layered with InGaN and GaN, covered with *p*-doped GaN. These NWs showed a high level of emission efficiency. The controlled synthesis of InGaN/GaN MQW uniaxial (*c*-plane) and coaxial (*m*-plane) NW heterostructures were also fabricated by MOCVD, as exhibited in Figure 10 (c)-(f).[71] The structural orientation of the heterostructures from *c*-plane to *m*-plane were realized by adjusting the growth temperature and working pressure.

In general, MOCVD can accomplish high volume growth with its high intake of precursor gas and possibility to use a large size substrate to harvest more nanostructures. Yet, limitations exist for the MOCVD process, such as the use of highly toxic gases and complicated chemistry, causing undue increase of the cost.

2.2.2 Physical vapor deposition

2.2.2.1 DC arc discharge method

The synthesis of nanostructures, particularly CNTs, through arc discharge method was first introduced by Iijima in 1991.[79] Since then, DC arc discharge method was developed for the synthesis of 1D inorganic semiconductor nanostructures, especially the compounds with high-melting point, such as nitrides, carbides, oxides, and silicides. The most outstanding advantages of this technique are the scorching temperature, reaching several thousands degrees, and large temperature gradient,[80] which enable the fabrication of nanostructures with high crystal quality.

Tondare et al.[81] developed the DC arc discharge technique for the growth of AlN NTs.

Subsequently, Lei and co-workers systematically investigated the growth of undoped and RE doped AlN nanostructures using DC arc discharge method. By adjusting the reactant gas pressure, voltage, input current, and growth time, various complex morphologies of AlN and AlN:M (M=Sc,Y) nanostructures were synthesized on Al, W, and Mo substrates.[82-84] The formation of various AlN nanostructures was discussed on the basis of the intrinsic properties of AlN.[85] During the arc discharge process, thermal decomposition of N_2 and evaporation of Al anode resulted in the formation of Al and N vapors, which were then transported by N_2 carrier gas to the substrate at a certain temperature to form AlN crystals. During this step, the heat convection and temperature gradient generated by the arc plasma provided a chemical-vapor transport and a condensation process, which was responsible for the nucleation of AlN. AlN crystal grew along certain direction to form 1D AlN nanostructures with the continued absorption of Al and N atoms. The growth rate along the [0001] growth direction was high because of abundant supply of Al and N during the initial stage in the high N_2 pressure. With the comsumption of Al, the lower evaporation of Al and insufficient Al supply to the substrate led to lower growth rate than the initial stage, resulting in the shorter 1D nanostructures grown on the former 1D nanostructure.

The synthesis of GaN NRs through DC arc discharge method was carried out by Han et al.[86] The reaction was achieved by igniting an anode of a mixture of GaN, graphite, nickel powders, with a graphite cathode in a nitrogen atmosphere. The as-grown products were GaN-Carbon composite NTs and GaN NRs. The DC arc discharge method, on the whole, could be employed to obtain AlN and GaN nanostructure with good crystalline structure due to the high growth temperature and the high temperature gradient involved. Nevertheless, with the inherent complexity of the arc discharge process itself, the composition and purity of the as-synthesized products were difficult to be controlled.

2.2.2.2 Molecular beam epitaxy (MBE)

MBE is an epitaxial growth technique of semiconductor compounds involving the reaction of thermal molecular beams on a substrate under ultra-high vacuum conditions.[87] Specifically, MBE-grown group III-nitride NWs are typically formed under N-rich condition

without any foreign catalyst. This process is also commonly referred as a spontaneous self-organized formation process. The NW formation and nucleation processes can be further promoted with the use of an *in situ* deposited seeding layer, e.g., Ga and In during the growth of GaN and InN, respectively. Many research groups have demonstrated the applicability of the approach for the growth of pure binary and ternary III-nitride nanostructures and the heterostructures.

Yoshizawa et al.[88] grew the GaN NCs by radio-frequency MBE (RF-MBE). The growth rate, density, and diameter of NCs were dependent on the N_2 flow rate and the RF input power. Daudin et al.[89] reported the catalyst-free PAMBE growth of AlN NWs. Taking advantage of Volmer-weber growth mode, there was no amorphous layer between the nanostructures and substrates. However, most studies revealed the existence of a thin amorphous layer between Si substrate and group III-nitride nanostructures under N-rich conditions by MBE. To understand the underlying mechanism, Consonni et al.[90] performed detailed analysis by combining *in situ* RHEED measurement with *ex situ* HRTEM imaging. The result suggested that the NW nucleation started from 2D nuclei, then nucleis transformed into NWs. The transformation process was mainly driven by the surface energy anisotropy as modeled theoretically. These results inferred that the growth of III-nitride NWs by MBE did not form any epitaxial relationship with the underlying substrate essentially. Therefore, III-nitride NWs in principle can be grown on different substrates including graphene layer and amorphous glass by MBE. Following the successful growth of binary III-nitride nanostructures on diverse substrates, ternary $In_xGa_{1-x}N$ nanostructures were tuned by changing substrate temperature[91] and In flux during the MBE process.[92] More recently, Pierret et al.[93] applied the PAMBE to grow $Al_xGa_{1-x}N$ NWs with x in the range of 0.3 - 0.8. The structural and optical properties of $Al_xGa_{1-x}N$ NWs were governed by the presence of compositional fluctuations associated with strongly localized electronic states. Meanwhile, Tangi et al.[94] reported the PAMBE-growth of dislocation-free $In_xAl_{1-x}N$ NWs in the temperature regime of 490 - 610 °C yielding In composition rangeing $0.17 \leq x \leq 0.50$.

Zhao et al.[95] obtained highly uniform GaN NWs on thick SiO_x template by PAMBE, which were free of stacking faults and misfit dislocations. InGaN/GaN dot-in-a-wire LED structures were investigated. The device exhibited stronger emission compared to that grown

directly on Si substrate, originating from the reduced light absorption by the Si substrate. In addition, the patterned substrates were employed to fabricate III-nitride nanostructures.[96-99] During the growth, a mask layer was first deposited on the substrate, and then nanoholes were created on the mask layer, which governed the subsequent nanostructures growth and formation process.

With the successful fabrication of binary/ternary group III-nitride nanostructures, a variety of heterostructures were designed and synthesized, including InGaN/GaN dot-in-a-wire, [100 - 103] InGaN/GaN core-shell NWs,[104] AlN/GaN core-shell NWs,[105-107] AlGaN/GaN NWs,[108] InN/InGaN core-shell NWs,[109] InGaN/AlGaN dot-in-a-wire core-shell NWs.[110]

2.2.3 Template-assisted synthesis

Template-confined synthesis is one of the common techniques for the fabrication of 1D nanostructures with uniform and controllable geometry. Numbers of templates, including CNT,[111-113] AAO,[114-115] Mo grid,[116] Ti and SiO_2 mask,[29, 117] patterned SiC and SiO_x,[28, 96] were employed to synthesize 1D group-III nitride nanostructures. Mesoporous materials, including CNTs, AAO, and Mo grid are usually employed as the hard template to assist and confine the growth of 1D AlN or GaN nanostructures.

2.2.3.1 CNT template

Using CNTs as template, for an example, Zhu et al. reported the fabrication of straight and smooth AlN NWs with controlled diameters at the temperature of 800 - 1500 °C.[111, 113] During the synthesis procedure, the reaction occured among the CNTs, Al powder of 200 mesh, and Al_2O_3 powder (the weight ratio of Al/Al_2O_3 was 1) in a flowing NH_3 atmosphere. The proposed mechanism for the reaction of Al, Al_2O_3, and NH_3 is as follow:

$$2Al\,(s) + 2\,NH_3\,(g) \rightarrow 2AlN(s) + 3H_2(g) \quad (7)$$

$$2Al_2O_3\,(g) + C(s) + 4NH_3\,(g) \rightarrow 4AlN(s) + CO(g) + 5H_2(g) + H_2O(g) \quad (8)$$

The formation of AlN NWs is achieved through two independent reactions (7) and (8). Reaction (8) removes the CNT template and faciliate the reaction (7) going all the way to

form AlN NWs.

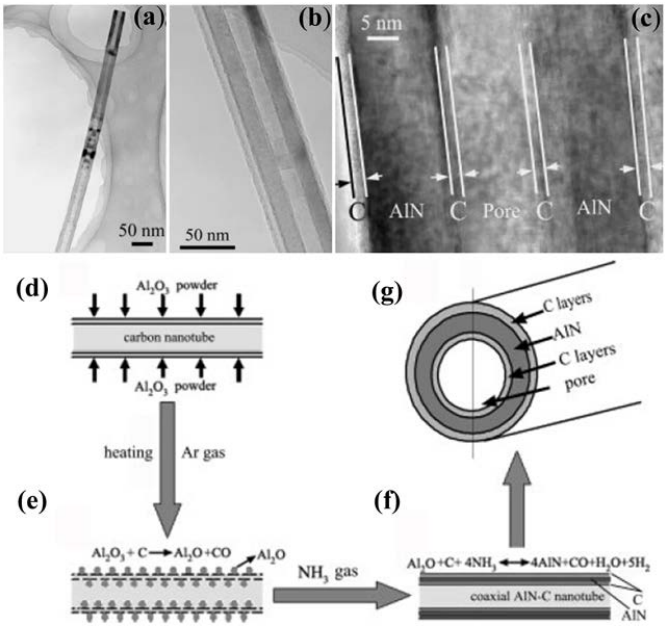

Figure 11 (a)-(c) The TEM images of a co-axial C-AlN-C composite NT with different magnifications; (d)-(g) schematic illustration of the formation process of C-AlN-C composite NTs.[112]

MWCNTs were applied to fabricate AlN and InN NTs, as reported by Yin and co-workers.[112, 118] The produced AlN consisted of composite NT with a coaxial structure, as shown in Figure 11(a)-(c), was synthesized through the reaction of multiwalled CNTs, Al_2O_3 powder and NH_3 at low pressure of 2-2.5 Torr. During the formation of C-AlN-C NTs, the MWCNTs not only simultaneously acted as the reducing agent, but also the template to control the morphology and size of AlN NTs. The formation of such heterostructure was attributed to a substitution reaction, in which carbon atoms of MWCNTs were finally substituted by AlN moleculars to form AlN NTs. The MWCNT substitution reaction should differ from MWCNT-confined reaction, which typically led to the formation of solid-like NW structures rather than hollow NTs, as proposed by Zhu et al.[111, 113]

CNT was also one of the most functional templates for GaN NWs growth.[119] A reaction of Ga_2O_3 and CNT in the flow of NH_3 occurred, which resulted in the formation of GaN NWs with similar diameter and length as that of the CNT template. In the presence of CNTs at 900 - 1000 °C, the following reactions are revolved during the formation of GaN NWs:

$$Ga_2O_3(s) + 4Ga(l) \rightarrow 3Ga_2O(g) \quad (9)$$

$2Ga_2O\ (g)+\ C(s)+4NH_3\ (g) \rightarrow 4GaN(s)+\ CO(g)+5H_2(g)+H_2O(g)$ (10)

However, if there is no CNT used in the fabrication process, only GaN powders are produced, the reaction is as follow:

$Ga_2O(g)+\ 2NH_3(g) \rightarrow 2GaN(s)+\ 2H_2(g)+H_2O(g)$ (11)

The work proved the importance of the CNT template in confining the growth of the desired 1D III-nitride nanostructures.

2.2.3.2 AAO template

AAO template possesses tunable monodispersed pore dimensions of 10 - 200 nm as diameter and several tens of micrometers as length, narrow pore size distribution, good mechanical and thermal stability.[120-121] Zhang et al.[115] reported the preparation of ordered GaN NWs within AAO template by reaction of metallic Ga and NH_3 at a temperature above 900 °C,

$2Ga\ (g)\ +\ 2NH_3\ (g) \rightarrow 2GaN(s)\ +\ 3H_2(g)$ (12)

As reported by Wu et al.[114], aligned hexagonal AlN NW arrays were produced with the help of AAO template, whereas AlN NWs with irregular morphologies were obtained without AAO template. They proposed that the space limitation reaction between Al and NH_3/N_2, followed by preferential growth along the *c*-axis parallel to the channels of AAO template underlied the growth mechanism of the hexagonal AlN NW arrays. Similarly, Zhang et al. [122] reported the AAO-assisted synthesis of InN NW arrays using the direct reaction of metal In with a constant flow of NH_3.

It should be noted that the efficiency of the template will be lost at high reaction temperature due to the fast reaction rate. For example, Al and NH_3 reacted to form AlN fibers with larger diameters than that of the template pores or channels, which weakened the function of the templates in isolation of the product with template and maintaining the alignment of the nanofibers.[123]

Objectively, the template-assisted synthesis method offers a feasible and controllable approach to the fabrication of 1D III-nitride nanostructures with desirable density, distribution, size, and morphology. However, it is expected that various post-treatments are necessary for

the isolation and removal of templates for the desired III-nitride nanostructures without damaging them.

2.2.4 Catalyst-assisted method

One of the most distinct features of the nanostructures synthesized through catalyst-assisted method is the presence of metal catalyst particles. Basically, the presence of a catalyst influences the nucleation sites, orientation and morphology of nanostructures, and accelerates the reaction without itself taking any part in. Numbers of group III-nitride nanostructures have been synthesized by catalyst-assisted CVD technique, as summarized in Table 2. Generally, the catalysts to assist the CVD growth of group III-nitride nanostructures are prepared in two ways: (1) metals or metal oxides deposited on the substrates by magnetron sputtering or evaporation; (2) dispersed on the substrate in solution form starting with the catalytic metal nitrate or sulfate.

Table 2 Summary of group III-nitride nanostructures synthesized using CVD method with different catalysts.

Catalyst	Material	Morphology
Au	AlN	NRs[124], NTs[125], (NRs, NFs, NSs)[126],(NWs, NFs,NCs)[127],
	GaN	NWs[128], Bicrystalline NWs[129], Serrated NWs[130], NRs[131]
	InN	NWs[132- 135], Periodic NWs[136],NBs[137], Stacked-cone NWs[138], Nanonecklace[139], Nanotowers[140], Ice-cream-like NWs[141]
	AlGaN	NWs[142-143]
	InGaN	NWs[144- 147], Coiled/zigzag NWs[148]
Ni	AlN	NCs[24], Hierarchical nanostructures[149], Aligned NRs[150]
	GaN	NWs[151], NBs[152], Nanotowers[30], Stacked-cone-shaped NWs[153]
	AlGaN	NTs[154], Nanocones[155]
Ag	GaN	NWs, Nanoribbons, Nanorings,[156]
Pt	GaN	Helical NWs[157]
Fe	GaN	NWs[158]
Co	AlN	NFs[159]
W	AlN	NWs[160]
Au/Pd	GaN	NWs[161-162]
Ni/Au	InGaN	NWs[163]
Au/Al/Pt	AlN	Nanotips[46]
Ni/Fe/Au	GaN	NWs[164]

In/Fe/Ni/Co	GaN	NWs[165]
Fe_2O_3	AlN	NWs[166], Nanowiskers[167], Rectangular nanofibers[168], Eiffel-tower-shaped nanotips[169], (Nanocones, NRs, Nanocraters)[170]
Fe/B_2O_3	GaN	NBs[171]
$Fe(NO_3)_3$	AlN	Zigzag NWs[172], Nanonecklaces[173]
$Ni(NO_3)_2$	AlN	Aligned NWs[114]
	GaN	NWs[174]
$CoSO_4$	AlN	NBs[175]
$NiCl_2$	AlN	Hierarchical nanostructures[176]
	GaN	NWs[177]
$MgCl_2$	AlN	NWs[178]
NiO	GaN	NWs[179]

WZ-structured 1D group III-nitride nanostructures usually grow along [0001] (*c*-axis), with a hexagonal section and six $(10\bar{1}0)$ facet surfaces. For example, Wu et al.[175] fabricated [0001] orientated AlN NBs by CVD using the $CoSO_4$ catalyst. The rectangular cross section of the AlN NBs were 30 - 500 nm in width and ~100 μm in length.

On the other hand, the catalyst also plays an important role in the growth of III-nitride nanostructures with abnormal crystal orientation. Wu et al.[180] synthesized the AlN NWs by CVD using $Ni(NO_3)_2$ catalyst. Before the growth, Al powder and $Ni(NO_3)_2$ were mixed in an ethanol solution, and Ni coated Al powders were obtained after the ethanol evaporated at RT. After the growth, the long axis of AlN NW was at ~ 40° relative to the [002] direction or nearly perpendicular to [002] direction for different NWs. Meanwhile, the diameters of the NWs were heavily dependent on the size of the Ni-Al alloy droplets formed in the growth process. Moreover, the NWs had a uniform single-crystalline core surrounded by an amorphous coating. AlN NWs with an unusual [101] growth direction was obtained by using W-catalyst.[160] The W catalyst was proposed to be responsible for the unusual growth direction due to the decreased total energy of the NWs and comparatively high degree of supersaturation in the system resulted from the high growth temperature and excess Al source. GaN nanostructures along [100] direction[179] and [010] direction[171] were fabricated using NiO and Fe/B_2O_3 as the catalysts, respectively. InN NWs along [100] [181] and [110] [182] directions were synthesized by CVD using Au as the catalyst. Monodispersed [100]-AlGaN NWs on Si(100) substrates were reported by CVD in the Au-assisted VLS process.[143]

Hong et al.[146] reported the Au-assisted CVD growth of InGaN NWs, and found that the growth orientation was along [100] at low In vapor pressure growth and transformed to [001] direction at high In vapor pressure. Based on the above discussion, the growth direction of the III-nitride nanostructures was affected by the different types of catalysts and experimental parameters.

In a word, the catalyst-assisted CVD method generally provides an effective way to control the size and composition of 1D group III-nitrides nanostructures by using various catalysts. Appropriate selection of the catalysts is significant to stimulate CVD-growth process and produce high-quality group III-nitride nanostructures for desired applications. Nevertheless, it is almost certain that the foreign metal catalysts or precursors employed in the growth process remain as a part of the as-synthesized nanostructures, which may induce deep trap states and stacking faults, thereby reducing minority carrier lifetime and optical quality of the III-nitride. As a result, some post-treatments are necessary to remove the remaining metal catalyst for high purity.

3. Properties of III-nitride nanostructures

Group III-nitride nanostructures are expected to possess novel properties due to dimensionality and size confinement. In this section, physical properties including Raman, luminescent and electronic properties of nitrides nanostructures are discussed in details.

3.1 Raman scattering

For the WZ structure, group theory predicts that there are eight sets of normal phonon modes at the Γ point, $\Gamma_{acoustic}+\Gamma_{optical}=(A_1+E_1)+(A_1+2B_1+E_1+2E_2)$.[183] Among the six optical phonons, two E_2 modes are only Raman active, A_1 and E_1 modes are both Raman and IR active, and the two B_1 modes are neither Raman nor IR active (silent). Most studies focused on the E_2^2 and A_1(LO) modes of group-III nitrides.

Six Raman active modes may present in WZ binary group-III nitrides, i.e., $1A_1$(TO) + $1A_1$(LO) +$1E_1$(TO) + $1E_1$(LO) + $2E_2$.[24] Figures 12(a)-(c) show the typical RT Raman spectra of AlN NWs,[184] GaN NWs,[185] and InN NTs,[33] respectively.

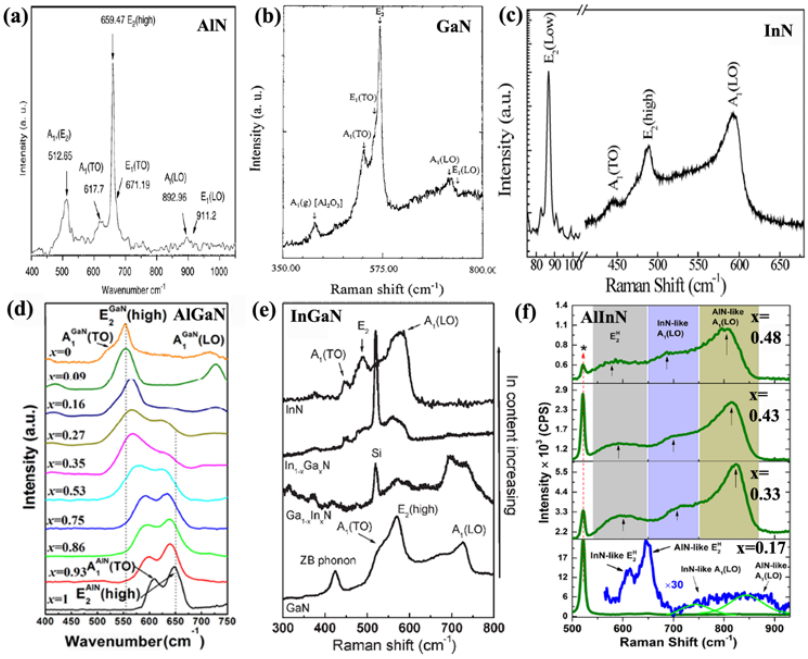

Figure 12 The representative Raman spectra of group-III nitride nanostructures: (a) AlN NWs,[184] (b) GaN NWs,[185] (c) InN NTs,[33] (d) $Al_xGa_{1-x}N$ NWs,[66] (e) $In_xGa_{1-x}N$ NWs,[145] (f) $Al_{1-x}In_xN$ NWs.[186]

Two-mode behavior of the E_2(high) Raman phonon in ternary alloyed nitride NWs was classified. The first-order Raman spectra of the alloyed ternary crystals comprised both AlN- and GaN-like vibrational modes in AlGaN NWs,[187] as shown in Figure 12(d), of which the wavenumbers of both E_{2h} modes are peaked in between those of pure GaN and AlN. With the increase of Al content (x), both the AlN- and GaN-like E_{2h} modes shift to low frequency. Similar behavior can be observed in A_1(TO), E_2, and A_1(LO) modes of InN in In-rich $In_{1-x}Ga_xN$ sample and the E_2(high) and A_1(LO) modes of GaN in the Ga-rich $Ga_{1-x}In_xN$ NWs[145], as provided in Figure 12(e). As exhibited in Figure 12(f), Al-rich $Al_{1-x}In_xN$ (x = 0.17) sample presents a clear splitting of E_2(high) mode into InN- and AlN-like two-modes whereas In-rich $Al_{1-x}In_xN$ samples (x = 0.33 - 0.48) show single mode behavior for E_2(high) phonons and two-mode behavior for A_1(LO) phonons. In addition, with decreasing In composition, the peak positions of AlN-like and InN-like A_1(LO) and E_2(high) modes shift to high frequency. [186]

On the other hand, Raman scattering is a feasible approach to access the stress between group III-nitride nanostructures and substrate. Our group studied the stress states of AlN NRs on Si and its effect on Raman scattering.[59] Figure 13 shows the typical Raman spectra of

the AlN NRs. Two fingerprint phonons of hexagonal AlN, A_1(TO) (612 cm^{-1}) and E_2(high) (656.5 cm^{-1}) are observed. The Raman shift of E_2(high) mode indicated the presence of internal stress and the line broadening of the E_2(high) mode suggested the existence of the defects. E_2 mode of WZ-AlN would shift to a higher frequency under the biaxial compressive stress within *c*-axis-oriented AlN. In the linear approximation, the deviation in frequency of a given phonon mode γ under symmetry-conserving stress could be expressed in terms of the biaxial stress σ_{xx} [59,188]:

$$\Delta\omega_\gamma = \kappa_\gamma \sigma_{xx} \qquad (13)$$

where K_γ is the linear stress coefficient and is taken as 3.39 cm^{-1}/GPa. In the case, Raman shift of each active mode is determined using the mixed Gussian and Lorentzian line shape fitting. The blue shift of the E_2(high) mode demonstrated that AlN NRs grown on the Si substrate were under compressive stress. From the FWHM and peak positions of A_1(TO) and E_2(high) modes of AlN NRs in the range of 80 - 300 K, the changes in the Raman line position, FWHM of the line, and intensity were clearly evident.

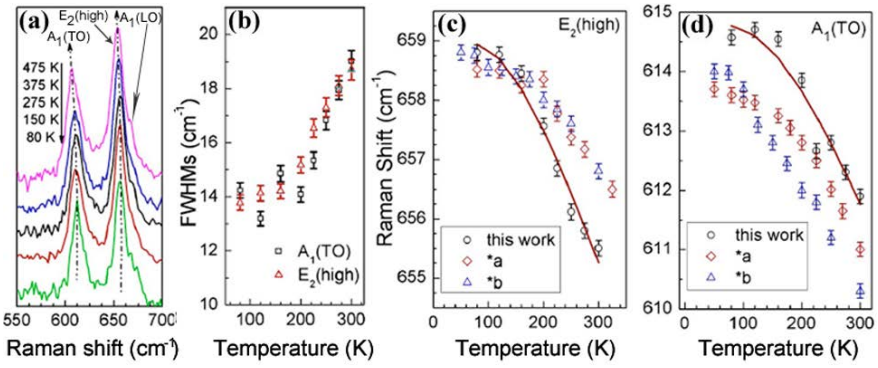

Figure 13 (a) Raman spectra of the AlN NRs at selected temperatures; (b) FMWHs of A_1(TO) and E_2(high) modes in dependence on the temperature; (c) and (d) Raman shift of E_2(high) and A_1(TO) modes of the AlN NRs as a function of temperature. [59]

The effects of temperature on the phonon energy measured by Raman scattering were primarily due to the thermal expansion of the lattice, and a downshift of phonon frequency with temperature is expected. The corresponding temperature-dependent frequency shifts of the A_1(TO) and the E_2 modes for bulk (stress-free) AlN [189-190] are displayed in the figures. According to the empirical formula (14),

$$\omega(T) = \omega_0 - \frac{A}{e^{B(hc\omega_0/k_BT)} - 1} \qquad (14)$$

where ω_0 is the Raman photon frequency at 0 K and ω_0, A, and B are fitting parameters, the experiment data for both A_1(TO) and E_2(high) modes are well fitted. The work suggested that different thermal expansion between the Si substrate and AlN NRs was the key contribution to the compressive stress in the NRs. The lower the temperature, the less the Si substrate effects on the AlN NRs phonons.

In InN NWs, the linear pressure coefficients and Grüneisen parameters of InN NWs phonons under high pressure were reported.[191] The reversible transition between the WZ and rocksalt phases of the InN NWs occurred at ~14.6 GPa. Unpolarized Raman spectra of InN nanostructures obtained at different temperatures possessed three prominent symmetry allowing E_2(low), E_2(high) and A_1(LO) Raman modes in 83 - 88, 485 - 489 and 581 - 593 cm^{-1}, respectively. [192] The frequency and line shape are sensitive to the electron density and mobility of carriers in the system. A continuous increase in the polar A_1(LO) to non-polar E_2(high) peak intensity ratio as the growth temperature increasing was attributed to the polarization of LO mode in the A_1 symmetry along the *c*-axis. The broadening of E_2(high) mode in the Raman analysis showed the development of a biaxial strain in the samples due to the unintentional impurity doping with the increase in the growth temperature.

For RE-, TM-, and metal-doped group III-nitride nanostructures, slightly shifting and broadening in Raman modes were observerd. Figure 14(a) displays Raman spectra of Cu-doped AlN NRs. [193-194] Two prominent phonon modes of hexagonal AlN, E_2(high) and A_1(TO), are centered at 661 and 617 cm^{-1}, respectively, while a broad peak at 893 cm^{-1} is assigned to A_1(LO). The slight red shift of E_2(high), A_1(TO), and A_1(LO) of the AlN:Cu NRs relative to those of the undoped AlN NRs is ascribed to the disorder of the crystals resulted from the incorporation of Cu. Similar observation in AlN:Sc six-fold symmetrical hierarchical nanostructures,[27] AlN:Cu whiskers,[195] and GaN:Si NWs[196] are provided in Figure 14(b)-(d).

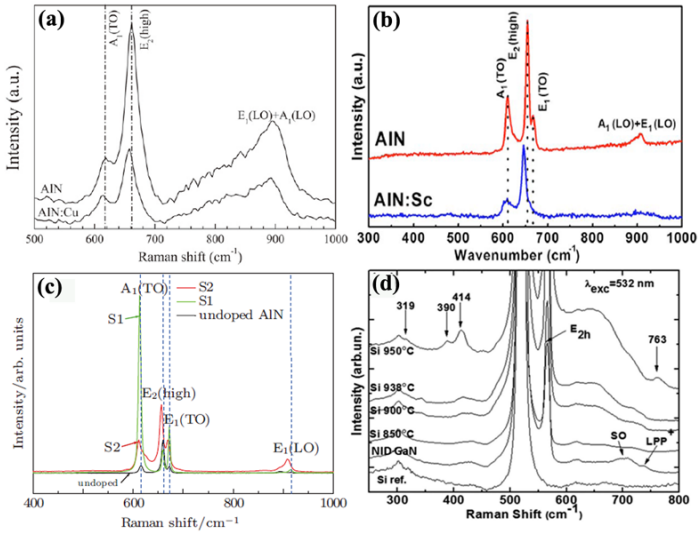

Figure 14 The typical Raman spectra of the doped group III-nitride nanostructures: (a) AlN:Cu NRs,[193] (b) AlN:Sc six-fold symmetrical hierarchical nanostructures,[27] (c) AlN:Cu whiskers,[195] and (d) GaN:Si NWs.[196]

3.2 Luminescence properties

Light can be emitted *via* a number of luminescent processes, which includes cathodoluminescence (CL), photoluminescence (PL), electroluminescence (EL), electrochemiluminescence (ECL) and thermoluminescence (TL).[197-200] Table 3 lists the typical types of luminescence and their origins. In this section, typical luminescence properties of group III-nitride nanostructures, including PL and CL, are presented.

Table 3 Different types of luminescence[197]

Luminescence	Caused by
Photoluminescence (PL)	Photo-excitation of compounds
Cathodoluminescence (CL)	Electron-excitation of compounds
Electroluminescence (EL)	Radiative recombination of electrons and holes in a materials after an electrical current passes through them or a strong electric field is applied
Electrochemiluminescence (ECL)	Electrogenerated chemical excitation
Thermoluminescence (TL)	Detrapping process caused by heating or thermostimulation

3.2.1 Photoluminescence

3.2.1.1 AlN

The band-edge emission of 6.18 eV from MBE AlN NWs was reported by Landré et al., which is similar to bulk and epilayers.[201] Shi et al.[125] compared the PL properties of bulk and nanocrystalline AlN (nanotips) under near band-edge (6.05 eV) excitation, as shown in Figure 15(a) and (b). The commercially obtained AlN ceramic micropowders showed a broad peak centered at 3.2 eV with a significant low energy shoulder. In contrast, the AlN nanotips displayed a blueshifted PL peak at ~3.4 eV, which was comparatively narrower due to the absence of the low energy shoulder. Two defect related transitions of O_N-V_{Al} complex at ~2.1 eV and separated O_N at 3.4 eV were identified by PLE analysis, as described in Figure 15(b). Temperature-dependent PL of AlN nanotips was reported by Ji et al.[58], as shown in Figure 15(c) and (d). The single-crystalline WZ AlN nanotips showed three PL peaks centered at 3.28 eV, along with a weak shoulder located at 4.32 eV and an even weaker near band-edge emission at 5.83 eV from the PL spectra measured at 10 K and 300 K. From the enlarged view of the temperature-dependent PL of the 5.83 eV emission, the peak position exhibitsed no shift with the decrease in the temperature due to indirect transition between the electron in the conduction band and the deep level.

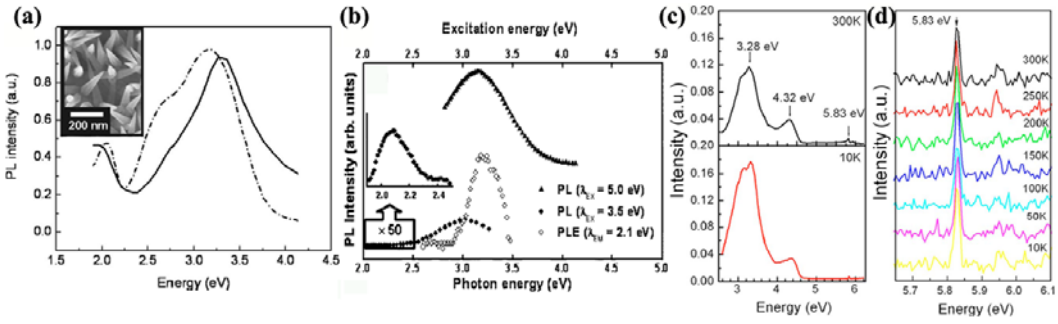

Figure 15 (a) PL spectra for AlN (·−·) ceramics and (—) nanotips, under an excitation of 6.05 eV, the inset showing the SEM image; (b) RT PL and PLE spectra of AlN nanotips;[125] (c) temperature-dependent PL spectra of the sample measured at 10 and 300 K; (d) an enlarged view of the temperature-dependent PL plot of the 5.83 eV emission.[58]

For AlN, N deficiency and O point defects might result in the blue or green emissions in the range of 365 - 520 nm, and the peak position was strongly dependent on O concentration.

Peak position of O point defects usually displayed an obvious red shift toward the direction of long wavelength with O content increase. The PL properties of some AlN nanostructures are summarized in Table 4.

Table 4 PL properties of AlN nanostructures

Origin	PL peak/nm	Nanostructures
Surface defect states	517[202], 523[203]	NWs
	564[204]	Nanowiskers
Oxygen impurity	434[205], 371.8 and 431.8[206]	NWs
	479[207]	6-fold-symmetrical hierarchical nanostructures
Nitrogen vacancy	450.6[206], 479[208], 506[209]	NWs
	481[24]	Nanocones
	416[204]	Nanowiskers
Recombination of a photogenerated hole with an electron occupying the nitrogen vacancies	573[210]	NBs
Transition from O_N- V_{Al} complex to the separated O_N ion level	365[125]	Nanotips
Al_i defect/complex defect of V_NAl_i	430/600[211]	Helices-like nanostructures
V_{Al} or donor-acceptor pair (DAP) recombinations associated with V_{Al}	264[212]	NTs
Transition from the shallow level of nitrogen vacancies (V_N) to the ground state of the deep level of the defect (V_{Al}^{3-}-3×O_N^+)	413[202], 590[213]	NWs
	410[210]	NBs
	590[125]	Nanotips
	480[204]	Nanowiskers

3.2.1.2 GaN

The direct bandgap and the main defect-related emission of GaN are 3.4 eV and 2.25 eV in general. However, the shifting of the PL emission with the growth direction and the dimension of the GaN nanostructures were reported. [164, 214-215] Kuykendall et al.[164] found the emission of GaN NWs grown along [1$\bar{1}$0] was blue-shifted by ~100 meV from that along [001] directon as presented in Figure 16. The shift in emission was ascribed to the clear manifestation of the difference in polar [001] and non-polar [1$\bar{1}$0] directions within the WZ GaN crystal structure. The presence of spontaneous polarization in GaN had a drastic impact

on electron-hole overlap, radiative lifetime, and subsequent emission wavelength and quantum efficiency. In addition, the difference in tensile stress and defects experienced by NWs grown along different directions could also contribute to the novel emission.

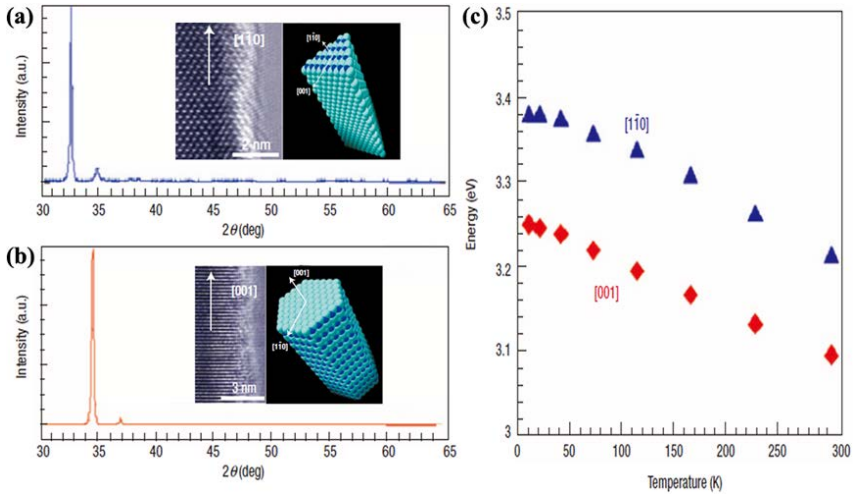

Figure 16 (a)-(b) The XRD pattern, HRTEM and space-filling structural model of the GaN NWs with (a) triangular top grown on γ-$LiAlO_2$ substrate and (b) hexagonal top grown on MgO substrate; (c) temperature-dependent PL collected on the two sets of GaN NWs with different growth directions.[164]

Zettler et al.[214] reported the RT PL emission at 3.412 to 3.454 eV from ultrathin epitaxial GaN NWs by thinning MBE-grown NW ensembles through a postgrowth thermal decomposition process. The diameter of the NW was as small as 6 nm. As present in Figure 17(a), the PL peak energy of GaN NWs increases with progressive decomposition. The dielectric confinement of the exciton becomes noticeable for diameters of $5a_B$ (exciton Bohr radius, and a_B was 3 nm for GaN). This observation was a signature of dielectric confinement. The radial dielectric confinement of the exciton becomes stronger with decreasing d_B. Consequently, the PL line of thinned NWs is blueshifted. As a result, the emission broadening increases with decreasing d_B.

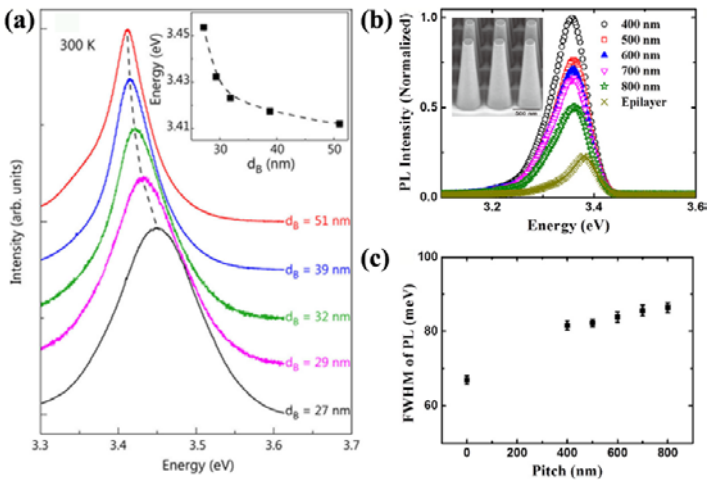

Figure 17 (a) PL spectra at 300 K from an ensemble of the as-grown GaN NWs (top spectrum) and from partially decomposed GaN NW ensembles with different average base diameters d_B, the inset showing the relationship of peak energy and d_B;[211] (b)-(c) PL spectra of GaN NP arrays with varying pitch (b) and FWHM of the PL as a function of array pitch (c).[212]

The PL property of GaN NP arrays with a pitch of 400, 600 and 800 nm by top-down approach was reported by Reddy et al.[215] Figure 17(b) shows the RT PL spectra of the NP arrays and the epilayer. The emission peak of the NP arrays red shifts as compared with that of the epilayer, which is invariant with pitch. This red shift of the peak position was due to the partial strain relaxation of NPs. However, the emission intensity of the NP arrays reduces with increasing pitch from 400 nm to 800 nm, which is the result of variation in the QE of the NPs or variation in light absorption and collection efficiency. The slightly larger PL linewidth as compared to the epilayer is originated from the strain variation along the length of the tapering NP.

Based on the above, the PL emission of GaN nanostructures was not only influenced by the growth direction of nanostructures, but also the diamension of the nanostructures. The PL properties of some GaN nanostructures are summarized in Table 5.

Table 5 PL properties of GaN nanostructures

Origin	PL peak/nm	Nanostructures
Near or bandgap emission of wurtzite GaN	364.7[165], 363.5[216], 357[217], 379[218], 374[179]	NWs
	358[219], 369[220]	NRs
Bandgap emission of cubic GaN	396[218], 400[165]	NWs
Deep level defects	367[218], 460[179]	NWs
Surface defects	359[217]	NWs

Conduction band edge to a localized state	539[165]	NWs
Transition between shallow donors (V_N, Ga_I) and deep levels (V_{Ga})	552[220]	NRs
Excitons bound to planar defects	362[217]	NWs
Recombination of bound excitons	378[158]	NWs

3.2.1.3. InN

InN has a direct band gap of ~0.6 - 0.7 eV at 300 K, which ensures the distinct IR emission of ~1700 nm. PL emission at ~0.68 eV from non-tapered InN NWs was demonstrated by Chang et al.[221], as shown in Figure 18. The PL FWHM increased from ~ 13 meV to 60 meV and the peak energy shifted from ~0.68 eV to 0.715 eV as the increase of laser power, attributing to the filling of the energy band states by photogenerated carriers. The red shift of the peak energy with increasing temperature was ascribed to the lattice dilation in spite of the relatively high laser power. Similar temperature dependent PL properties was observed from InN nanotubes, and the carrier concentration of the InN nanotubes was estimated. [222]

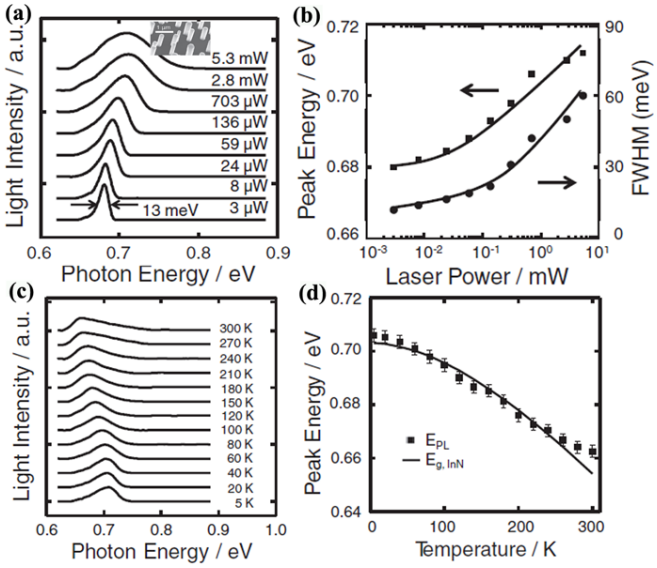

Figure 18 (a) Normalized PL spectra of a single InN NW measured under a range of laser powers at 5 K, inset showing the corresponding SEM image; (b) variation of the PL spectral linewidth and peak energy versus the laser power; (c) normalized PL spectra of a single InN NW measured at different temperature with a laser power of ~0.7 mW; (d) variation of the PL peak energy with temperature and the fit using the Varshni's equation (solid line).[218]

As shown in Figure 19, the RT-PL exhibits an emission band centered at 0.68 eV and the emission peak shows a blue-shift to 0.71 eV as temperature is lowered to 20 K. The narrowed FWHM of PL emission at RT indicated a suppressed band filling effect due to the low impurity incorporations. The relationship between the FWHM and free-electron concentration can be well described by the empirical formula given by

$$\log(FWHM) = 0.50737\log(n) - 7.5988 \quad (15)$$

The carrier concentration, n, was estimated to be 3×10^{18} cm^3. The area of the PL peak depended on the excitation power Φ approximately as $\sim\Phi^m$. It yielded a m value of 1 at 20 K, which was consistent with the near band edge PL in direct bandgap semiconductors. The PL emission and their originations of some InN nanostructures are given in Table 6.

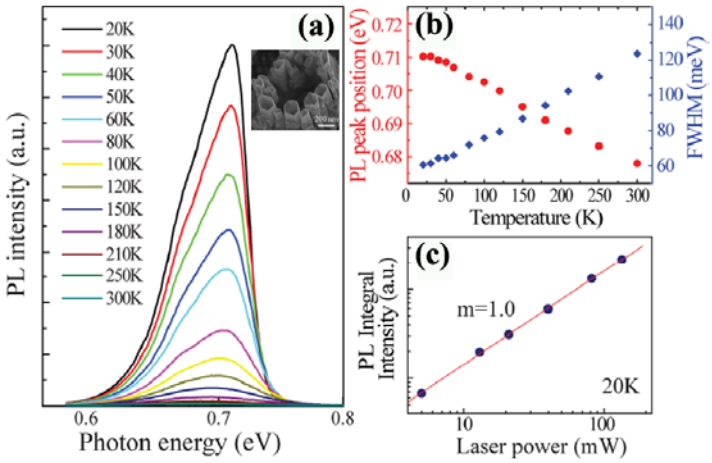

Figure 19 (a) Temperature-dependent PL spectra of InN NTs, inset showing the SEM image of InN NTs; (b) PL peak position and FHWM as a function of temperature, and (c) the laser power dependence of the peak intensity measured at 20 K.[219]

Table 6 PL properties of InN nanostructures

Origin	PL peak/nm	Nanostructures
Band-edge emission	1653[223], 1619[224]	NRs
	1631[225], 1660[226]	Nanobelts
	670[227], 652[228], 707[229], 1754[230], 651[231], 1698[232]	NWs
	640[233], 700[234]	Nanotubes
	1127[235]	Nanofingers
Interband emission	1968[236]	NRs
High electron concentration	780[237], 1590[238]	Nanocolumns

Band-to-deep acceptor transition or phonon side band emission	2000[239]	Micro-mushrooms
Electrons at the bottom edge of the conduction band recombine with localized holes in the acceptor level	1823[239]	
Electrons near the Fermi energy recombine with localized holes in the acceptor level	1722[239]	

3.2.1.4 Ternary III-nitride alloys

(1) InGaN

The tunable bandgap of $In_xGa_{1-x}N$ is in the range of 0.65 ~ 3.4 eV, thus the PL of $In_xGa_{1-x}N$ nanostructures can potentially covers the whole visible range by alloying and modifying the chemical compositions. Yang et al. realized $In_xGa_{1-x}N$ NWs in the whole composition range by halide-assisted CVD method, and some of the results are shown in Figure 20(a)-(c).[37] The color CCD images were taken at regular intervals along the substrate and exhibited the vibrant colors emitted in the visible spectrum region. The PL emission of $In_xGa_{1-x}N$ NWs with the x in the range of 0 ~ 0.6 shift to longer wavelengths from 325 nm to 850 nm with increasing In concentration (x). Furthermore, the compositions determined by PL, absorption and EELS was almost in agreenment with bowing fit, as shown in Figure 20(c).

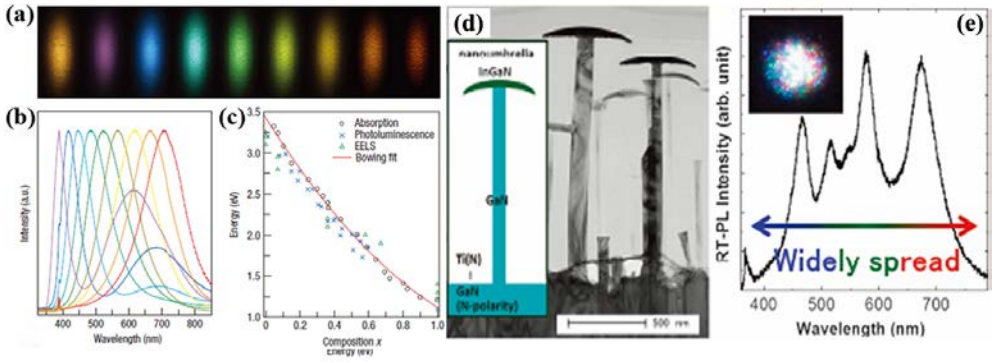

Figure 20 (a) Color CCD images of the $In_xGa_{1-x}N$ NWs ($0 \le x \le 1$), (b) visible PL emission (x =0-0.6), (c) energy plotted as a function of In concentration x determined by EDS for PL, absorption and EELS and bowing equation fit to absorption spectra;[37] (d) TEM image of the InGaN nanoumbrella and the corresponding schematic illustration; (e) typical RT-PL spectrum obtained from the high-density nanoumbrella array, the inset showing the RT-PL imag.[240]

White light emission from the designed InGaN nano-umbrellas, consisting of bending InGaN nanoplates and supporting GaN nanocolumns, was demonstrated by Kouno et al.[240] Figure 20(d) and (e) show a TEM image and the RT-PL spectrum of InGaN nano-umbrellas, respectively. The emission wavelength covered the entire visible-light from ~360 to 800 nm, which was likely originated from the nonuniform configurations of the bending nanoplates of the nanoumbrellas.

(2) AlGaN

$Al_xGa_{1-x}N$ nanostructures with x in the range of 0 - 1 possess a tunable bandgap from 3.4 to 6.2 eV, which can potentially cover from blue to deep ultraviolet. PL performance of AlGaN NWs was investigated by Pierret et al. as shown in Figure 21(a)-(e).[93] When Al composition was less than 50%, the PL spectra at 5 K exhibited only one emission peak, which move towards higher energy as Al content inceasing, as shown in Figure 21(c). However, two well separated peaks were observed from the samples with Al content greater than 50%. One peak (highlighted with points) increased its energy following a similar trend as those samples with low Al content, while the other peak (highlighted with a vertical dotted line) stayed at a constant energy (4.3 eV). The PL peak highlighted with the red point was the band energy emission of AlGaN NWs with different compositions. Micro-PL spectra from a few (~5) NWs shown in Figure 21(d) and (e) proved that the 4.3 eV emission band was due to localized states.

Zhao et al.[241] reported RT-PL of RF-MBE grown GaN/AlGaN NWs as schematic in Figure 21(f)-(h). The RT-PL emission wavelength exhibited a progressive blueshift with increasing substrate temperature. Al composition (x) was estimated approximately by the RT-PL peak energy (E_{PL}) *via* $E_{PL}(x) \approx E_g(x) = (1-x)E_g(GaN) + xE_g(AlN)-bx(1-x)$, where E_g is the bandgap energy, and b is bowing parameter (1 eV), $E_g(GaN)$ and $E_g(AlN)$ are 3.4 and 6.2 eV, respectively. The PL peak wavelength *vs*. Al content x presented in Figure 21(h) is consistent with the reports.[93, 242]

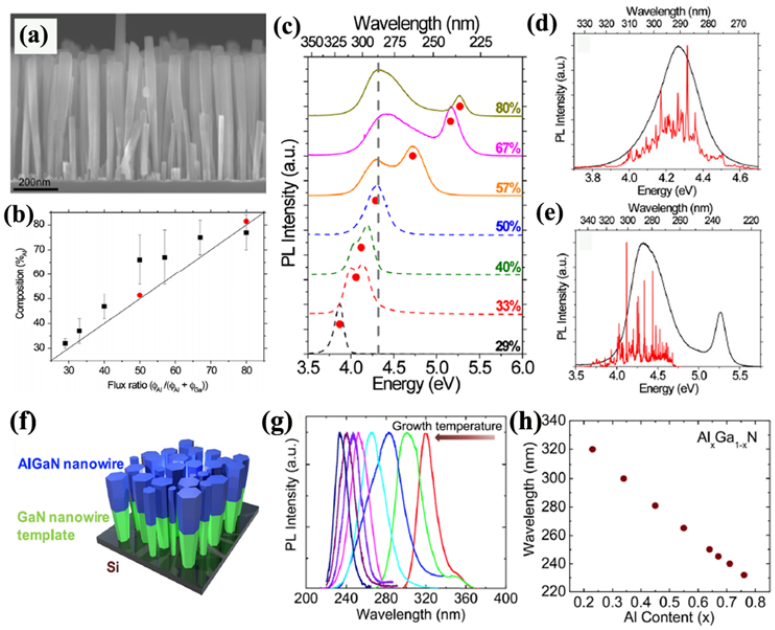

Figure 21 (a) Typical SEM image of the AlGaN NWs on GaN NWs; (b) composition of the AlGaN NWs deduced by Raman (squares) and XRD (circles) studies; (c) PL of the samples with different compositions at 5K; PL of an ensemble of (black, λ_{exc}=193 nm) and of a few (red, λ_{exc}= 244 nm) nominal (d) $Al_{0.5}Ga_{0.5}N$ and (e) $Al_{0.8}Ga_{0.2}N$ NWs at 5 K;[93] (f) Schematic of AlGaN NWs grown on a GaN NW template; (g) PL spectra of samples grown under different substrate temperatures (895 °C to 960 °C); (h) PL peak wavelength *vs.* Al content.[241]

The monolithic integration of three-primary-color (RGB) LEDs using a nitride semiconductor is a very important issue for full-color applications. A novel technology for controlling the In composition of InGaN quantum wells on the same wafer was developed by Sekiguchi et al.[243] PL near-field emission images of the InGaN/GaN NC arrays show NC diameter-dependent tunable emission color in full visible range, as shown in Figure 22 (a)-(f). Double-peak emissions are observed from RT micro-PL spectra of the NC arrays with different diameters [Figure 22 (g)]. The two peaks at longer wavelength side originated from sixfold side faces and the shorter one from angle areas of pyramids. The PL peak wavelength of the longer-wavelength-side monotonically shift from 513 to 632 nm with increasing diameter from 137 to 270 nm.

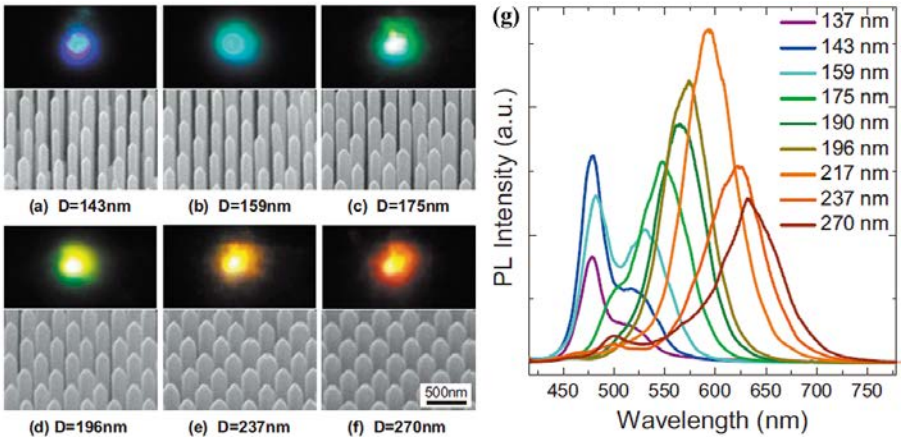

Figure 22 (a)-(f) SEM images and corresponding PL emission images of the InGaN/GaN NCs with different diameters: (a) 143 nm, (b) 159 nm, (c) 175 nm, (d) 196 nm, (e) 237 nm, (f) 270 nm; (g) PL spectra of InGaN/GaN NCs with different diameters.[243]

(3) InAlN

The bandgap of InxA$_{1-x}$lN can be tuned from 0.65 eV to 6.2 eV, covering the light emission from IR to deep UV. In-rich In$_x$Al$_{1-x}$N (x in the range of 0.71 - 1.00) NCs grown by RF-MBE was reported by Kamimura et al.[244] Figure 23(a)-(c) display the SEM images of the In$_x$Al$_{1-x}$N NCs with different In contents. The PL peak energies are 0.692 eV (~1.79 μm) for InN, 0.954 eV (~1.30 μm) for In$_{0.89}$Al$_{0.11}$N, 1.21 eV (~1.02 μm) for In$_{0.8}$Al$_{0.2}$N and 1.39 eV (~892 nm) for In$_{0.71}$Al$_{0.29}$N, as plotted in Figure 23(d). The emission of In-rich InAlN NCs covered a wide spectral region of the optical communication wavelength of 1.3 - 1.7 μm. The inset of Figure 23(d) shows the dependence of LT-PL peak energy on x_{In}. The peak energies were fitted using the expression E_g (x) = x E_g (InN) + (1-x) E_g (AlN) - bx(1-x). The bowing parameter b was optimized to be 4.08 eV, which was considerd to be consistent with both experimental data[245-246] and theoretical calculations[13, 247].

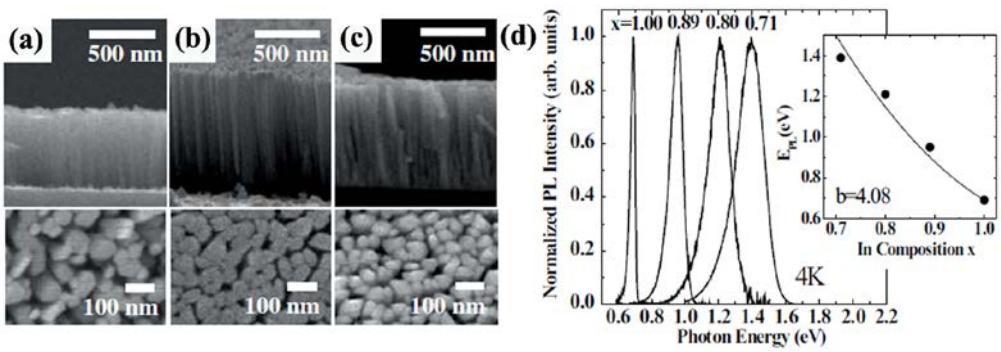

Figure 23 (a)-(c) Cross-sectional and top-view SEM images of In$_x$Al$_{1-x}$N NCs with different x,

(a) 0.92, (b) 0.81, (c) 0.71; (d) the PL spectra of the corresponding samples at 4 K, the inset showing the variation in PL peak energy as a function of In composition x.[244]

3.2.2 Cathodoluminescence (CL)

Cathodoluminescence (CL) is an optoelectrical phenomenon wherein a beam of electrons is generated by an electron gun and is interacting with a luminescent material, such as phosphor, causing the material to emit light. It is a useful technique for characterization of the optical properties of the nanostructures because of its high spatial resolution and structural information obtained by using SE imaging. Table 7 summarizes the CL properties of group III-nitride nanostructures.

Table 7 Cathodoluminescence of group III-nitride nanostructures

Composition	Nanostructures	Emission/nm(eV)	Ref.
AlN	Nanotips	(2.1, 3.4, 6.07, 6.2)	[125]
	Nanotubes	(2.3,2.8,3.4,3.7,4.0)	[248]
	Nanowiskers	352,722	[249]
	Nanorods	(2.9, 3.48)	[250]
	Nanowires	357, 436, 550	[251]
GaN	Nanorods	(2.2, 3.4)	[252]
	Nanorods	(2.25,2.67,3.25)	[253]
	Nanorods	(2.2, 3.3)	[254]
	Nanowires	370, 410, 510	[255]
	Nanowires	(2.1, 2.74, 3.2)	[256]
	Nanowires	369, 650	[257]
InN	Nanorods	(0.65)	[258]
	Nanowires	(1.38, 1.7)	[259]
AlGaN	Nanocones	308~366	[36]
	Nanowires	(4.15~5.50)	[260]
InGaN	Nanorods	(2.64~3.26)	[261]

The representative CL spectra of AlN, GaN, and InN nanostructures are shown in Figure 24. A strong CL emission band centered at 3.4 eV accompanied with a weak emission at 2.1 eV are observed from AlN nanotips[125]. The 3.4 eV peak was related to O substitution of N in the AlN lattice, and the 2.1 eV emission band was originated from the N vacancies and Al interstitial point defects. In addition, the band edge splitting of AlN is observed as shown in the inset of Figure 24(a). Figure 24(b) is a typical CL spectrum of GaN NWs, showing strong

NBE luminescence at ~357 nm, along with weak defect-related blue luminescence at ~436 nm and yellow luminescence at ~550 nm.[251]

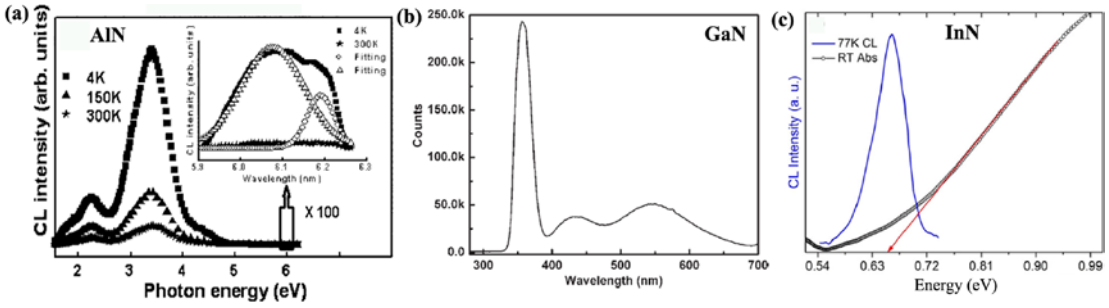

Figure 24 (a) The representative RT CL spectra from the AlN nanotips, the inset showing the near band edge transition;[125] (b) the RT CL spectrum of GaN NWs;[251] (c) CL emission and optical absorption spectra of InN NRs.[258]

Liu and co-workers verified the origin of yellow-band CL emission in GaN NWs was arised from dislocation threading in GaN−sapphire interface in the case of carbon free case.[257] Figure 25(b) and (d) provide the CL spectra of the GaN NWs grown on Au/Sapphire [Figure 25(a)] and Al/Au/Sapphire [Figure 25(c)]. The CL spectrum in Figure 25(b) exhibits the strong UV (369 nm) and weak visible (650 nm) emission, while the CL spectrum in Figure 25(d) only possesses a predominant narrow sharp emission peak at ~369 nm. They indicated that the 369 nm UV emission in Figure 25(b) and (d) was attributed to near-band-edge emission, and the broad yellow-band luminescence was originated from the dislocation induced by epitaxial growth.

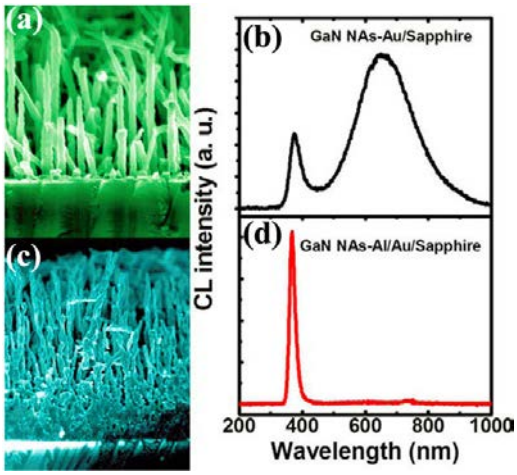

Figure 25 Typical SEM images and CL spectra of the GaN NWs grown on Au/Sapphire (a)-(b) and Al/Au/Sapphire (c)-(d).[257]

The band edge emission of ~0.65 eV of InN NRs was observed from CL measurement at 77K [Figure 24(c)], as Tangi et al. reported.[258] Spatially resolved CL investigation of the InN NRs was employed by Tessarek et al. to verify the optical activity.[262] As shown in Figure 26, the CL spectra of InN NRs with different diameters exhibit decreased emission energy as the diameter of NRs increasing. The relationship between the CL peak position *vs* the NR diameter proved that the InN NRs had an In droplet on top and free sidewall facets due to the passivation effect of In, which futher modified the surface electron accumulation layer of the InN NRs. The blue-shifted near band emission of CL spectra was ascribed to the high carrier concentration of ~10^{19} cm^{-3}.

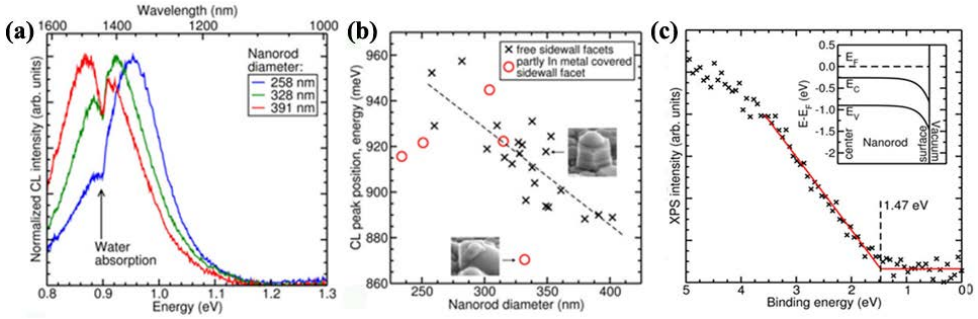

Figure 26 (a) CL spectra of three single NRs with varying diameters in one sample; (b) comparison between the NR diameter and CL peak position. The black and red circles were measurements on NRs without and with partly In metal covered sidewall facets, respectively; (c) XPS spectrum of the InN NR. The difference between the valence band maximum (located at 0 eV) and the near-surface Fermi level was 1.47 eV. The inset sketched the conduction and valence band (E_C and E_V) profile with downward band bending close to the surface.[262]

CL properties of InGaN/GaN MQW heterostructure NWs was investigated by Ra et al.[263], as shown in Figure 27(a)-(f). The CL spectrum of an InGaN/GaN MQW single NW exhibited two emission peaks at 440 and 369 nm, ascribing to InGaN and GaN, respectively, and an additional peak at 480 nm was also observed. CL mapping image of the whole single NW displayed uniform luminescence of the NW's body part, whereas slightly darker luminescence of the pyramidal top portion. Figure 27(c) represents the CL emission at 369 nm from both the *m*-plane and *r*-plane, which are different with the distinct CL characteristic peaks at 440nm of *m*-plane and 480 nm of *r*-plane. The significant difference in the CL

emission was ascribed to compositional differences in these regions. The In composition of the *r*-plane region was higher than that at the *m*-plane region, resulting in the red-shift (480 nm) in the CL emission spectrum. The spatially resolved CL mapping images demonstrated that *n*-GaN was uniformly distributed over the entire core region of the NW, the 440 nm emission was originated from the *m*-plane InGaN/GaN MQW NW region, and the 480 nm bright luminescence was ascribed to *r*-plane at the top region of InGaN/GaN MQW NW. The composition-dependent CL emission and the presence of polarization-induced effects of the *m*-plane and *r*-plane MQW NWs were confirmed by the power-dependent CL spectra.

Spatially resolved CL measurement was also used to characterize the composition fluctuation in a single InGaN/GaN NC, as shown in Figure 27(g)-(i).[264] LT-CL spectra of a single InGaN/GaN NC in Figure 27(g) show the spectral features due to variations of the In% and/or strain in each NC. The corresponding spatially resolved CL images display a red shift when moving towards the NC top, pointing to an axial increase of the In composition. The CL emission peak at 2.85 eV seemingly originating from the InGaN/GaN interface region was backing up the previous picture of a low In incorporation until the onset of strain relaxation occurred above a certain critical thickness. The spatially resolved CL data at 10K from a single NC showed a monotonic decrease of energy from 2.98 eV in the middle-low nanocolumn region down to 2.12 eV at the NC apex due to the growth temperature gradient.

Ristić et al.[265] reported the low-temperature in-depth CL performance of the AlGaN NCs with/without GaN QDs. By increasing the electron beam energy gradually from 3 to 25 keV, the CL peak intensity of InGaN without QDs increased with the penetration depth without changing its energy position. However, the emission from the GaN QDs (3.62 eV) was dominant at low penetration depths. The AlGaN peak became stronger and finally was dominant as the electron probe going deeper since the probe was averaging over the whole sample volume.

In a word, CL analysis precisely determined the spatial luminescence distribution of pure group III-nitride and *p*-*n*-junctioned nanostructures, as well as the optical properties of the quantum discs in 1D nanostructures.

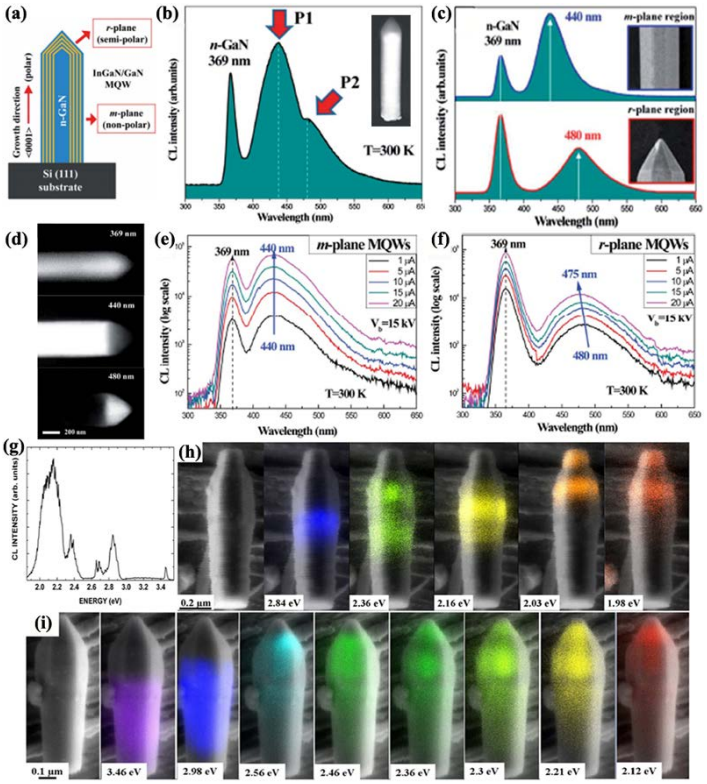

Figure 27 (a) Schematic illustration of a single coaxial InGaN/GaN MQW/n-GaN NW; (b) CL spectrum recorded along the entire coaxial NW, inset showing spatially-resolved CL mapping image recorded at 440 nm; (c) spatially-revolved CL spectra of a m- and r-plane-oriented MQW NW, respectively; (d) spatially-resolved CL mapping image of an MQW NW at wavelengths of 369, 440 and 480 nm; (e) and (f) power-dependent CL spectra of m- and r-plane oriented MQW NW, respectively;[260] (g)-(h) 10K CL spectrum and spatially resolved CL mapping from a single InGaN/GaN NC synthesized at 650 °C; (i) 10K spatially resolved CL measurements in a single InGaN/GaN NCs synthesized at growth temperature gradient of 1.67 °C /min from 725 to 625 °C.[264]

3.2.3 Luminensent property of doped III-nitrides

Green emission of Tb-doped AlN NRs was reported by Liu et al.[266] as shown in the PL and CL spectra of Figure 28(a)-(d). The characteristic emission lines of Tb^{3+} ions were observed in both PL and CL spectra. The strongest green emission peak located at 554 nm corresponded to the $^5D_4 \rightarrow {}^7F_5$ transition of Tb^{3+} ions. Other peaks were identified to the following transitions: $^5D_3 \rightarrow {}^7F_6$ (at ~384 nm), $^5D_3 \rightarrow {}^7F_5$ (at ~418 nm), $^5D_3 \rightarrow {}^7F_4$ (at ~442 nm), $^5D_3 \rightarrow {}^7F_3$ (at ~462 nm), $^5D_4 \rightarrow {}^7F_6$ (at ~494 nm), $^5D_4 \rightarrow {}^7F_4$ (at ~591 nm), $^5D_4 \rightarrow {}^7F_3$ (at ~625 nm),

and $^5D_4 \rightarrow {}^7F_2$ (at ~656 nm). Transitions from the $^5D_4$ level to lower ^7F_J levels were much clearer and stronger than those from the $^5D_3$ level to lower ^7F_J levels. The high emission probability from $^5D_4$ was due to cross-relaxation process, which depopulated the excited $^5D_3$ to the $^5D_4$ state. The monochromatic (wavelength ~554 nm) CL images of a cross section, tip surface, and a single Tb-doped AlN NR, respectively, demonstrated that the green emission (554 nm) was from the oriented NRs.

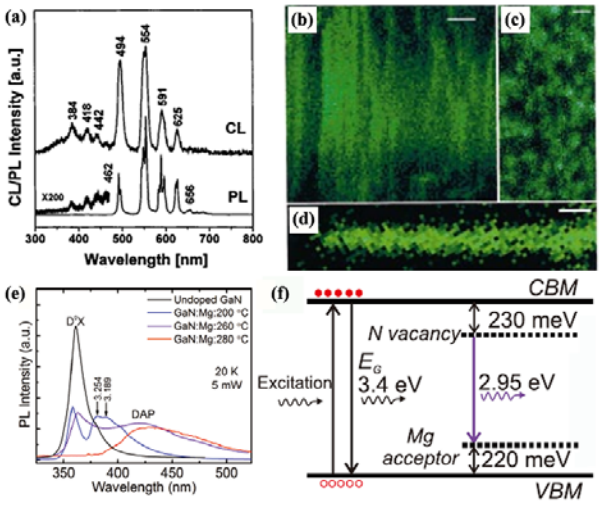

Figure 28 (a) The RT PL and CL spectra of AlN: Tb NRs; (b)-(d) monochromatic (wavelength = 554 nm) CL images of a cross section, a tip surface of AlN: Tb NRs, and single AlN: Tb NR stripped off from the Si substrate;[266] (e) 20 K PL spectra of GaN:Mg NWs in comparison to undoped sample; (f) schematic energy band diagram of GaN:Mg:260 °C NWs illustrating the formation of V_N and Mg related intra-gap states.[267]

Kibria et al.[267] reported the intra-gap defect related energy states of Mg-doped GaN NW arrays, as shown in Figure 28(e) and (f). The pure GaN PL was dominated by a single peak at ~3.435 eV, corresponding to donor-bound exciton (D^0X). For the lightly Mg doped (T_{Mg}=200 °C) sample, in addition to the D^0X emission, two additional peaks were clearly resolved at 3.254 eV and 3.189 eV, which was attributed to the conduction band to Mg-related acceptor level (e-A) transition and Mg related defects in GaN, respectively. The broad emission peak at ~2.95 eV of Mg-doped GaN (T_{Mg}=260 °C) was originated from the donor-acceptor-pair (DAP) transition between the V_N related deep donor states and shallow Mg acceptor states. At T_{Mg}=280 °C, the DAP emission red-shifted with progressive disappearance of the band-edge emission was ascribed to the emergence of high densities of deep energy states and the deterioration of crystalline quality caused by the incorporation of

high densities of Mg. A schematic energy level diagram is described in Figure 28(f). The emission peaks of Mg-related acceptor energy level or defect states are also observed in Mg-doped AlN or InN nanostructures.[268-269]

The optical performance of transition metals, such as Fe and Mn, doped group III-nitride nanostructures were also intensively studied. For example, Ji et al.[270] investigated the DUV PL properties of Fe-doped AlN NRs. The PL spectrum of undoped AlN NRs comprised two strong impurity-related emissions lines at 3.25 and 4.32 eV, and a weak emission at 5.83 eV, as described in Figure 29(a). The emission peaks of 3.25 and 4.32 eV were attributed to the transitions between free or donor-bound electrons to Al vacancy and vacancy-impurity complex (V_{Al}-complex) with different charge states. However, the emission peak of 5.83 eV was related to an unidentified impurity as the peak position did not shift with temperatures from 300 K down to 10 K. It was noted that both impurity emissions were absent from the Fe-doped NRs, but a 3.96 eV emission became apparent in addition to the band edge emission at 6.02 eV. The vanishing of the 3.25 and 4.32 eV emissions was due to the formation of nonradiative defects complex induced by Fe ions. The emission peak of 3.96 eV with narrow linewidth (18.5 meV) was related to $Fe^{3+/2+}$ acceptor. PL measurements on Mn-doped AlN NWs at 10 and 300 K were studied by Yang et al.[271] The as-grown sample exhibited a red luminescence, consisting two intensive emission peaks around 600 and 695 nm. The red-orange band at 600 nm was a characteristic of the luminescence from the Mn center in AlN. The other two peaks were related to the O impurity in AlN. In contrast, the PL spectra of undoped AlN NWs exhibited very weak broad bands located between 550 and 600 nm, as shown in Figure 29(b).

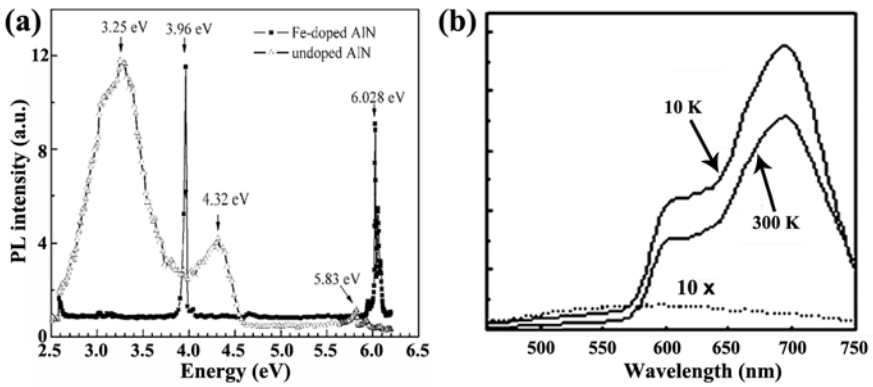

Figure 29 (a) PL spectra of the undoped and Fe-doped AlN NRs;[267] (b) PL measured at 10

and 300K for the Mn-doped AlN NWs (*solid line*) and the undoped AlN layer (*dashed lines*).[271]

In general, the luminescence of the TM-doped III-nitride nanostructures originated from the dopants' themselves and the dopant-related defects. Optical properties of doped 1D group III-nitride nanostructures are listed in Table 8.

Table 8 Optical properties of 1D doped group III-nitride nanostructures

Nanostructures	Emssion peaks and origin	Ref
Tb-AlN nanorods	384 nm: Tb^{3+} $^5D_3 \rightarrow {}^7F_6$; 418 nm: Tb^{3+} $^5D_3 \rightarrow {}^7F_5$; 442 nm: Tb^{3+} $^5D_3 \rightarrow {}^7F_4$; 462 nm: Tb^{3+} $^5D_3 \rightarrow {}^7F_3$; 494 nm: Tb^{3+} $^5D_4 \rightarrow {}^7F_6$; 554 nm:$Tb^{3+}$ $^5D_4 \rightarrow {}^7F_5$; 591 nm: Tb^{3+} $^5D_4 \rightarrow {}^7F_4$; 625 nm: Tb^{3+} $^5D_4 \rightarrow {}^7F_3$; 656 nm: Tb^{3+} $^5D_4 \rightarrow {}^7F_2$;	[266]
Fe-AlN nanorods	3.69 eV: $Fe^{3+/2+}$ acceptor-related emission 6.02 eV: the band edge emission of AlN	[270]
Mn-AlN nanowires	600 nm: luminescence of Mn center in AlN 670 nm, 695 nm: oxygen impurity	[271]
Mn, Cu-AlN nanowires	1.66 eV: shallow levels (N vacancy) to Mn deep levels 2.6 eV: transition from deep levels made by Cu 3.02 eV: oxygen trapped levels	[208]
Mg-AlN nanowires	3.9 eV: transition from a shallow donor to a deep acceptor 4.57 eV: transition from a deep donor to Mg-acceptor energy level 5.34 eV: Mg-acceptor related transition 5.95eV: band-edge emission	[268]
Mg-GaN nanowires	3.189 eV: Mg-related defects 3.254 eV: transition from conduction band to Mg-related acceptor level 3.435 eV: donor-bound exciton	[272]
Mn-GaN nanowires	610 nm: Mn^{2+} $^4T_1 \rightarrow {}^6A_1$	[273]
Mg-InN nanowires	0.61 eV: transition from conduction band to Mg-acceptor energy level 0.67 eV: band-to-band recombination	[269]

3.3 Electrical properties

In order to realize the applications of group III-nitride nanostructures in nanoscale electronic field, it is a crucial step to access the electrical properties of them. In 2002, Lieber's group demonstrated the FET based on a single GaN NW, as illustrated in Figure 30(a).[274] A layer of Ti(50 nm)/Au(70 nm) at the two ends of an individual NW was applied as source and drain electrodes. Gate-dependent current-source drain voltage (I-V_{sd}) data indicated that the GaN NWs were *n*-type and the conductance of FET could be modulated by more than 3

orders of magnitude. Based on the I-V_{sd} and current-source-gate voltage (I-V_g) data, the electron mobilities were calculated to be as high as 650 $cm^2/V{\cdot}s$.

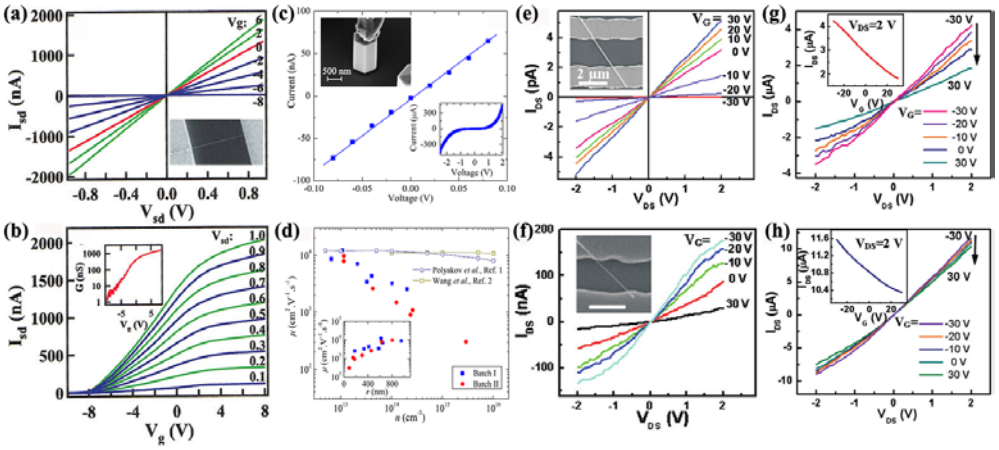

Figure 30 (a)-(b) Gate-dependent I-V_{sd} data of a GaN NW FET with a 17.6 nm diameter, inset showing a SEM image of the FET, and I-V_g data recorded for values of V_{sd} = 0.1-1 V, (inset) Conductance, G, vs gate voltage (b);[274] (c)-(d) representative low-bias I-V charateristics of a single InN NW, inset showing SEM image of the FET and high bias I-V curve (c), and the calculated electron mobility μ as a function of the free carrier concentration n_0, the open symbols were from theoretical calculations based on InN planar structures (see Refs. 275, 276), the inset showing the calculated electron mobility μ as a function of the NW radius r (d);[277] (e)-(h) I_{DS}-V_{DS} curves of the AlN NW FET at different V_G for different samples: (e) D0, (f) D2, (g) D5, and (h) D10, insets of (e) and (f) showing the SEM images of AlN NW-FET, and insets of (g) and (h) displaying I_{DS}-V_G plots of the FETs at V_{DS}=2 V.[278281]

Among III-nitride semiconductors, InN possesses the theoretically predicted highest electron mobility (~12000 $cm^2/V{\cdot}s$), the largest electron saturation velocity (~5×10^7 cm/s) at RT, and narrowest bandgap (~0.65 eV), which rendered itself an excellent candidate for the emerging ultrafast nanoscale electronic and infrared photonic devices. However, due to the extremely high free carrier concentration, large dislocation density, and surface electron accumulation in InN nanostructures, the experimentally reported electron mobility of pure and doped InN NWs was usually in the range of 2 - 2300 $cm^2/V{\cdot}s$,[34, 132, 230, 279-282] which were much lower than the theoretically predicted value. Surprisingly, the highest electron mobility of intrinsic InN NW in the range of 8000 - 12000 $cm^2/V{\cdot}s$ was achieved by Zhao et

al in 2013.[**Error! Bookmark not defined.**] In this work, the electrical transport performance of InN NWs was studied by employing an electrical nanoprobing technique in a SEM environment. As shown in Figure 30(c) and (d), the InN NWs exhibit an ohmic conduction at low bias and a space charge limited (SCL) conduction at high bias. The experimentally calculated electron mobility from the *I-V* curves in the ohmic conduction regime was in the range of 8000 - 12000 $cm^2/V·s$, which reasonably agreed with the theoretical calculation.

The low electron mobility of the wide bandgap AlN and GaN nanostructures limits their applications in high-speed nanoscale optoelectronic devices. Doping offers an effective approach to tune the electron transport performance of III-nitride nanostructures. For example, Tang et al.[278] demonstrated the tunable electrical transport properties of AlN NWs with Mg doping, as shown in Figure 30(e)-(h). For the FET fabrication, Ti(100 nm)/Au(50 nm) were used as source-drain electrodes. The carrier concentration of D0-D10 was in the range of 1.7×10^{18} cm^{-3} to 4.7×10^{19} cm^{-3}, and the corresponding mobility was 2.3×10^{-5} $cm^2/V·s$ to 6.4 $cm^2/V·s$. The carrier concentration and the mobility of Mg-doped AlN NWs were controlled by tuning the flow rate of doping source. Zhao et al.[34] demonstrated *p*-type conduction in InN NWs by doing Mg through MBE technique. The field effect hole mobility based on a single Mg-doped InN NW was in the range of 64-130 $cm^2/V·s$, which was comparable to reported theoretical calculations by the ensemble Monte Carlo method.[283]

Based on the above-discussion, the electron transport properties of group III-nitride nanostructures can be improved by the crystal quality and the doping, as given in Table 9.

Table 9 A brief summary of the electron transport performance of III-nitride nanostructures-based FETs.

Material	Morphology	Growth method	Electrode	Type (n/p)	Electron mobilities ($cm^2/V·s$)	Ref.
Si-doped AlN	Nanoneedle	CVD	Ti(10nm)/ Au(90nm)	*n*	0.1	[25]
Mg-doped AlN	Nanowires	CVD	Ti(100nm)/ Au(50nm)	*p*	1.1-6.4	[278]
GaN	Nanowires	CVD	Ti(20nm)/ Au(50nm)	*n*	2.15	[284]
Mg-doped GaN	Nanowires	CVD	—	*p*	12	[285]
GaN	Nanowires	CVD	Pd/Ti/Pt/A	*n*	30	[286]

			u			
GaN	Nanowires	MOCVD	—	*n*	65	[287]
GaN	NWs	Laser-assisted catalytic growth	Ti/Au	*n*	650	[274]
InN	Nanowires	CVD	Ni(50nm)/ Au(200nm)	*n*	29.2±5.4	[280]
InN	Nanowires	CVD	Ni(40nm)/ Au(87.5nm)	*n*	55-220	[279]
InN	Nanowires	MOCVD	Pt	*n*	2±1	[230]
Si-doped InN	Nanowires	MBE	Ti/Au	*n*	470	[282]
Mg-doped InN	Nanowires	MBE	Ni/Au/ Ni/Au/ Ni/Au	*p*	64-130	[34]
InN	Nanowires	CVD	Ti/Al/Ti/A u	*n*	300-850	[281]
InN	Nanowires	CVD	Ti(20nm)/ Au(200nm)	*n*	2300	[132]
InN	Nanowires	MBE	W/In	*n*	8000-1200 0	[**Error! Bookmark not defined.**]
p-GaN/InGaN/*n* -GaN	Nanorods	MBE	Ni(10nm)/ Au(5nm)	*p*-i-*n*	2000-3000	[288]

4. Application of the III-nitride nanostructures

4.1 Light emitting diodes (LEDs)

Recently, tremendous progress has been made on group III-nitride nanostructure-based LEDs in the full color range from DUV to NIR through tuning bandgap of Al(Ga/In)N nanostructures. Typical types of group III-nitride-nanostructure-based LEDs consisted of nitride *p*-*n* homo- and hetro-junctions, *n*-nitride/*p*-semiconductor, and *n*-semiconductor/*p*-nitride. In this section, the progress made recently on group III-nitride nanostructures LEDs with tunable emission color are described.

4.1.1 Ultraviolet (UV) LEDs

Since the first demonstration of nanostructured GaN LEDs utilizing two single NWs of an Si-doped *n*-GaN NW and a Mg-doped *p*-GaN NW,[274, 285] more attentions were paid to the explorations on tunable light emission sources based on 1D nanostructure embedded with *p*-*n* junction. For example, LEDs based on GaN NRs *p*-*n* junction[289] and *n*-ZnO/*p*-AlGaN heterojunction NWs[290] were explored, as depicted in Figure 31. As for GaN NRs *p*-*n* junction, the *n*-GaN NRs was originated from the N vacancies and/or O impurities, and the *p*-GaN NRs was obtained by Mg doping. The *I*-*V* curve of a single *p*-*n* GaN NR based LED in Figure 31(b) exhibits rectifying behavior. Light emission from the *p*-*n* junction of an individual GaN NR LED is observed by applying a forward bias. The EL spectrum of GaN NR *p*-*n* junction LED exhibits an emission peak at 3.179 eV (~390 nm), which is independent of the current injection as shown in Figure 31(c). As for the single *n*-ZnO/*p*-AlGaN NW based LED device, the turn-on voltage and the rectification ratio, as provided in Figure 31(e), are ~2 V and 4:1, respectively. The rapidly increased EL intensity with increasing current was due to the band-filling effect.[290-292] When the injection currents is ranging from 1 to 4 μA, as described in Figure 31(f), the monopeak is centered at ~394 nm and kept constant, but the EL peak shifts to 400 nm at 5 μA. At low injection currents, the light emission at 394 nm was the radiative recombination of the injected carriers occurred in the *p*-AlGaN side. When the current was high enough, holes could be also injected into *n*-ZnO side, resulting in the near band edge radiative recombination from *n*-type ZnO at ~400 nm.

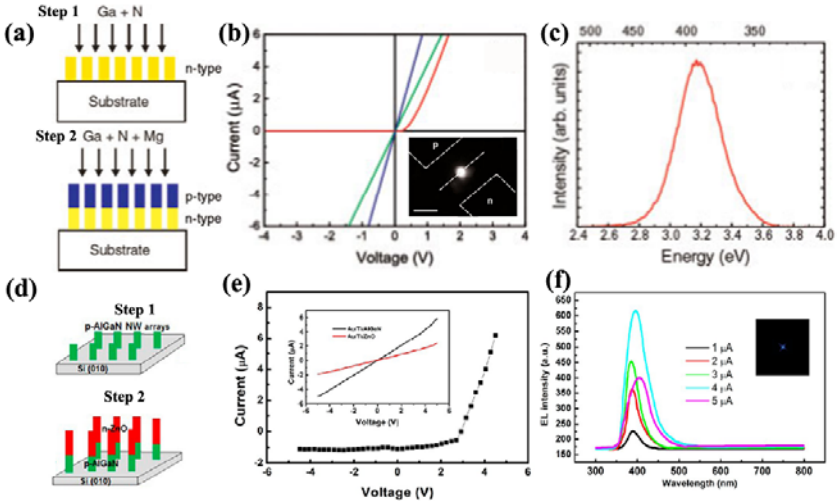

Figure 31 (a) Two-step formation of *n*-GaN/*p*-GaN homojunction NRs; (b) *I*-*V* behavior

of *n*-*n* (blue curve), *p*-*p* (green curve), and *p*-*n* (red curve) junctions, inset showing the luminescence image from a forward-biased NR junction at 3V; (c) the corresponding CL spectrum;[289] (d) two-step CVD growth of *n*-ZnO/*p*-AlGaN heterojunction NWs; (e) *I*-*V* curves of the heterojunction diode (inset: the ohmic contact characteristics of the electrodes); (f) RT EL spectra of single *n*-ZnO/*p*-AlGaN heterojuncton NW under different injection currents, the inset showing a CCD image of device under an injection current of 4 μA.[290]

Multi-well/disk-in-a-wire LED heterostructures were developed to enhance the carrier confinement in the NW active region by Kikuchi et al. in 2004[293] using InGaN/GaN MQD embedded single NW. Afterwards, Carnevale et al. developed DUV LEDs based on $Al_xGa_{1-x}N$ NWs,[294] UV AlGaN NW LED,[295] and ultrathin GaN/AlN MQDs,[296] as illustrated in Figure 32. The DUV LEDs based on $Al_xGa_{1-x}N$ NWs consisted of GaN QWs and $Al_xGa_{1-x}N$ cladding layers with linearly grading composition, forming a polarization-induced *p*-*n* junction without any impurity doping.[294] The current density of the LED was 50 mA/cm^2 at a forward voltage of 10 V, and the EL emission peaked at ~4.3 eV (~288 nm). In 2016, Sarwar et al. reported the DUV emission at ~240 nm from ultrathin GaN/AlN MQDs.[296] The 240 nm emission peak exhibited about an order of magnitude weaker than the 320 nm emission. It was due to the smaller number of 240 nm emitting QDs compared to that of 320 nm in NWs, and the emission from the 240 nm QWs was strongly absorded in the graded AlGaN region before collection. This work provided a pathway toward the realization of efficient DUV emitters using GaN active region with enhanced vertical emission. Zhao et al.[297-298] reported the near-vacuum UV EL emission of AlN NW LEDs. They demonstrated the 210 nm emission AlN NW LED by employing the MBE-grown N-polar AlN NWs and the tunable emission from 210 nm to 300 nm based on Al-rich $Al_xGa_{1-x}N$ NW LEDs.

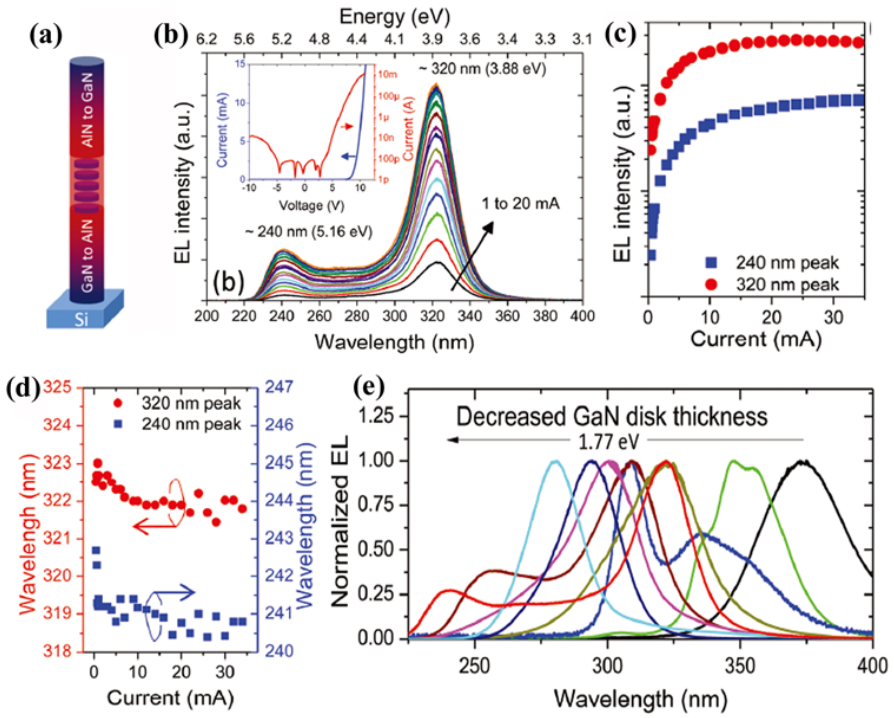

Figure 32(a) Schematic of the double graded polarization doped GaN/AlN NW; (b) EL spectrum of nominally 1 monolayer GaN QD LEDs under dc current injection, the inset showing the *I-V* curve of the LED device; (c)-(d) evolution of 240 nm and 320 nm peak intensities and wavelengths as a function of injection current; (e) normalized EL spectra of polarization doped NW LEDs with decreasing GaN disk thickness.[293]

Mi's group developed nearly defect-free AlGaN tunnel junction (TJ) NW in 2016.[299-300] As shown in Figure 33(a)-(c), the EL emission peak of the AlGaN NW LED with the n^+-GaN/Al/p^+-AlGaN TJ is centered at ~242 nm, showing an enhanced EL emission compared to AlGaN NW-LED without TJ due to the improved electrical performance. The EL intensity was enhanced about 400 times. For unpackaged TJ UV LEDs emitting at 242 nm, a maximum output power of 0.37 mW was measured with a peak external quantum efficiency up to 0.012%.[299] With Al-rich AlGaN shell around the AlGaN NWs with TJ,[300] as described in Figure 33(d)-(f), the core-shell NW heterostructure provided effective carrier confinement in the NW LED active region and suppress nonradiative surface recombination. A relatively narrow emission peak at 275 nm and no significant shift of the peak position with increasing injection current was ascribed to the formation of double heterostructures. The output power of the unpackaged Al TJ DUV LED was higher than 8 mW and a peak EQE was ~0.4%, which were nearly one to two orders of magnitude higher than their AlGaN NW

devices.[299] The improved LED perforemance was proposed to be the significantly enhanced hole transport and injection into the device active region due to the incorporation of Al TJ, the elimination of resistive and absorptive *p*-GaN contact layer.

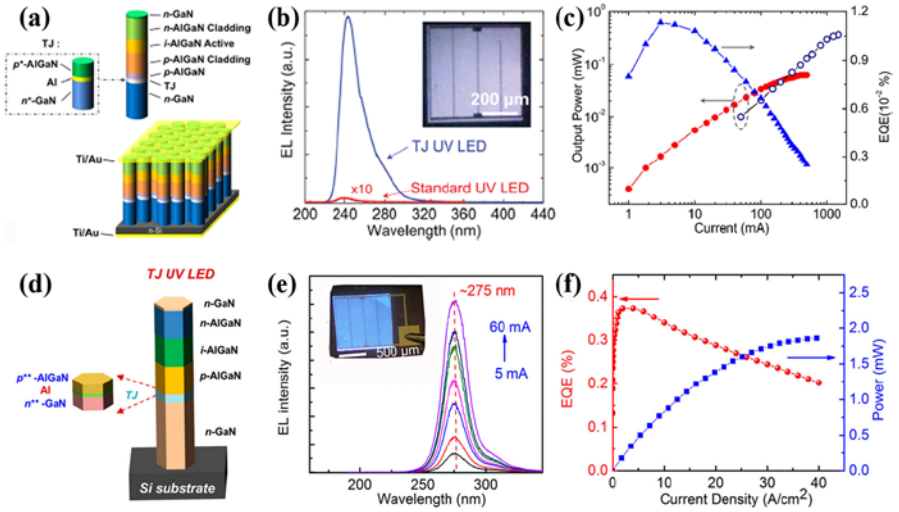

Figure 33 (a)-(c) Schematic of the AlGaN NW TJ UV LED structure (a), RT EL spectra measured from standard and TJ UV LEDs, with the inset showing an optical image of light emission from device top (b), RT output power and EQE of TJ UV LEDs (c);[299] (d)-(f) schematic diagram of Al TJ AlGaN UV LED (d), RT EL spectra of the Al TJ AlGaN UV LED under CW biasing condition, with the inset showing an optical image of the device (e), RT output power and EQE of TJ UV LEDs (f).[300]

Due to the presence of TM polarized light emission of WZ AlN, the light emission propagated in-plane was difficult to be extracted from the top surface. The performance of conventional *c*-plane AlN LED structures was limited by the low light extraction efficiency. [7] In 2015, Zhao et al.[298] demonstrated the dominant light emission from the NW top surface through angle-dependent (0 - 90°) EL measurements. An alternative approach for realizing highly efficient UV emission was ultilized in ternary $Al_xGa_{1-x}N$ NW structures. Wang et al.[242] obtained the ~340 nm UV emission from the $Al_xGa_{1-x}N$ NW based double heterojunction (DH) LEDs. The device showed an internal quantum efficiency (IQE) of ~59% at RT, a relatively small series resistance (~5-100 Ω), highly stable emission characteristics, and the absence of efficiency droop under pulsed biasing conditions up to ~350 A cm^{-2}.

In general, Mg has been widely used as the *p*-type dopant in GaN but possessing significant challenges for AlN due to the exceptionally large ionization energy (~ 600 meV).

Moreover, the presence of free hole concentration in Mg-doped AlGaN is heavily compensated by the formation of extensive native defects and impurity incorporation during the epitaxy of highly lattice mismatched AlGaN epilayers. In order to overcome the intrinsic drawback of low *p*-type conductivity in Al-rich AlGaN for deep ultraviolet (DUV) LEDs, hexagonal boron nitride (h-BN) may be an ideal candidate for DUV LEDs owing to its large bandgap, near-zero polarization field, small ionization energy (~ 150 meV), and especially, the unusual propensity for p-type doping with the presence of B vacancies.[301] For example, Jiang *et al.* demonstrated a novel h-BN/AlGaN *p-n* junction to overcome p-type doping issues in Al-rich AlGaN by using h-BN.[302] Moreover, Laleyan *et al.* reported that h-BN can function as a highly conductive, DUV transparent electrode in the Mg-free NW-array based Al(Ga)N/h-BN LED, and the hole concentration is as high as $\sim 10^{20}$ cm^{-3} at room temperature, which is 10 orders of magnitude higher than that of previously reported Mg-doped AlN epilayers.[303]

4.1.2 Visible LEDs

4.1.2.1 Single color LEDs

Group III-nitride nanostructures possess physical characteristics that are highly promising for various color LED applications since the bandgap of III-nitride nanostructures is widely tunable in the visible light range by alloying the binary material. [304] Both *p*- and *n*-type III-nitride nanostructures can be readily achieved by introducing trace amounts of Mg and Si, respectively, which makes the formation of an epitaxial *p-n* homojunction possible, leading to the efficient radiative recombination between electrons and holes. Therefore, it is potential to achieve various color LEDs based on group III-nitride nanostructures.

In 2004, axial group-III-nitride NW LEDs were reported by Kikuchi et al.[293] and Kim et al.[38]. Whereafter, much attention had been paid to the research of various color and high efficiency LEDs using III-nitride axial nanostructures.[305-307] For example, Ra et al.[305] reported single peak emission of ~415 nm from *p*-GaN/$In_xGa_{1-x}N$/GaN MQW/*n*-GaN NW LED, as shown in Figure 34(a)-(d). The well-controlled In composition in the MQW structure

was optimized by tuning the number of the MQW pairs through MOCVD technique. The output power linearly increased as the current increased due to the uniform and defect-free $In_xGa_{1-x}N$/GaN MQW NW structure.

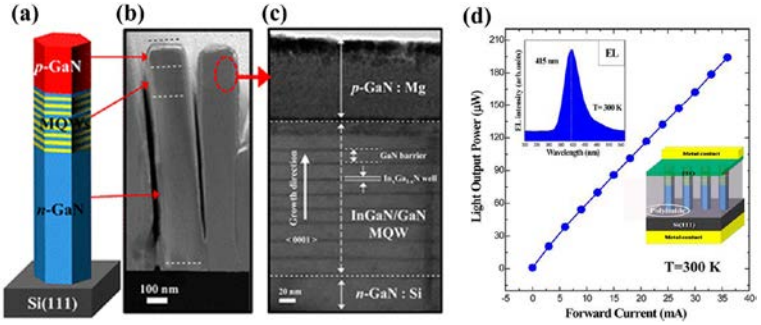

Figure 34(a) Schematic of a single *p*-GaN/$In_xGa_{1-x}N$/GaN MQW/*n*-GaN NW; (b)-(c) low- and high-magnification TEM images of the NW; (d) light output power of NW LED, as a function of current, top-left and bottom-right showing the EL and schematic of the LED structure, respectively.[305]

Later on, Bengoechea-Encabo et al.[307] achieved blue (441 nm), green (502 nm) and yellow (568 nm) LEDs, based on ordered GaN NCs having long InGaN active regions (250 nm to 500 nm). Kishino et al.[306] realized the green-light NC LEDs with emission wavelengths from 515 to 550 nm using RF-MBE grown InGaN NC arrays.

4.1.2.2 Color tunable LEDs

Color tunable LEDs with desired CCT and CRI open up a new pathway to various applications, including displays,[308] smart lighting,[309] and real-time indentification of biological cells.[310] To overcome the drawbacks of the tranditional phorphor LEDs, such as low CRI and Stokes fluorescence loss, phorphor-free and high-efficient tunable-light LEDs were developed. The integration of RGB LEDs directly on a single chip may be an appealing strategy to realize color-tunable LEDs with extremely small size, low power-consumption, and high CRI. To date, much effort has been devoted to exploiting the feasible way to obtain color-tunable III-nitride nanostructure LEDs. The recent studies of the tunable color emission of III-nitride nanostructure LEDs are summed up in the following categories: (i) tuning the In composition in pure InGaN NWs or (Al, In)GaN/GaN 1D MQW/MQD heterostructures;[311- 315] (ii) designing special InGaN/GaN heterostructures and measuring

the device performance under different injection currents/applied voltages/current injection modes;[316-319] (iii) integrating the different areas with tunable color emission directly on a single chip.[243, 320-322] Specifically, one of the simpliest approaches to achieve tunable color emission of III-nitride nanostructure LEDs was to adjust the In composition in InGaN NWs. For example, Qian et al.[323] fabricated a single *n*-GaN/$In_xGa_{1-x}N$/GaN/*p*-AlGaN/*p*-GaN core/multishell (CMS) NW LED, as described in Figure 35(a)-(d). The single NW device was isolated, and discrete contacts were made to the *n*-type core and *p*-type shell. EL emissions at 367, 412, 459, 510, and 577 nm were achieved from $In_xGa_{1-x}N$ NWs with the *x* of 0.01, 0.1, 0.2, 0.25, and 0.35, respectively. Hahn et al.[311] realized the tunable emission based on InGaN NW LEDs, as shown in Figure 35 (e) and (f). The In composition of InGaN NWs grown on *p*-GaN/Al_2O_3 substrates was tuned in the range of 0.06 ~ 0.43 by adjusting the VT of In and Ga sources during the CVD growth. The EL emission peaks were tuned from 435 nm to 575 nm, i.e., from blue to orange colors, with increasing In concentration due to the tuned bandgap of $In_xGa_{1-x}N$ NWs.

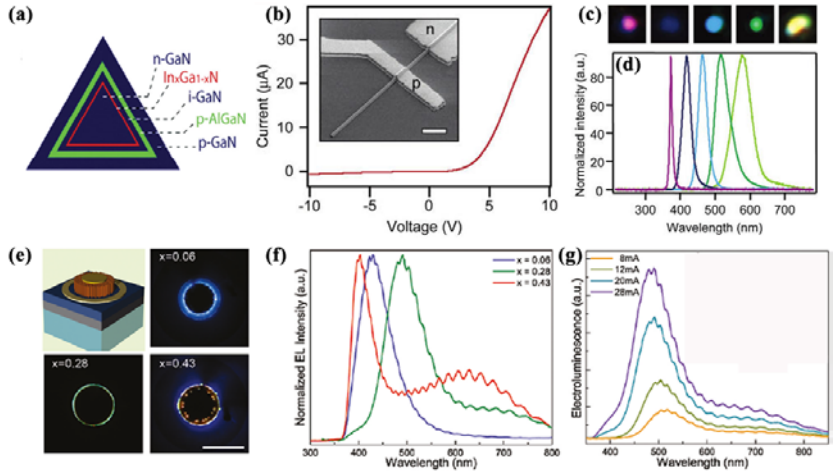

Figure 35 (a) Schemimatic of the *n*-GaN/$In_xGa_{1-x}N$/GaN/*p*-AlGaN/*p*-GaN core/multishell (CMS) NW; (b) I-V data recorded on a CMS NW device, inset showing the corresponding SEM image; (c) OM images collected from around *p*-contact of CMS NW LEDs in forward bias; (d) normalized EL spectra of the LEDs;[323] (e) schematic and OM images of the InGaN NW LED device under forward bias (V = 19, 9, and 11 V for x = 0.06, 0.28, and 0.43, respectively); (f) normalized EL spectra of each device in panel e; (g) dependence of EL on current of *x* = 0.28 device.[311]

Visible-color tunable LEDs using a InGaN thin-film embedded into the

position-controlled GaN NR arrays were reported by Hong et al.[316] During the heteroepitaxial overgrowth of the InGaN/GaN MQW layers, anisotropic MQWs with various QW thickness and composition were formed on different facets of *n*-GaN NRs, as exhibited in Figure 36(a)-(e). The EL spectra of the nanostructured LEDs displayed a continuous peak shifting from red to blue emission with increasing bias voltage. The highly tunable emission color of these NR-embedded thin-film LEDs was originated from both the anisotropic MQW layers formed on the multifaceted GaN NRs and the gradual change in electric field distributions in NR-embedded thin-film structures upon varying electric bias. They also demonstrated the tunable emission color from green to blue based on InGaN/GaN microdonut array LEDs using the similar approach.[319]

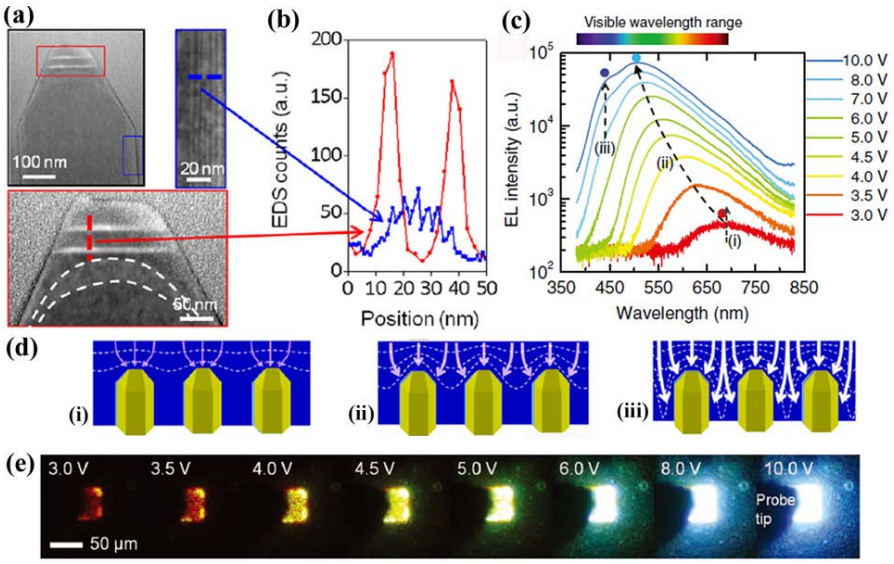

Figure 36(a) STEM images of InGaN/GaN NR MQWs formed on topmost and up right sidewall areas of a GaN NR; (b) the corresponding EDX line profiles of the In along the axial and radial directions of the NR; (c) EL spectra of the nanostructured LEDs taken at various bias voltage from 3.0 to10.0 V; (d) illustrations of the change of equipotential planes (white dotted lines) in the p-GaN overlayer of the nanostructured LEDs and paths of hole carriers (white arrows) (i) under a low electric field near the turn-onvoltage, (ii) with increasing applied voltage, and (iii) at very high bias voltage; (e) light emission photographs of the LEDs taken at various bias voltage.[316]

Since Kishino et al.[324] reported the self-assembled InGaN/GaN NC LEDs with multicolor emission from blue to red, the ideas of micro-semiconductor displays and low-cost

white emitting LEDs with the mixed color of RGB were inspired.[322, 324] In 2014, Wang et al.[320] reported the controllable SAG growth of full-color NW LED arrays on a single Si substrate by PA-MBE, as shown in Figure 37(a)-(c). The NWs consisted of one ~0.4 μm GaN:Si segment, ten vertically aligned InGaN/GaN dots, one ~10 nm *p*-doped AlGaN electron blocking layer (EBL), and one ~0.2 μm GaN:Mg segment. The emission color was tuned from blue (450 nm) to red (700 nm) by adjusting size and/or compositions of the QD active region. These integrated tunable full-color LED arrays exhibited a wide range of CCT (~1900 - 6500 K) and high color rendering index (＞90). The tunable emission from 430 nm to 630 nm was also realized on AlInGaN quaternary core-shell NW heterostructures.[315] The heterostructure NW LEDs exhibited an output power exceeding 30 mW for a ~1×1 mm^2 nonpackaged device at a current density of 100 mA/cm^2 due to the suppression of nonradiative surface recombination of such core-shell heterostructure.

In 2016, Ra et al.[321] reported the full-color single NW LEDs by incorporating multiple InGaN/GaN QDs in *p*-GaN:Mg/*n*-GaN:Ge NWs, as shown in Figure 37(d)-(g). The EL emission was dependent on the diameter of single NW LED subpixels with a small level of quantum-confined Stark-effect. Under the same injection current density, the NWs with larger diameters obtained stronger light intensity due to the larger active region area. On the other hand, NW LED subpixels with smaller diameters could withstand higher current density due to the more efficient current conduction and heat dissipation.

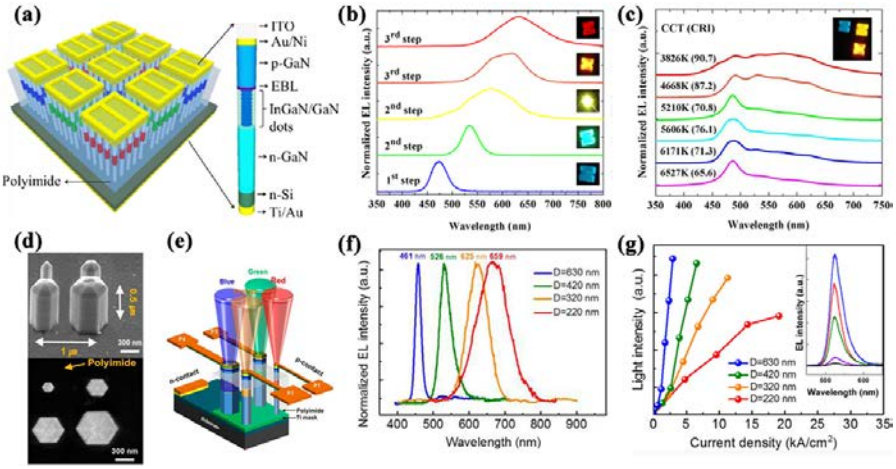

Figure 37(a) Schematic of multi-color NW LED devices on the same chip; (b) normalized EL spectra of NW LED subpixels monolithically integrated on Si substrate and the corresponding optical images; (c) normalized EL spectra and their corresponding CCT/CRI values of a

representative triple-color LED pixel measured under different injection current.[320](d) side- and top-view SEM images of the InGaN/GaN dot-in-NWs with different diameters; (e) schematic illustration of monolithically integrated multicolor single NW LED pixels on a single chip; (f) EL spectra of single NW LEDs with different diameters; (g) the corresponding light-current characteristics of the LED devices and EL spectra of the green-emitting LED device under different injection currents.[321]

4.1.2.3 White light LEDs

Efficient light emission covering nearly the entire visible light range has been realized with the utilization of InGaN nanostructures.[325-326] Generally, there are two types of heterostructures adopted in the fabrication of phosphor-free white light LEDs, such as core-shell heterostructures[327 - 328] and quantum dots/nanodisks in 1D GaN nanostructures.[325-326, 329- 337] For example, Nguyen et al.[328] reported a type of axial NW LED heterostructures, with the use of self-organized core-shell InGaN/AlGaN dot in *p*-GaN:Mg/*n*-GaN:Si NW arrays, as shown in Figure 38(a)-(c). The energy band diagram of the InGaN/AlGaN dot-in-a-wire core-shell LED active region showed superior 3D carrier confinement due to the multiple AlGaN shell and barrier layers. The ten InGaN dots were centrally confined and capped by the AlGaN barriers, each of which formed an Al-rich shell at the NW sidewall. The output EL spectra of the dot-in-a-wire core-shell LED under various injection currents were highly stable and nearly independent of injection currents. The LED exhibited nearly neutral white light emission with CCT of ~4450 K and a very large CRI of 95.

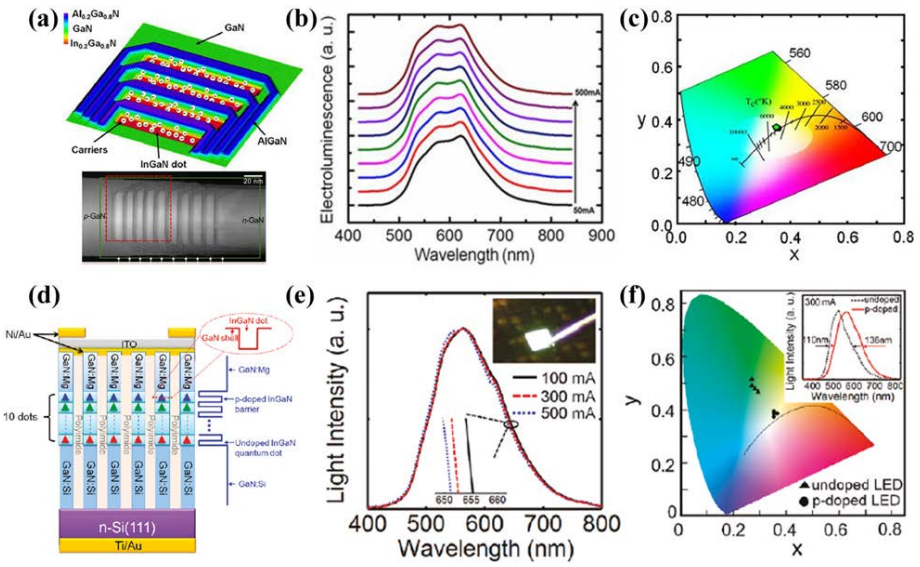

Figure 38(a) Schematic illustration of the energy band diagram of the InGaN/AlGaN dot-in-a-wire core-shell LED active region and the corresponding STEM-HAADF images; (b) EL spectra of the LED measured under different injection currents ; (c) CIE diagram showing the stable white light emission for injection current from 50 mA to 500 mA;[328] (d) illustration of the *p*-doped InGaN/GaN dot-in-a-wire LED device; (e) RT EL spectra of a dot-in-a-wire LED, inset showing the white light emission image; (f) 1931 CIE chromaticity diagrams, the emission spectra measured at an injection current of 300 mA for the undoped and *p*-doped LEDs were shown in the inset.[329]

The InGaN quantum dots/nanodisks embeded in 1D defect-free GaN nanostructures is an effective strategy to achieve phosphor-free white light LEDs. Nguyen et al.[329] reported the white light emission of InGaN/GaN dots in a *p*-GaN:Mg/*n*-GaN:Si NW LEDs, as described in Figure 38(d)-(f). The NW LED showed strong white light emission. Moreover, for the *p*-doped LED, the CIE chromaticity coordinates with increasing injection current were nearly unaltered. By comparing the RT IQE of the undoped and *p*-doped LEDs, the IQE of *p*-doping (~56.8 %) was 50% higher than that of undoping (~36.7%), which was enough efficient for the phosphor-free white LEDs.

Therefore, group III-nitride nanostructures offer an alternative approach to develop the white-light LEDs with improved efficiency, increased lifetime, and enhanced light quality.

4.1.3 Near infrared LEDs

Kishino et al.[338] explored the InGaN NC NIR LED with a light emission wavelength of ~1.46 μm, benefiting from the SAG grown InGaN NCs with the diameter of ~300 nm and the In concentration of 0.85. Since then, much effort have been devoted to the study of III-nitride nanostructures NIR LEDs.[339- 342] Le et al.[339] demonstrated the EL emission at ~0.71 eV (1746 nm) from a single InN *p-i-n* NW LED. Zhao et al.[342] reported the comparative study of InGaN/GaN NW NIR LEDs epitaxially grown on Mo and Si substrates, as shown in Figure 39(a)-(g). The low injection current density and high EQE of droop-free InGaN/GaN quantum-disks-in-nanowire LEDs emitting were ascribed to the effect of disparat current spreading and high-effective heat dissipation. The radiative recombination rates of NW-LEDs between RT and 40 °C was found not limited by Shockley-Read-Hall recombination, Auger recombination, or carrier leakage mechanisms, thus realizing droop-free operation. The output power and wall-plug efficiencies of LED on Mo were stronger than those on Si because the heat generated, even at high current injection, could be dissipated efficiently without degrading device performance due to the high thermal conductivity of LEDs on Mo.

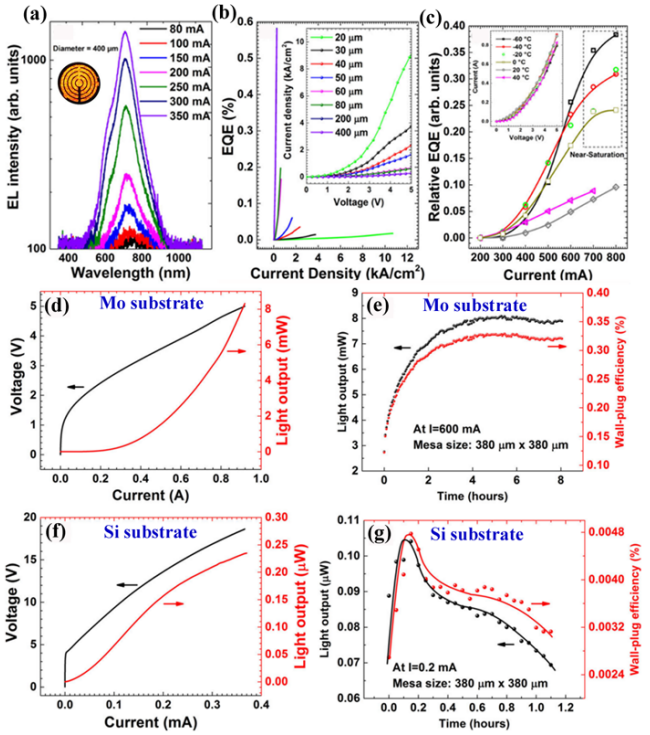

Figure 39 (a) The EL spectra of the InGaN/GaN NW LED grown on Mo substrate, inset

showing the optical microscope image of the LED; (b) the EQE of LEDs with different sizes; the inset showing the measured *I-V* characteristics; (c) EQE with current injection between -60 and 40 °C; the inset showing the *I-V* characteristics of LEDs between -60 and 40 °C. The dashed rectangle indicates the region where the relative EQE reached near-saturation; (d) typical *L-I-V* of LEDs on Mo; (e) light output power and wall-plug efficiency of LEDs on Mo versus time. A constant current of 600 mA was applied to the LEDs with size of 380 μm × 380 μm; (f) typical *L-I-V* of LEDs on Si; (g) light output power and wall-plug efficiency of LEDs on Si versus time. A constant current of 0.2 mA was applied to the LEDs with size of 380 μm × 380 μm.[342]

4.1.4 Micro-LEDs

Besides the above-mentioned NW-array or single-NW based LEDs, micro-LEDs (μ-LED), as small as a micro-size of ~10-30 μm, is presently recognized as the ultimate display technology because they inherently provide high brightness, high contrast ratio, high response speed, long lifetime, and power saving properties, which can be operated over a wide temperature range. Since the report of the first current injection μ-LED (~12 μm) based on p-GaN/InGaN/n-GaN QWs,[343] much more attentions have being paid on the development of μ-LED, exhibiting promising products in wearable displays for high speed three-dimensional/augmented reality/virtual reality (3D/AR/VR) display applications, high brightness/contrast large flat panel displays and TVs, and light sources for the neural interface and optogenetics, and for visible light communications (Li-Fi).[344] For example, Kishino *et al.* reported the multicolor (red, green, blue, and yellow; RGBY) μ-LED pixels with 5 × 5 μm^2 emission windows by using InGaN/GaN-based nanocolumns (NC).[345]

4.2 Photodetectors

Because of the tunable direct bandgap energies of III-nitride materials, their 1D nanostructures are the promising candidates for photodetecors operating in a broad spectrum range from DUV to NIR.

4.2.1 PDs based on undoped III-nitride nanostructures

In the past few years, the photoconductivity performance of III-nitride nanostructures, especially GaN NWs, have been intensively investigated.[230, 346- 352] In 2005, Calarco et al.[346] reported the electrical transport performance of single GaN nanowisker under the dark and illumination. The photocurrent of the GaN NW PD device depended on the diameter of the NWs due to the existence of depletion space charge layers. The recombination process was enhanced within the NWs with small diameters, which screened the depletion electric field, leading to the decreased photocurrent. However, the photocurrent had a negligible dependence on the diameter, since the large bulk volume remained undepleted. Wang et al.[350] demonstrated single NW PD based on axial GaN NWs on pattern Si substrate. The device exhibited a high responsivity up to 10000 A/W with a response time less than 26 ms.

Although the photoconductivity of AlN nanostructures under DUV illumination was rarely investigated due to its wide bandgap and high insulating nature, the performance of single AlN NWs using different subband gap excitation sources was reported by Huang et al.[348] In this study, the photoconductivity of individual AlN NW was characterized under air and vacuum by employing various subband gap excitation sources of 1.53 eV (808 nm), 2.33 eV (532 nm), 3.06 eV (405 nm), and 3.81 eV (325 nm), as illustrated in Figure 40(a)-(e). Both positive (under 1.53 and 2.33 eV excitations) and negative (under 3.06 and 3.81 eV excitations) photocurrent responses were observed. Based on the energy band and photoconduction process near surface region of the AlN NW, negative photoconductivity could be generated originating from the existence of electron trap and recombination center in AlN. Notably, a strong positive surface photoconductivity could be generated by manipulating the measurement environment from air to vacuum because of the excess electrons produced by the surface electron trapping states [$O^-(g) + h\nu \rightarrow e^- + O_2$ (ad)], inducing an oxygen molecular sensitization effect, which was responsible for the surface sensitive positive photoconductivity.

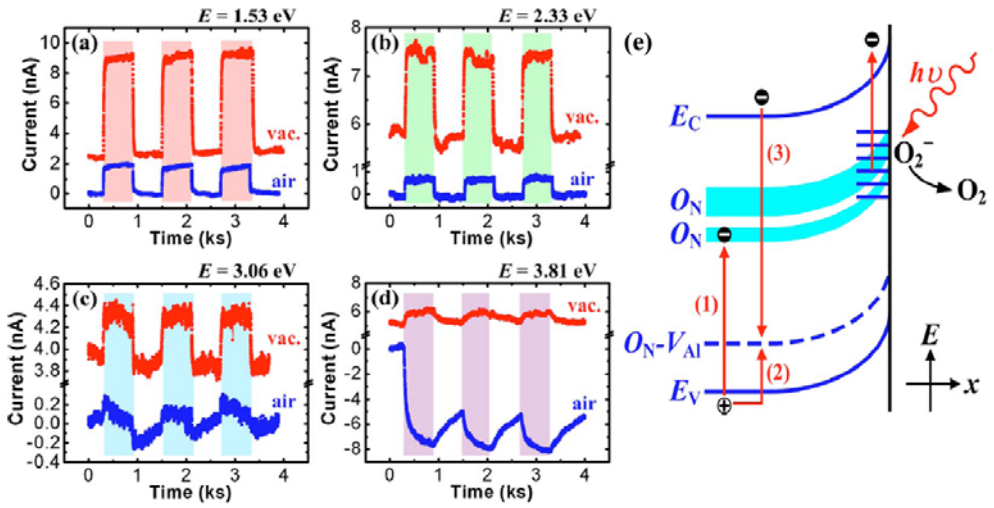

Figure 40(a)-(d) The current response curve of the single AlN NW in the air and vacuum under repeated excitation using different photon energy (*E*) of (a) 1.53 eV, (b) 2.33 eV, (c) 3.06 eV, and (d) 3.81 eV; (e) The schematic drawings of the energy band and photoconduction process near surface region of an AlN NW.[348]

The vacuum-ultraviolet (VUV) PDs with high sensitivity can be significantly ultilized for coping space weather and monitoring hazardous. AlN is an ideal material for VUV detection due to the wide bandgap (~6.2 eV), superior radiation resistance, high thermal and chemical stability. In 2015, Zheng et al.[353] demonstrated the high sensitivity of AlN micro/nanowire-based PD under VUV illumination (193 nm), as illustrated in Figure 41(a)-(c). The magnitude of photocurrent obtained under 193 nm light was five orders higher than that of the dark current. The photocurrent curve was linearly increasing with rising bias voltage. The photocurrent responded expeditiously in 0.1 s and increased to a stable value of ~24 nA when the illumination was turned on, while it decreased dramatically to the initial value in 0.2 s when the light was turned off, indicating the fast response speed of the AlN micro/nanowire-based PD.

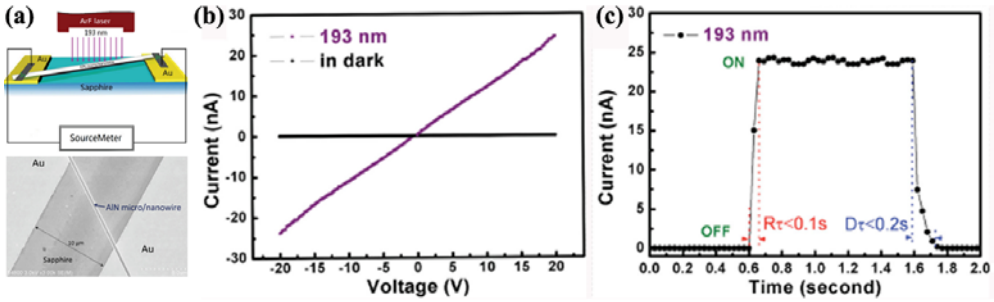

Figure 41(a) Schematic and representative SEM image of AlN micro/nanowire-based PD; (b)

I-V characteristics of the PD illuminated under a light of 193 nm and under dark condition; (c) time-dependent response of the device measured under air environment at RT applied a bias of 20 V.[353]

In addition to the nitride NW PDs operating in the spectral range from UV to visible light, the photoconductivity (PC) of individual infrared-absorbing InN NW was reported by Chen et al.[230] Under 808 nm excitation, the photocurrent values of a single InN NW device at the bias of 0.1 V exhibited a gradual increase as the decrease of temperature from 300 K to 10 K, while the photosensitivity (S) increased one order of magnitude from 0.3 to 14, indicating the good device performance for IR sensing. The photoconductive gain could reach to the value of 8×10^7 at RT in vacuum.

4.2.2 PDs based on doped III-nitride nanostructures

The incorporation of dopants in group III-nitride nanostructures has been demonstrated as an effective strategy to achieve desired optical and electronic properties.[15] This approach was also applicable to optimize the performance of group III-nitride nanostructures PDs.[354-356] For example, Richter er al.[354] investigated the influence of *n*-doping on the electrical transport performance of GaN NWs with different diameters. The photocurrent of GaN NWs with highly doped Si was significantly higher than that of NW with undoped and lightly doped Si under UV illumination. Patsha et al.[355] reported photoconductivity performance of Mg doped nonpolar GaN NWs. The fabricated devices exhibited a very high on-off ratio of ~100 under the illumination of 470, 530, and 788 nm wavelengths.

4.2.3 PDs based on III-nitride homo/heterostructures

PDs consisting of an active *p-n* junction based on III-nitride nanostructures have been developed. When light falls on the junction, a reverse current flying proportional to the illumination can be detected. Rigutti et al.[357] reported the UV PDs based on GaN/AlN quantum disks in a single GaN NW. The device showed a drastically reduced dark current and an enhanced photocurrent. The responsivity was ~2000 A/W at λ=300 nm, and the photosensitivity was up to 500 at RT. Bugallo et al.[358] reported the fabrication and

characterization of a visible-blind PD based on *p-i-n* junction GaN NW array, as shown in Figure 42(a)-(c). The responsivity of the PD was ~0.47 AW^{-1} at -1 V, under UV illumination at λ=356 nm with an incident power of 1.6 μW. Moreover, the photocurrent appeared at □ 3.27 eV and increased by more than two orders of magnitude between 3.3 and 3.4 eV, the rejection ratio of UV to visible photocurrent was ~200. Such visible-band detectors had the promising applications in high-speed PDs. Subsequently, high sensitivity of a single GaN NW PD based on the radical $In_{0.16}Ga_{0.84}N$/GaN MQW *n-i-n* junctions was reported by Bugallo et al..[359] The PD had a light response to ~477 nm, and the responsivity was as high as 8000A/W. Later on, Gonzalez-Posada et al.[360] demonstrated the photocurrent performance of a single axial GaN *n-i-n* NW grown by PAMBE. The photoconductive gain of the device was in the range of 10^5 to 10^8, and the responsivity ratio of UV (350 nm) to visible (450 nm) was higher than 10^6. Recently, Lähnemann et al.[361] reported the UV photosensing performance of a single GaN NW incorporating AlN/GaN: Ge axial heterostructures. They found both the incorporation of the heterostructures and the larger number of active nanodisks and AlN barriers could result in the decrease of the dark current and the increase of the photosensitivity.

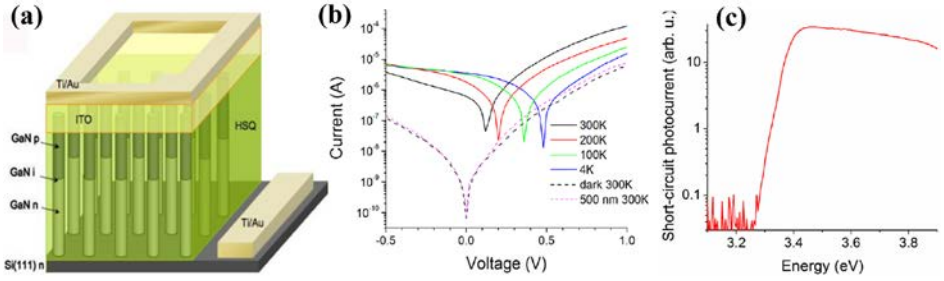

Figure 42(a) Schematic representation of *p-i-n* GaN NWs photodetector; (b) *I-V* characteristics under UV illumination at 300, 200, 100 and 4 K. Dashed lines showed the dark *I-V* and the *I-V* under illumination with λ = 500 nm light at RT; (c) RT photocurrent spectrum under zero applied bias.[349]

In addition, efforts have been devoted to improving the photoconductive performance of III-nitride nanostructure-based PDs by using different electrode materials.[362-364] Babichev et al.[364] reported the fabrication and photoconductive properties of the PDs using few-layer graphene contact to GaN NW ensemble. The device showed a responsivity of ~25 A/W at 357 nm under 1 V biasing, and had a strong response up to 298 nm.

4.3 Lasers

Since the first demonstration of NW lasers in 2001,[365] III-nitride NW lasers have attracted tremendous attention due to their tunable bandgaps (from 0.65 eV for InN to 6.2 eV for AlN), extremely small surface recombination velocity, and large exciton binding energy (~26 meV for GaN and ~60 meV for AlN). Therefore, 1D III-nitride nanostructures have potential applications with ultralow threshold, small scale lasers from DUV to NIR spetra range. Moreover, lasers with low dimensionality provide the opportunity to develop efficient, low-threshold, and compact light sources for diverse novel applications in high-speed communications, information processing, and optical interconnects. In this section, the development of optically pumped and electrically injected III-nitride nanostructure lasers with emission wavelength ranging from DUV to red light range are described.

4.3.1 Optically pumped NW lasers

A variety of optical resonators based on III-nitride nanostructures have been designed. In order to realize III-nitride semiconductor nanolasers with single mode, broadband-tunable emission wavelengths, and ultralow lasing threshold, many different types of micro/nanocavities have been developed, including Fabry-Pérot, microstadium, photonic-crystals, ring cavities, two-dimensional distributed feedback (2-D DFB), and random lasing. Some experimental details of III-nitride NW lasers are listed in Table 10. In general, the lasing threshold is dependent on the NW dimensions, quality of the NWs, characteristics of NW cavities, and coupling with the substrate.

Table 10 A brief summary of the experimental detais of III-nitride NW lasers.

Active layer	substrate	Operating temperature	Threshold	λ (nm)	Resonator type	Ref.
GaN	*c*-sapphire	RT	700 nJ/cm^2	370 to 380	Fabry-Pérot	[151]
GaN	*c*-sapphire	RT	2-3 μJ/cm^2	384	Fabry-Pérot	[366]
GaN	*c*-sapphire	RT	22 kW/cm^2	370 to 378	Fabry-Pérot	[367]
GaN	*c*-sapphire	RT	112.5 μJ/cm^2	373 to 380	Ring	[368]
InN	Si(100)	20 K	70 kW/cm^2	1559 to 1644	Fabry-Pérot	[226]
GaN	*c*-sapphire	RT	1536 kW/cm^2	370 to 372	Microstadium	[369]
InGaN/GaN	*r*-sapphire	RT	900 kW/cm^2	383 to 478	Fabry-Pérot	[370]
InGaN/GaN	GaN/	RT	320 kW/cm^2	470	2-D DFB	[371]

	c-sapphire					
AlInGaN	AlGaN/ *c*-sapphire	RT	0.52 MW/cm^2	343.7	Fabry-Pérot	[372]
GaN	Si	RT	320-350 kW/cm^2	362 to 370	Random	[373]
InGaN/GaN	GaN/ *c*-sapphire	RT	0.42 MW/cm^2	440 to 560	2-D DFB	[374]
GaN	Si	RT	120 kW/cm^2	370	Photonic crystal	[375]
InGaN/GaN	Si	7 K	300 kW/cm^2	533	Plasmonic	[376]
GaN	Si	RT	95.2 nJ/cm^2	366 to 372	Polariton	[377]
GaN	Au/SiO_2/Si	RT	241 kW/cm^2	370	Fabry-Pérot	[378]
InGaN/GaN	Si	78 K	3.7 kW/cm^2	510 to 522	Plasmonic	[379]
GaN	*c*-sapphire	RT	231 kW/cm^2	367 to 371	Fabry-Pérot	[380]
GaN	*c*-sapphire	RT	874 kW/cm^2	370 to 374	Fabry-Pérot	[381]
GaN	GaN/ *c*-sapphire	RT	5 MW/cm^2	455 to 470	Random	[382]
GaN	*c*-sapphire	RT	—	362 to 375	Fabry-Pérot	[383]
InGaN/GaN	*c*-sapphire	RT	130 kW/cm^2	380 to 440	Photonic crystal	[384]
GaN	Si	RT	625 nJ/cm^2	370	Polariton	[385]
GaN	SiO_2/Al film	RT	3.5 MW/cm^2	370	Polariton	[386]
InGaN/GaN	Al_2O_3/Ag film	7 K	10-100 W/cm^2	474 to 627	Plasmonic	[387]
InGaN/GaN	Patterned Si	RT	500 KW/cm^2	423	Fabry-Pérot	[388]
GaN	*c*-sapphire	RT	1055 KW/cm^2	368	Fabry-Pérot	[389]
InGaN/GaN	*c*-sapphire	RT	6.5 mJ/cm^2	421.5 to 422.4	WGM	[390]
GaN	GaN/ *c*-sapphire	RT	410 KW/cm^2	372	Fabry-Pérot	[391]
GaN	GaN/ *c*-sapphire	RT	440 KW/cm^2	364.7	Polariton	[392]
InGaN	GaN/ *c*-sapphire	RT	~0.65 MW/cm^2	429 to 525	2-D DFB	[393]

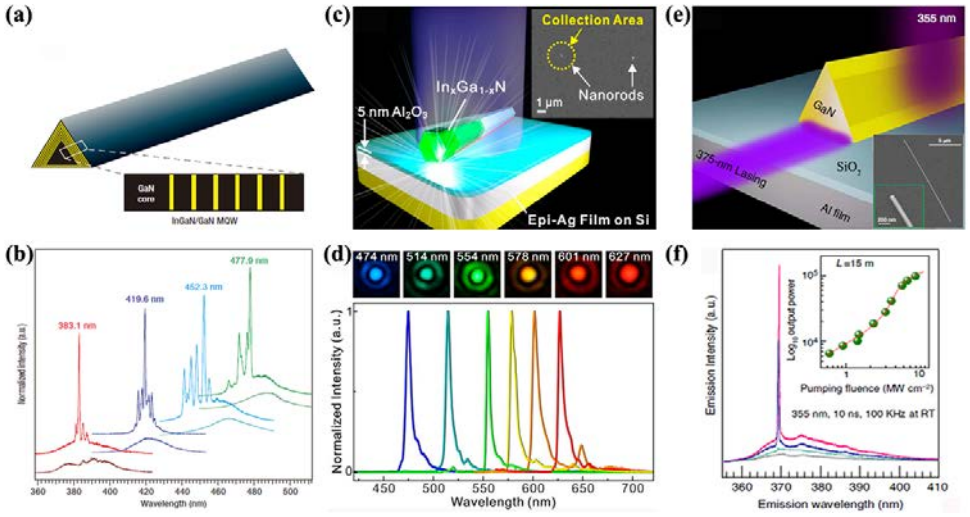

Figure 43(a)-(b) Schematic of an InGaN/GaN MQW NW and corresponding cross-sectional view of a NW facet highlighting the MQW structure (a), and nomalized PL spectra of four respresentative 26 MQW NW structures with the increase of In composition pumped 250 and 700 kW/cm^2, respectively (b);[370] (c)-(d) schematic of the nanolaser structure based on a single InGaN/GaN NR and the SEM image on the upper right supplied a collection area of ~3 μm in diameter using a focused excitation laser beam (c), tunable color single-mode lasing images obtained from single NR (d);[387] (e)-(f) schematic of the nanolaser device based on a GaN NW with a triangular cross-section and inset showing the SEM image of a GaN NW on SiO_2/Al film (e), and power-dependent PL emission spectra, inset exhibited the relationship of integrated PL emission and the pumping intensity (f).[386]

In 2002, Johnson et al.[151] reported the optically pumped RT laser emission (~375 nm) from a single GaN NW. The localization of bright emission at the two ends of the NW suggested strong waveguiding behavior, and the cavity modes were Fabry-Pérot (axial) rather than WGMs. Since then, much attention was paid to decrease the optically pumped lasing threshold of GaN NWs laser with Fabry-Pérot cavity. Gradečak et al.[367] demonstrated a low lasing threshold density of 22 kW/cm^2 of optically pumped lasing in MOCVD GaN NWs with a nonpolar <11-20> growth direction. These NWs functioned as free-standing Fabry-Pérot cavities with triangular cross-sections, dislocation-free structures, uniform diameters, and *n*-type doping. Later on, Qian et al.[370] realized the multi-mode tunable nanolasers from InGaN/GaN MQW core/shell NWs, as shown in Figure 43(a) and (b). The heterostructure consisted of single crystalline GaN NW cores and InGaN/GaN MQW shells.

The GaN cores acted as the optical cavity, and the MQW shells served as a composition-tunable gain medium. Such heterostructure contained 3 to 26 QWs, and the diameters and lengths of the NWs were 200-400 nm and 20-60 μm, respectively. Tunable lasing was achieved ranging from 383 nm to 478 nm by increasing the In contents.

Compared to the most reported GaN NW lasers with multi-mode operation, the development of NW lasers with single-mode operation is critical for realizing the pratical applications in constructing nanoscale photonic devices and optoelectronic circuits.[394] Till to now, much progress has been made on single-mode operation based on GaN NWs.[378, 380-381, 383-384, 395] Li et al.[380] demonstrated the RT single-mode linewidth of ~0.12 nm and >18 dB side-mode suppression ratio GaN NW lasers operating far above lasing threshold, where the GaN NWs were obtained by a top-down approach from *c*-plane GaN epilayers on sapphire. Each laser consisted of a linear, double-facet GaN NW functioned as gain medium and optical resonator. Xu et al.[381] reported that the side-by-side contacted GaN NW-pair showed a single-mode laser at 370 nm with a threshold of 874 kW/cm^2. The coupled NW-pair provided a mode selection mechanism through the Vernier effect. Later on, mode-slection by coupling a GaN NW laser to an underlying gold substrate was demonstrated by Xu et al.[378] The single mode behavior was converted from multimode lasing of GaN NWs following placement onto a gold film. The single-mode GaN NW laser also obtained by controlling the gap sizes of cleaved-coupled cavities in GaN NWs[383] and externally coupling GaN NWs to a dielectric grating.[395]

In addition, broadband-tunable III-nitride semiconductor nanolasers with ultralow lasing threshold offer the promising applications in all-optical, on-chip information processing, miniaturized smart display technology, and super-resolution biomedical imaging. In this regard, Lu et al.[387] realized tunable color plasmonic lasers in full visible spectrum based on MOS (Ag/Al_2O_3/InGaN) structure. InGaN/GaN NWs consisted of a GaN bottom section and a top InGaN section with a spontaneously formed InGaN shell, as shown in Figure 43(c) and (d). The lasing color could be tuned from blue (474 nm) to red (627 nm) under optical pumping through a novel autotuning mechanism, which was resulted from the interplay between the dispersions of the plasmonic resonator material and the gain medium in a gain-medium-loaded plasmonic nanoresonator. Meanwhile, UV nanolasers (200 - 400 nm)

were attracted tremendous attention on the basis of the important applications from laser therapy to optical storage. Usually, the emission wavelength in the UV spectral region could be obtained by plasmonic lasers. However, some obstacles, including high ohmic, radiation losses, and bending-back effect,[396] hindered the realization of UV plasmonic lasers. Zhang et al.[386] reported the RT UV plasmonic nanolaser of GaN NW with a triangular cross-section as illustrated in Figure 43(e) and (f). Under pumping source of ~355 nm, a sharp peak with ~0.8 nm linewidth was observed as the increase of pumping intensity. The *S*-shaped light output intensity *vs.* the pumping intensity supplied a direct evidence of lasing, and the lasing threshold was ~3.5 MW/cm^2.

Moreover, the laser wavelength based on III-nitride NWs can be tuned by manipulating the dielectric constant in a photonic crystal structure.[374, 384] Wright et al.[384] demonstrated the single-mode InGaN/GaN NW photonic crystal lasers by utilizing the broad gain-bandwidth of InGaN/GaN MQW heterostructures through the top-down approach. By employing two different gain sections, InGaN MQWs with an emission peak of ~430 nm and InGaN under-layer with 385 nm emission wavelength, the obtained single-mode lasing could be tuned in the blue-violet spectral range from 380 to 440 nm.

4.3.2 Electrically injected NW lasers

Electrically injected semiconductor NW lasers can be widely utilized in applications ranging from telecommunications and information storage to medical diagnostics and therapeutics.[397] In the past several years, much attention was paid to develop electrically injected low threshold III-nitride NW lasers at RT under continuous wave biasing conditions, due to the high threshold current densities (up to kA/cm^2) of conventional planar GaN-based laser devices.

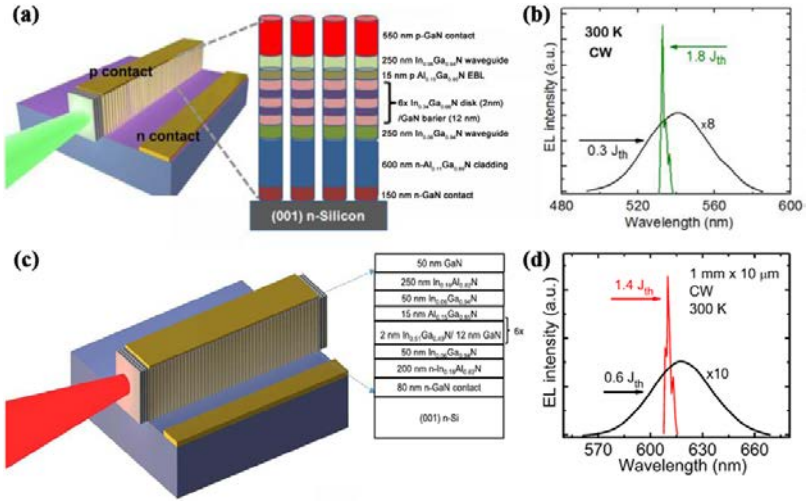

Figure 44(a)-(b) Schematic of the green NW laser heterostructure and the EL spectra under cw bias above and below threshold;[398] (c)-(d) schematic representation of the red NW laser heterostructure and EL spectra under cw bias above and below threshold.[399]

Recently, the electrically injected lasers of 3D III-nitride quantum-confined NW heterostructures were realized in the spectral range from red,[399] green[398] to UV-A,[400] UV-B,[401] and UV-C[402] through designing the heterostructures, tuning the compositions, and optimizing the NW diameter and fill factors. Bhattacharya's group demonstrated the electrically pumped green and red edge-emitting lasers from the InGaN/GaN disk-in-NW heterostructure on Si (001) substrates,[398-399] as illustrated in Figure 44. The gain medium of the green and red laser heterostructures consisted of 6 $In_xGa_{1-x}N$ disks (2 nm) separated by 12 nm GaN barriers inserted in the center of the waveguide layer. The optimized area density of NW arrays for both laser structures was 2×10^{10} cm^{-2}. The laser color was tuned by increasing the In fraction in the $In_xGa_{1-x}N$ disks in the active region from 0.34 to 0.51. The linewidths of the green (λ = 533 nm) and red (λ = 610 nm) laser peaks were ~0.8 nm and ~0.9 nm, respectively, and the threshold current densities of green and red laser were 1.76 kA/cm^2 and 2.9 kA/cm^2, respectively.

Theoretically, the electrically pumped laser of AlGaN-based lasing structure can span from UV-A (320 - 420 nm), UV-B (280 - 320 nm), to UV-C (100 - 280 nm) according to the tunable direct bandgap of AlGaN from 3.4 eV to 6.2 eV. However, due to the wide bandgap and large effective mass of AlGaN materials, it is still challenging to achieve electrically injected UV or DUV lasers, which usually required carrier densities on the order of 10^{19} cm^{-3} to meet transparency conditions. Low-dimensional quantum-confined nanostrucures with low

defects and dislocations and efficient *p*-type conduction can effectively reduce the carrier density and the laser threshold. In this regard, tunable-color electrically injected lasers in the spectra range from UV-A to UV-C were fabricated by utilizing AlGaN NWs, as illustrated in Figure 45.[400-402] Li et al.[400] reported the electrically pumped AlGaN core-shell NW lasers in the UV-A (~315-340 nm) range. The NW consisted of AlGaN *p*-*i*-*n* layer, *n*- and *p*-GaN contact layers, and AlGaN shell. By adjusting current densities at 6 K, two discrete lasing peaks located at ~332.7 nm and 334.1 nm were observed, and the lasing threshold current density was estimated to be ~12 A/cm^2, as provided in Figure 45(a)-(c). Zhao et al. reported the electrically injected UV-B (~289 nm)[401] and UV-C (~262.1 nm)[402] lasers of the similar AlGaN NW heterostructures by adjusting Al content as shown in Figure 45(d)-(i). Under different injected currents, the lasing peaks centered at ~289 nm and ~262.1 nm were obtained, and the lasing threshold current was ~300 A/cm^2 at RT and 200 A/cm^2 at 77 K, respectively. All of the UV A-C lasers by employing AlGaN NW heterostructures showed a low threshold current because of the nearly defect-free AlGaN NWs, the existence of QD-like nanostructures, and the high-Q optical cavity.

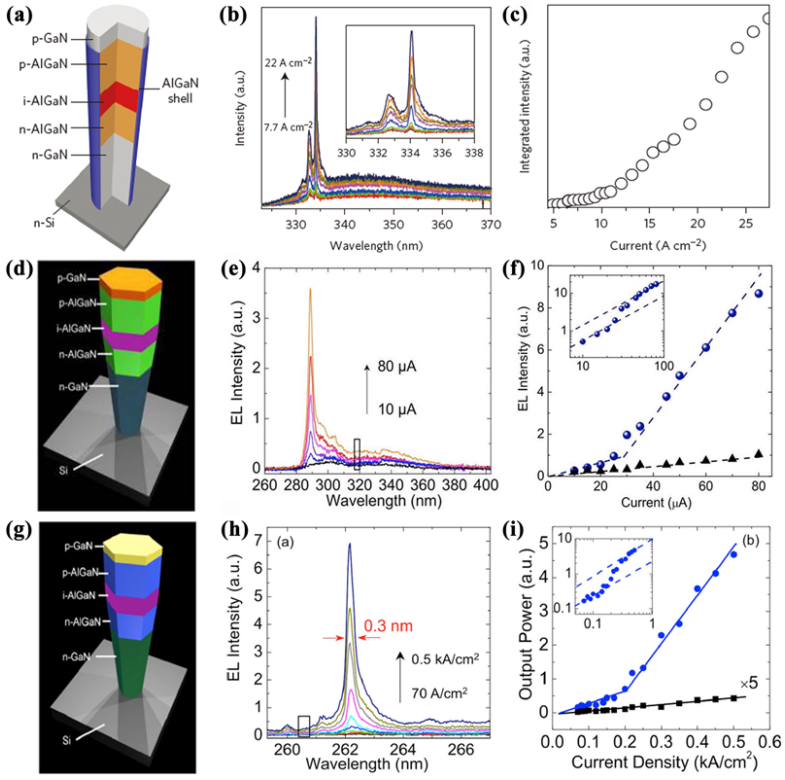

Figure 45(a)-(c) The schematic of AlGaN NW double-heterostructures (a), 6K EL spectra under different current densities (b), inset showing the enlarged view of the lasing spectra,

and integrated intensity of the lasing peak at 334.1 nm as a function of injection-current density (c);[400] (d)-(f) schematic of AlGaN NW heterostructures (d), RT EL intensity under different injection currents (e), and the EL intensity-current curve of the 289 nm lasing peak (blue circles) (f);[401] (g)-(i) schematic of the AlGaN NW laser structure (g), 77K EL spectra measured at under different injection currents (h), and EL intensity as a function of the injection current density of the 262.1 nm lasing peak (blue circles) (i).[402]

4.4 Artificial photosynthesis

The efficient, sustained oxidation of water is a critical component of a renewable, substainable, and environment-friendly fuels generator. An approach to effectively capture solar energy and directly convert it into chemical fuels is attractive for energy storage and transportation applications. This solar-to-fuel process is termed artificial photosynthesis. There are two typical categories of chemical reactions to produce fuels, such as splitting water into H_2 and O_2, and reducing CO_2 into organic molecules, as the schematic illustration in Figure 46(a) and (b). Photoelectrochemical (PEC) and photochemical (PC, or photocatalytic) are two general approaches for solar water splitting.[403-404] The artificial photosynthesis process not only requires the absorption and charge separation, but also utilizes excited charge carriers to promote electrochemical reactions in an efficient behavior. To overcome the thermodynamic barrier, splitting water into hydrogen and oxygen required at least 1.23 V of potential difference, which could be expressed as $H_2O + 1.23\ V \rightarrow H_2 + 1/2O_2$. To achieve high efficiency, it is more desirable to employ two light-absorbers with smaller band gaps to provide the necessary voltage for the electrochemical reaction. As illustrated in Figure 46(c), the bandgap of most of the metal/nonmetal-nitrides straddle the redox potential of water, with sufficient kinetic overpotentials for water redox reactions and CO_2 reduction to various hydrocarbons. The group III-nitride semiconductors possess tunable bandgap and excellent fundamental characteristics, such as excellent chemical stability, high absorption coefficient, and mobility. The development of semiconductor nanostructures supplies new opportunities to improve the performance, reliability, and scalability of artificial photosynthesis devices. In these regards, group III-nitride nanostructures have been considered as a new class of

materials for the applications of artificial photosynthesis.

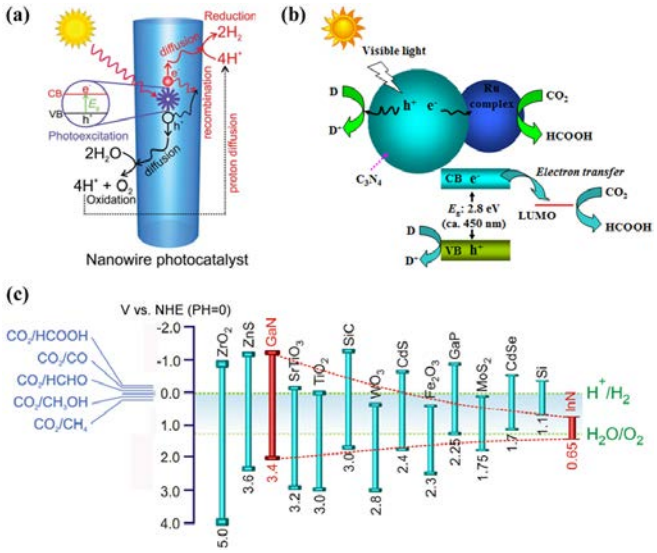

Figure 46(a) Schematic illustration of the main process steps in water splitting, including photoexcitation, carrier generation, diffusion, recombination, water oxidation, proton diffusion, and reduction reaction on the surface of nanowire photocatalysts;[405] (b) schematic of photochemical CO_2 reduction to HCOOH using a Ru complex/C_3N_4 hybrid photocatalyst;[406] (c) band edge positions of commonly reported nitride photocatalysts. The oxidation and reduction potentials of water are also shown (green dotted lines). The red dotted line represents the band edge positions of $In_xGa_{1-x}N$ with x increasing from left to right (0 - 1). The reduction potentials of CO_2 to various value added products were also shown.[405, 407]

4.4.1 Photochemical (PC) water splitting

Jung et al.[408] demonstrated the comparative study of photocatalytic activity of GaN NWs, submicron dots, and thin film. They found that the PC activity of GaN NWs was much better than that of GaN submicron dots and thin films by measuring the amount of photodegraded dye solution. The enhanced PC performance of the GaN NWs was attributed to the large surface area and high crystallity of the NWs. Thereafter, considerable efforts have been devoted to the study of PC performance of group III-nitride nanostructures. Since Wang et al.[409] demonstrated the achievement of wafer-level PC overall neutral water splitting on GaN NWs with the decoration of Rh/Cr_2O_3 core-shell nanoparticles in 2011, various approaches, including multiband NW heterostructures,[410] doping-related defect energy

states,[272] engineering surface band bending,[407, 411] incorporating visible light-sensitive dyes on NWs,[412] were developed to achieve high-efficiency one-step H_2 production from overall pure water splitting under visible-light.

The efficiency of multi-bandgap heterostructure-based photosystem was reported to have significantly higher level than that of single bandgap system because of better matching and utilization of the incident solar spectrum.[413] For example, water splitting performance of a triple-band InGaN/GaN NW heterostructures, decorated with rhodium (Rh)/chromium-oxide (Cr_2O_3) core-shell nanoparticles, was studied by Kibria et al.[410], as depicted in Figure 47(a) and (b). The triple-band NW was composed of bandgaps of 3.4, 2.96, and 2.22 eV by tuning the In incorporation during the epitaxial growth process. The Rh/Cr_2O_3 core/shell nanoparticles decorated on the surface of the triple-band InGaN/GaN NW in order to perform stable overall neutral water splitting under UV, blue, and green light irradiation. Results elucidated that the PH (~7.0) of neutral water was invariant, indicating a balanced oxidation and reduction reaction of H_2O. Moreover, the calculated H_2 production rate was ~ 92 $mmolh^{-1}g^{-1}$. The highest AQE (1.86%) was achieved at 395 - 405 nm. The photocatalytic performance of Rh/Cr_2O_3 deposited triple-band InGaN/GaN NW heterostructures was ascribed to the introduction of active reaction sites, suppression of charge carrier recombination, and enhancement in charge separation along the lateral dimension.

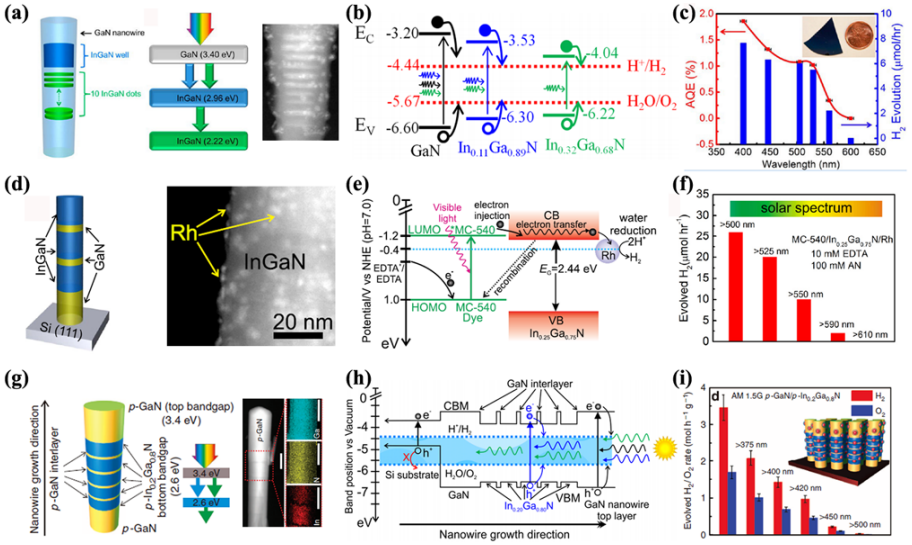

Figure 47 (a)-(c) Schematic of the InGaN/GaN NW heterostructure, the corresponding triple band and EELS spectrum image of Rh/Cr_2O_3 deposited InGaN/GaN NW (a), conduction-/valence-band edge positions of GaN, $In_{0.11}Ga_{0.89}N$, and $In_{0.32}Ga_{0.68}N$ (b), and apparent

quantum efficiency (AQE) and H_2 evolution rate as a function of the incident light wavelength (c);[410] (d)-(f) schematic of InGaN/GaN NW heterostructure and a high-resolution STEM-HAADF image of Rh nanoparticle-decorated InGaN NW (d), reaction mechanism of MC-540 dye-sensitized $In_{0.25}Ga_{0.75}N$/Rh NWs (e), and H_2 evolution from 10 mM EDTA and 100 mM AN mixture under 300W Xenon lamp (f);[412] (g)-(i) schematic of the double-band *p*-GaN/*p*-$In_{0.2}Ga_{0.8}N$ NW heterostructure, the concept of double-band photocatalyst, and STEM-HADDF image (g), flat-band diagram of the GaN/$In_{0.2}Ga_{0.8}N$ NW heterostructure (h), H_2 and O_2 evolution rates in overall water splitting with AM1.5G filter, the inset showing a schematic of core/shell Rh/Cr_2O_3 nanoparticle decorated double-band NW photocatalyst.[411]

In order to more effectively ultilize the longer wavelength (＞500 nm) towards deep-visible and NIR solar spectrum, higher In composition of InGaN NWs is an alternative approach to extend the absorption edge. However, the development of high-quality InGaN with high In concent (＞50%) was extremely difficult due to the large lattice mismatch (~11%) between InN and GaN, spinodal decomposition, In phase separation, and In surface segregation. Alternatively, Kibria et al.[412] demonstrated Merocyanine-540 (MC-540) dye-sensitized and Rh-decorated MBE-grown InGaN NWs to extend the solar absorption of InGaN NWs towards longer visible solar spectrum, as illustrated in Figure 47(d) and (e). The reaction mechanism was expressed as following: (1) MC-540 + *hv* (λ＞500 nm) → * MC-540, (2) * MC-540 → $In_{0.25}Ga_{0.75}N$ (e^-) + $(MC\text{-}540)^+$, (3) $In_{0.25}Ga_{0.75}N$ (e^-) → $In_{0.25}Ga_{0.75}N$ + Rh(e^-), (4) Rh ($2e^-$) + $2H^+$→ H_2, (5) $(MC\text{-}540)^+$ + EDTA (e^-) → MC-540 + EDTA (oxidized). Thus, this work provided a viable approach to harness deep-visible and NIR solar energy for efficient and stable water splitting.

In addition, tuning near-surface band bending on group-III nitride nanostructures was another effective approach to realize high efficiency and stable overall water splitting under the UV and visible-light irradiation. The upward- (downward-) band bending was usually observed in the near surface region of *n*- (*p*-) type semiconductors, which generated a energy barrier for the migration of photogenerated electrons or holes towards the semiconductor-liquid interface.[414] As a result, the oxidation or reduction reaction was suppressed at the NW surface, thereby suppressing the overall water splitting efficiency. Kibrial et al.

demonstrated the improved quantum efficiency by tuning the near-surface band bending on *p*-GaN NWs.[415] The achievement of efficient and stable stoichiometric dissociation of water into H_2 and O_2 under visible light by eradicating the potential barrier on nonpolar surfaces of *p*-type InGaN: Mg NWs.[411] For the case of the photocatalytic performance of *p*-type GaN NWs, the APCE was enhanced to ~51% under 200 - 365 nm.[415] Subsequently, they developed and designed a double-band *p*-GaN: Mg/*p*-$In_{0.2}Ga_{0.8}N$:Mg NW heterostructure, as the schematic illustrated in Figure 47(g)-(i).[411] Flat band-gap diagram of the heterostructure exhibited the conduction-band and valence-band edge positions of GaN, $In_{0.2}Ga_{0.8}N$, and the underlying Si substrate. In comparison with the redox potentials of water (shown by the dotted lines), GaN and $In_{0.2}Ga_{0.8}N$ possessed sufficient overpotential for oxidation and reduction of water. Under full arc illumination with AM1.5G optical filter, the NW heterostructure achieved an APCE of ~69% and AQE of ~12.3% in the range of 400 - 470 nm, and the solar-to-hydrogen (STH) conversion efficiency was estimated to be ~1.8%.[411]

4.4.2 Photoelectrochemical (PEC) water splitting

In the past few years, diverse stratagies were developed to modify PEC water splitting and H_2 generation performance using GaN-based nanostructures. Hwang et al.[416] studied the PEC performance of $In_xGa_{1-x}N$ (x=0.08-0.1) NWs grown on planar Si and Si NW arrays substrates as the photoanode, as shown in Figure 48(a) and (b). As presented in Figure 48(c), the InGaN/Si hierarchical arrays achieve a photocurrent at an onset voltage of 0.1 V *vs*. RHE, and reached a photocurrent density of 33 μA/cm^2 at 1.23 V *vs*. RHE, which is 5 times higher than the NW arrays grown on planar Si substrates, because of a higher surface area for the electrochemical reaction and increased optical pathway in the hierarchical arrays. Similarly, Beaton et al.[417] demonstrated that the GaN NR arrays based PEC system exhibited a significant enhancement with a factor of 6 in photocurrent density compared to planar GaN photoelectrode.

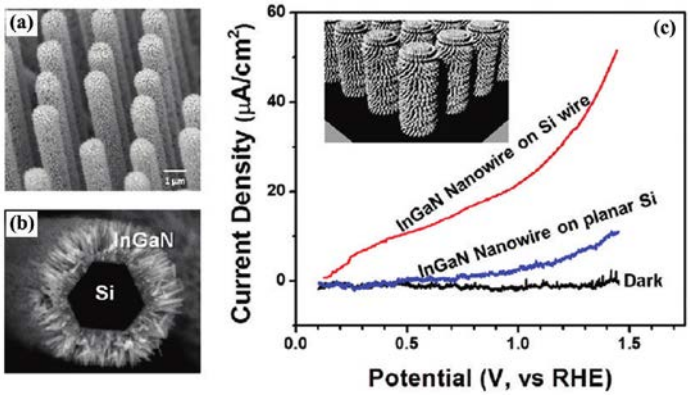

Figure 48 (a) Tilted and (b) cross-section SEM images of Si/$In_xGa_{1-x}N$ NW arrays on Si(111) substrate; (c) photocurrent density plots of hierarchical Si/$In_xGa_{1-x}N$ (red) and planar Si/$In_xGa_{1-x}N$ (blue) under 100 mW/cm^2 and dark, inset showing the schematic of Si/$In_xGa_{1-x}N$ NW arrays.[416]

The incorporation of dopants in III-nitride nanostructures was a feasible approach to improve the PEC performance of water splitting.[418-420] Wallys et al.[418] reported the electrochemical performance of Si- and Mg-doped GaN NWs. AlOtaibi et al.[421] investigated the PEC properties of undoped and Si-doped GaN NW arrays in HBr and KBr electrolytes. Under ~350 nm light illumination, maximum IPCE of ~15% and 18% were measured for undoped and Si-doped GaN NWs, respectively. Kamimura et al.[420] reported PEC properties of *n*- and *p*-type InGaN NWs for water splitting using *in situ* electrochemical mass spectroscopy (EMS). The IPCE of *p*-type $In_{0.04}Ga_{0.96}N$ NWs was around 40% at a bias potential of -0.45 V/NHE with monochromatic light using band-pass filters for a wide spectra range (up to 750 nm). Both photocurrent and H_2 evolution were stable for 60 min.

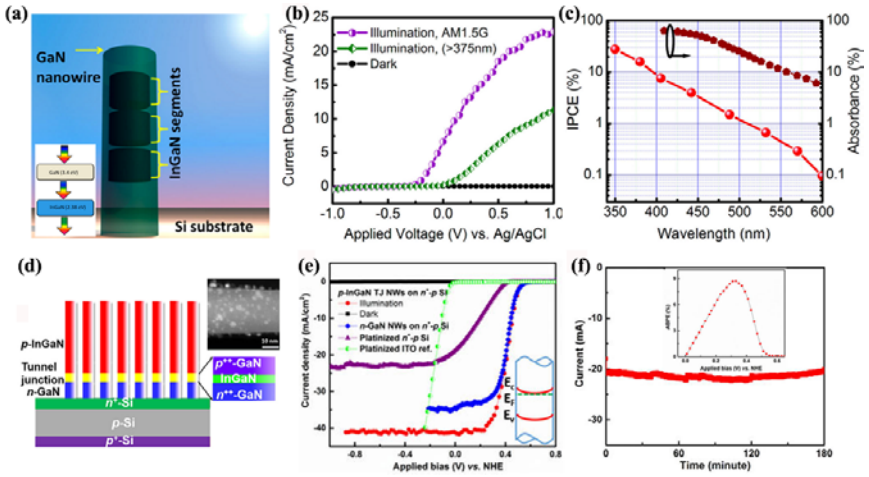

Figure 49 (a)-(c) Schematic of InGaN/GaN core/shell NW structures and the double band (a),

variations of the current density with applied voltage (vs Ag/AgCl) in 1 mol/L HBr under AM1.5G illumination (b), and IPCE of InGaN/GaN NW photoelectrodes measured at an applied bias of 1 V (vs Ag/AgCl) in 1 mol/L HBr in log scale (c); [422] (d)-(f) the schematic of InGaN TJ NWs on n+-p Si substrate and the STEM image of Pt nanoparticles-decorated InGaN TJ NW (d), the change of current density with applied voltage versus NHE for the NWs in 1 M HBr solution under different conditions (e), and stable photocurrent for 3 h at an applied bias of 0.06 V versus NHE under 1.3 sun of AM1.5G illumination, inset showing the ABPE of the photocathode formed by InGaN TJ NWs.[423]

Various III-nitride hetrostructures, including InGaN/GaN core-shell NWs,[422] NiO decorated InGaN/GaN NRs,[424] InGaN/GaN nanoporous structure,[425] 3D GaN-InGaN core-shell NRs array,[426417] InGaN/GaN MQW coaxial NWs,[427-428] and InN/InGaN QDs,[429] have been designed and fabricated to enhance the absorption of visible solar spectrum. AlOtaibi et al.[422] demonstrated the stable PEC water splitting and H_2 evolution under UV and visible light irradiation using PAMBE-grown *n*-type InGaN/GaN core/shell double-band NW photoanode in HBr solution, as illustrated in Figure 49(a)-(c). A current density of ~23 A/cm^2 under AM 1.5 G illumination was obtained at 1 V, and an IPCE of 27.6% was achieved at 350 nm at 1V *vs.* Ag/AgCl. Moreover, no visible photo-oxidation of InGaN/GaN NW photoelectrode could be observed after 24h measurements in 1 mol/L HBr electrolyte due to the relatively high quality of InGaN/GaN NW structures. Benton et al.[424] observed a PEC reduction from MOCVD-grown InGaN/GaN NRs photoelectrode in NaOH electrolyte. The addition of NiO nanoparticles suppressed the PC etching of the NWs and the carrier recombination, promoting oxidation reaction on its surface rather than on the NW surface. Benton at al.[425] reported water splitting application using GaN and InGaN/GaN nanoporous structures with pore sizes ranging from 25-60 nm, which were obtained by PEC etching in KOH solution. The nanoporous structures showed a higher photocurrent density (~4 fold) than that of as-grown planar devices, and the IPCE of InGaN/GaN device reached 46% at 355 nm. Caccamo et al.[426] investigated the PEC performance of 3D GaN/$In_xGa_{1-x}N$ core/shell rod arrays with In concentration of ~0.3. The 3D GaN/$In_xGa_{1-x}N$ heterostructures showed improved PEC properties than that of GaN NRs. Ebaid et al.[427] investigated the PEC water splitting performance of InGaN/GaN MQW coaxial NW photoanode. By carefully

tuning the QW thickness in coaxial NWs, an IPCE attained a maximum value of ~15% at 1V under 350 nm UV light illumination. Recently, Alvi et al.[429] reported the PEC water splitting efficiency of epitaxial InN QDs decorated $In_{0.54}Ga_{0.46}N$ photoelectrode was double higher than that of $In_{0.54}Ga_{0.46}N$ photoelectrode, and a maximum IPCE of InN/$In_{0.54}Ga_{0.46}N$ photoelectrodes achieved a value of 56% at 1 V vs.Ag/AgCl at 600 nm with photostability.

To achieve high solar-to-hydrogen efficiency, compared to single light absorber, a dual/multiple light absorbers have been employed to absorb a wide range light of solar spectrum, reducing the operation voltage for PEC water splitting.[423, 430-431] Fan et al.[423] reported the fabrication and performance investigation of a dual absorber photocathode, consisting of *p*-InGaN/tunnel junction/*n*-GaN NW arrays and a Si solar cell wafer, as illustrated in Figure 49(d)-(f). The onset potential of InGaN TJ NWs on n^+-p Si substrate was at V_{NHE}=0.5 V for the current density of -2 mA/cm^2 and a saturated photocurrent density reached -40.6 mA/cm^2 at V_{NHE}=0.26 V. Moreover, maximum applied bias photon-to-current efficiency (ABPE) of 8.7% was obtained at V_{NHE}=0.33 V under 1.3 sun of AM1.5G illumination. The current remained nearly constant and showed a high-level stability for the duration of 3h. Most recently, Fan and co-workers further demonstrated the optimized PEC performance of an InGaN/Si double-band photoanode, with the nearly ideal bandgap configuration of 1.75/1.13 eV for maximum solar-to-hydrogen conversion.[431]

4.4.3 PC/PEC CO_2 reduction

At present, various stratagies were developed to obtain high conversion efficiency of CO_2 into usable energy, including (1) doped (Ge and Mg) Ga(In)N NW arrays for tunable photocatalytic activity of CO_2 reduction;[432-433] (2) depositing Pt or Rh/Cr_2O_3 core-shell nanoparticles on the surface of GaN NWs;[434] (3) monolithically integrating GaN NWs/Si solar cell photocathode.[435] AlOtaibi et al.[434] demonstrated the photocatalystic activity of the nonpolar surfaces of GaN NWs for the PC reduction of CO_2 into CH_4 and CO under UV light irradiation, as shown in Figure 50(a)-(f). The comparative study of CH_4 and CO production of bare GaN NWs, Pt and Rh/Cr_2O_3 core-shell nanoparticles decorated GaN NWs showed that the CH_4 production was improved and the CO production was suppressed by an

order of magnitude with Rh/Cr_2O_3 core-shell nanoparticles decoration. The enhancement of CH_4 production was attributed to the effective adsorption and hydrogenation of CO_2 molecules on Rh/Cr_2O_3, and the decrease of CO production was ascribed to the photoexcited electrons collected by Rh/Cr_2O_3 nanoparticles. CH_4 production of Pt nanoparticles-decorated GaN NWs exhibited an order of magnitude higher than that of bare GaN NWs. Linear increase of both CO and CH_4 production indicated stable photocatalytic CO_2 reduction. AlOtaibi et al.[433] further demonstrated the photoreduction of CO_2 into methanol (CH_3OH) using unpolar InGaN/GaN NWs as the photocatalysts. A conversion rate of 0.5 mmol g_{cat}^{-1} h^{-1} for CO_2 into CH_3OH was achieved under visible light (＞400 nm) illumination. Additionally, the photocatalytic activity of CO_2 reduction was enhanced by incorporating a small amount of Mg dopant.

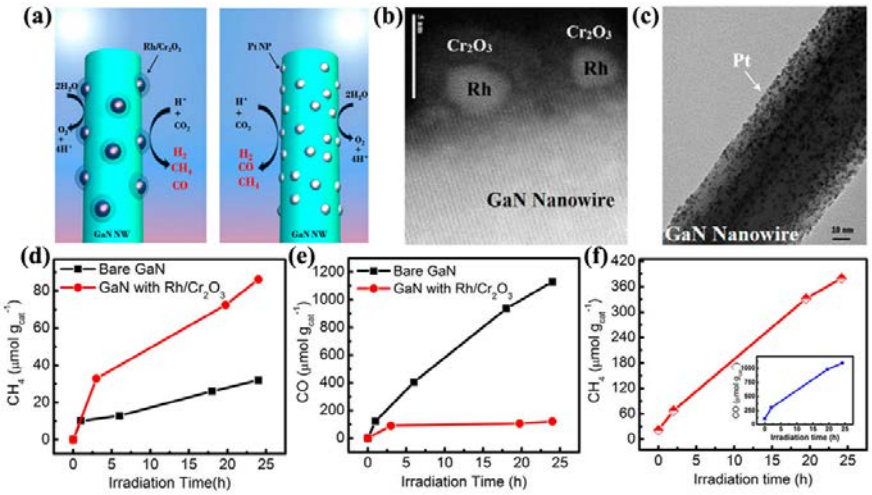

Figure 50 (a) Schematic of the photoreduction of CO_2 on Rh/Cr_2O_3 (b) and Pt (c) nanoparticles-decorated GaN NWs; (d) CH_4 and (e) CO production on bare and Rh/Cr_2O_3 core/shell nanoparticles-decorated GaN NWs as a function of illumination time; (f) CH_4 evolution over Pt-decorated GaN NWs, and inset showing the CO generation.[425]

Although efforts have been devoted to improving the CO_2 conversion efficiency, there is still a long way to realize the goal with the help of utilization of nanostructured III-nitride photocatalysts and photoelectrodes under UV, visible and NIR solar spectrum in the near future.

4.5 Field emitters

Field emission (FE) is based on a physical phenomenon of quantum tunneling in which the electrons are injected from the surface of materials into vacuum under the influence of an external applied electrical field. The FE mechanism is explained by the the Fowler and Nordheim (FN) theory. The FE properties are highly dependent on both the properties and morphology of the material and the shape of the particular cathode,[436] such as electron affinity, work function, conductivity, aspect ratio, growth density, morphology, and so on. The current density produced by a given electric field is described by the FN equations:[437]

$$J = \left(A\beta^2 E^2 / \phi\right)\exp\left(-B\phi^{3/2} / \beta E\right) \qquad (16)$$

$$I = S \times J\,, \quad E = V / d \qquad (17)$$

$$\text{or } \ln\left(J/E^2\right) = \ln\left(A\beta^2 / \phi\right) - B\phi^{3/2} / \beta E \qquad (18)$$

where A and B are constants (A = 1.54×10^{-6} A eV V^{-2}, B = 6.83×10^{3} $eV^{-3/2}$ V μm^{-1}), S is the emitting area, V is the applied potential, I is the emission current, β is the field-enhancement factor, d is the distance between a sample and the anode, and ϕ is the work function of the emitting materials. From FN model and field-enhancement factor, β, materials with low or negative affinity, low work function, elongated geometry and sharp tips or edges are expected to have a great emission current. Figure 51 illustrated the phenomenon of FE obtained from a nanostructure.

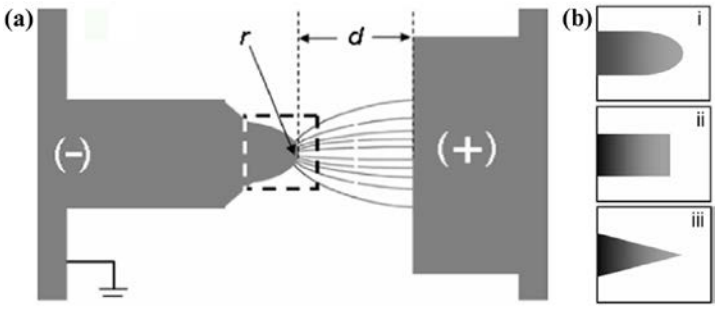

Figure 51 (a) The FE phenomenon at the tip of an emitter of a nanostructure; (b) different tip geometry of an emitter, such as (i) round tip, (ii) blunt tip, and (iii) conical tip.[427]

To date, the FE performances of group III-nitride nanostructures with controlled composition[36, 66] and morphology,[166, 438] doping,[439] surface docration,[440-441] patterned growth,[116] thermal treatment,[442] using conductive substrates,[18, 20, 443]

were investaged. Ji et al.[58] reported the temperature-dependent FE performance of CVD-grown AlN nanotips [Figure 52(a)]. The E_{to} and E_{thr} decreased gradually with an increase in temperature from 300 to 573 K. Meanwhile, the emission current density increased with the temperature rising. The decrease of E_{to} and the increase of emission current density with the increase in the temperature was due to the decrease in the effective work function of the AlN nanotips. The field enhancement factor β was estimated to be 483 - 1884 as the temperature increased from 300 - 573 K, and the corresponding effective work function was calculated to be 0.060 - 0.024 eV. The emission current fluctuation had been found to be less than 8% at 8.0 V/μm in 1000 min. Our group demonstrated the excellent FE performance of CVD-grown AlN nanotips on conductive carbon cloth.[18] By employing the flexible and conductive carbon cloth, the E_{to} of the AlN nanotips reduced to be as low as 1.1 V/μm, and the field enhancement factor was as high as 6895, indicating that the AlN nanostructures grown on carbon cloth were promising for the nanoscale flexible electronics. The CVD-grown AlN NWs on graphite sheet and AlGaN NWs on carbon cloth with improved FE performance were also demonstrated.[20, 66]

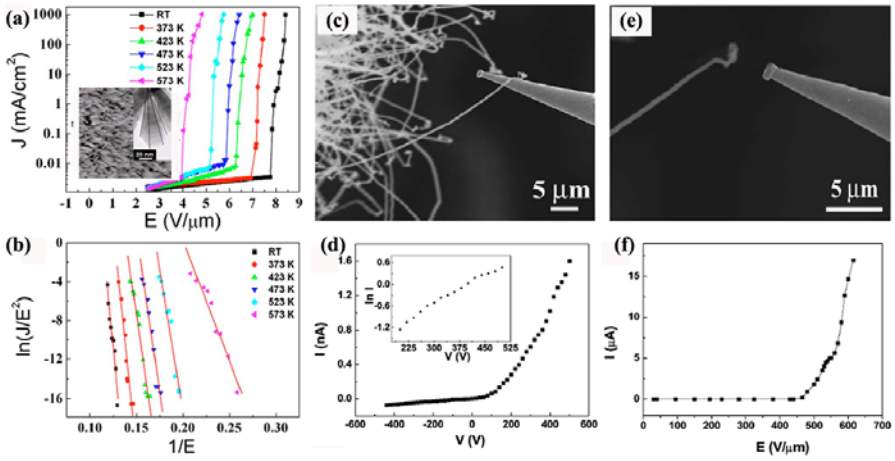

Figure 52(a)-(b) *J-E* plot of the AlN nanotips under different temperature, inset showing the SEM image of the sample (a), and the corresponding FN relationship of $\ln(J/E^2)$-$1/E$ plot (b);[58] (c)-(f) The SEM images of individual AlN NW and the tungsten probe during the conductivity measurement (c) and the FE measurement (e), representative electrical transportation curve of a single AlN NW, inset showing I-V curve (d), and the FE *I-E* curve of a single NW (f).[166]

In addition to the electron affinity and aspect ratio, the electrical conductivity is also

necessary to be considered in the FE properties of III-nitride nanostructures, and can be measured by studying single nanostructure. In this regard, Liu et al.[166] investigated the electrical transport and FE performance of an individual ultra-long AlN NW. *In situ* conductivity and FE measurements on individual ultra-long AlN NW were performed in a modified SEM system, as shown in Figure 52(c) and (e). As the *I-V* and *I-E* curves of the individual AlN NW described in Figure 52(d) and (f), an average conductivity was estimated to be 2.7×10^{-4} Ω^{-1} cm^{-1}, and mean electric field was 440 V/μm for 1 nA and 480 V/μm for 1 μA, respectively. Although the electric conductivity and FE of the AlN NW were not good enough for FE applications, the work offered an effective approach to find the possible factors which might influence the FE behaviors.

In general, the turn-on (E_{to}) and threshold electric fields (E_{thr}), which are defined as the electric field (E) values required to produce a current density of 10 μA cm^{-2} and 1 mA cm^{-2}, respectively, are usually employed to assess the FE performance. The FE performance of group III-nitride nanostructures was compared and listed in Table 11.

Table 11 FE properties of group III-nitride nanostructures

Material	Morphology	E_{to} @10 μA cm^{-2} (V/μm)	E_{thr} @1 mA cm^{-2} (V/μm)	β	Ref.
AlN	nanowires	~0.67	~0.74	8.2×10^{4}	[180]
	nanotips	10.8(12.2)	13.6(15.2)	367(317)	[62]
	nanoneedles	3.1	~8.5	748	[444]
	nanorods	8.8	19.2 (10.31 mA cm^{-2})	565	[445]
	nanoplatelets	3.2-5.0	7.8-12.1 (10 mA cm^{-2})	1015-1785	[446]
	nanotubes	0.8	3.0	8000	[447]
	nanotips	6	10 (0.22 A cm^{-2})	—	[448]
	nanocones	17.8	＞40	340	[449]
	nanocones	4.8-15.2	11.2-29.5	436-1561	[116]
	Core-shell nanocones	7.8-15.2	14.8-23.1	—	[441]
	Si-doped nanoneedles	1.8	4.6 (10 mA cm^{-2})	3271	[450]
	Aligned nanorods	2.25	3.58	784	[451]
	Multilayer nanostructures	2.7	7.1	—	[176]
	Ultra-lone nanowires	4.5-6.5	10.4-15.5	1138-1997	[166]
	CsI-decorated nanostructures	7.0-14.2	13.6-28.6	—	[440]

	Doped nanocones	7.07-8.09	12.84-15.96	—	[439]
	nanocones	3.2-7.9	—	286-484	[438]
	nanotips	3.9-7.7	4.1-7.9	483-1884	[58]
	nanowires	4.9-5.8	6.7-8.4	607-825	[20]
	Radical nanotips	1.1-2.3	1.5-2.5	847-6895	[18]
	naowires	12	14(0.02 mA cm^{-2})	—	[452]
	nanorods	9.5(0.2 μA cm^{-2})	18	—	[453]
	nanowires	3.96	—	1050	[454]
	nanowires	8.4	10.8 (0.96 mA cm^{-2})	474	[455]
GaN	Durian-like nanostructures	8.24	10.18	—	[456]
	nanograss	7.82	8.96	—	[457]
	nanowires	4.39	12.3	2087	[458]
	nanocolumns	2.5, 2.6	4.7, 5.1	3959, 9725	[61]
	Conical-like nanorods	3.35	4.45	926	[459]
	nanocables	1.4 (0.1 μA cm^{-2})	3.4(0.1 mA cm^{-2})	1400	[460]
	Aligned nanoneedles	2.1	4.5	2835	[461]
	P-doped microtube	2.9	9.5(3 mA cm^{-2})	2774	[462]
	nanofingers	9.7	—	156	[235]
InN	nanotips	0.9	—	69000	[463]
	nanocones	12.5	30.4	1465	[63]
AlGaN	nanocones	7.35-16.5	13.89-30	—	[36]
	nanowires	1.6-3.6	2.1-4.2	423-6032	[66]
InGaN	nanowires	10 (2.8 μA cm^{-2})	24(2.9 mA cm^{-2})	640	[147]

4.6 Solar cells

A solar cell, also called a photovoltaic (PV) cell, is an electrical device that converts the light energy directly into electricity *via* the photovoltaic effect.[464] Compared to Si and other conventional III-V materials, more attention have been paid to the development of III-nitride NWs solar cells due to the tunable direct bandgap enegy from ~6.2 eV for AlN to ~0.65 eV for InN, which can enable the application of full-solar-spectrum PV devices. Furthermore, the advantages of using 1D nanostructure arrays with high crystalline quality in PV devices includes (1) the forming of vertical radial junctions allows extended absorption paths while maintaining short distances for carrier collection; (2) strong light trapping and reduced reflection can be achieved by using NWs; (3) manipulation of material properties will be possible when the size of nanostructures is small enough for quantum effects, and (4)

structures can be grown using a little material and thus at much lower cost.[465]

In 2008, Tang et al.[131] demonstrated the *p*-GaN:Mg NRs/*n*-Si heterojunctions for the PV applications, as shown in Figure 53(a)-(c). The PV cell exhibited well-defined rectifying behavior in the dark with a large rectification ratio. Under illumination from a calibrated solar simulator with intensity of 100 mW/cm^2, a maximum power conversion efficiency reached ~2.73 %. The schematic energy band diagram of the *p*-GaN NR/*n*-Si heterojunction diode at thermal equilibrium illustrated the explanation of the rectifying behavior of the cell. An asymmetrical energy barrier for electrons was formed at the junction due to the large bandgap difference between Si and GaN, resulting in the decrease of electron diffusion and electron-hole recombination in GaN NRs. The built-in field naturally led to the low hole injection into the *n*-Si side, and wide bandgap GaN NRs on the top of the heterojunction decreased the leakage current in the depletion region. Under illumination from the top, photons (whose energy was between E_g(GaN) and E_g(Si)) would transmit through NRs, and were absorbed by Si, while light with photon energies larger than E_g(GaN) was absorbed by GaN NRs. The holes and electrons generated in both sides of the heterojunction were collected effectively due to the large built-in electric field at the junction and thus yielded the photocurrent.

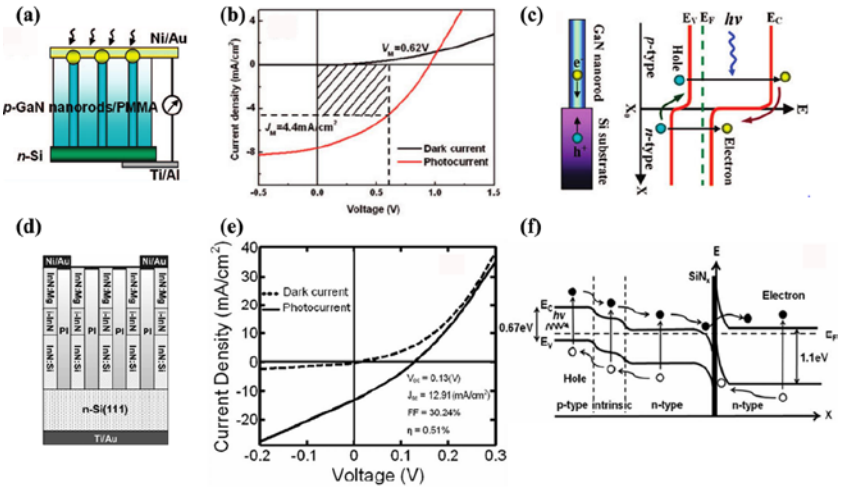

Figure 53(a)-(c) Schematic of the *p*-GaN NR/*n*-Si heterojunction photovoltaic cell (a), current density *vs* voltage for the PV cell in the dark and under simulated AM1.5G illumination (b), and schematic energy band diagram of the heterojunction diode showing the photogenerated carrier transfer process (c);[131] (d)-(f) schematic illustrations of InN:Mg/i-InN/InN:Si NW solar cells on *n*-type Si substrate (d), *I*-*V* characteristics of the NW solar cells under dark and

illumination (1-sun at AM1.5G) conditions (e), and illustration of the corresponding energy band diagram of the NW junction under thermal equilibrium (f).[466]

Later on, Nguyen et al.[466] reported the experimental demonstration of InN NW solar cells, as depicted in Figure 53(d)-(f). The InN *p*-i-*n* NWs based solar cell exhibited characteristics of a diode structure under dark conditions, with a rectifying ratio of ~60 measured at –1 and +1 V. Under simulated AM 1.5 G illumination on the device with area of 1 mm^2, the short-circuit current density, open-circuit voltage, fill factor, and power-conversion efficiency were ~12.91 mA/cm^2, ~0.13%, 30.2 %, and 0.51%, respectively. The performance of the device can be explained by the energy-band diagram under thermal equilibrium, which possessing narrow depletion region widths between InN and Si substrare, due to the high doping concentrations in InN and Si.

Both InGaN/GaN MQW solar cells with periodic NR and nanohole array operating at a wavelength of 520 nm exhibited improved performance, and the conversion efficiency of nanohole array solar cell was 1.28 %, higher than that of nanorod array (1.12 %), attributing to more effective optical coupling between the nanohole array and the incident sunlight, and a higher density of waveguide modes available in nanohole array than in the NR array. [467] However, the conversion efficiency of PV based on III-nitrde NWs is low. [468-470]

4.7 Other applications

4.7.1 Gas sensors

III-nitride nanostructure based gas sensors were mostly decorated with metal nanoparticles, for example, Pt-coat InN NRs,[471] Pd-coated GaN NWs, [472] Pt-coated InN NBs,[473] and Pt-coated porous GaN nanonetwork[474] for H_2 detection, Au-coated GaN NWs for N_2 and CH_4 detection,[475] and defect GaN NWs for CH_4 detection.[476]

The mechanism of the decorated metals on the sensitivity of gas sonsors was investigated. Dobrokhotov et al.[475] compared the electrical properties of GaN NWs gas sensors with/without AuNPs decoration as a function of exposure to Ar, N_2, and CH_4, as illustrated in Figure 54(a)-(f). The device exhibited a linear ohmic behavior insensitive to the environment without AuNPs, while the *I-V* curves of the devices with AuNPs were nonlinear

with a drop of 5 orders in the current value, suggesting the Au-coated GaN NWs device was sensitive to the different gas environment. The sensoring mechanism of the AuNPs-coated GaN NWs was proposed as following: (1) the conducting channel of the intrinsically n-type GaN NW was reduced as the AuNP was formed on its surface; (2) charge transfer across the Au/GaN interface created a depletion region within the NW and resulted in the shrinkage of conducting channel in the GaN NW; (3) physisorption of the gases on the Au NPs induced a negative potential, which further increased the depletion layer thickness and reduced the conductance.

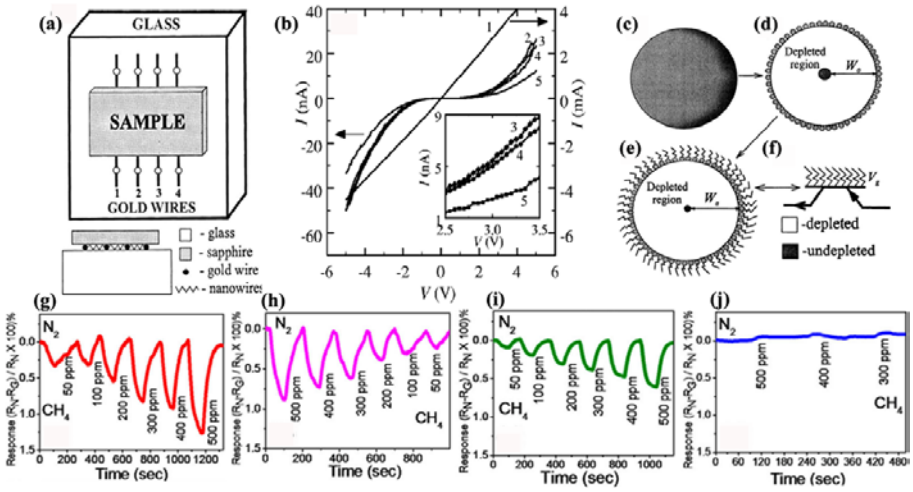

Figure 54 (a)-(f) The schematic of Au-coated GaN NWs gas sensor (a), (b) I-V curves of a sensor constructed from bare GaN (curve 1) NWs and Au-coated GaN NWs (curves 2-5) for in vacuum (2), Ar (3), N_2 (4), and CH_4 (5) (b), and a cross-section view of an NW showing the size of the conducting region (grey) with no AuNP on the surface (c), with a layer of AuNPs on the surface in vacuum (d), with gas physisorbed on the surface of the NPs (e), and an equivalent circuit diagram representative of the operation of the NW as a gas-sensitive FET with Vg representing the induced potential by the absorbed molecules (f). W_0 was the depletion depth due to just AuNPs on the NW surface and W_a was the depletion depth when gas molecules had been physisorbed onto the AuNPs;[475] (g)-(j) temporal responses of CH_4 sensing by four devices made of NW samples obtained under different O impurity concentrations of ~10^5 ppm (g), 10^3 ppm (h), 10^2 ppm (i), and <2 ppm (j).[476]

Later on, RT ppm concentration of H_2 detection using Pd-coated CVD-grown GaN NWs was reported by Lim et al.[472] By comparing the measured resistance as a function of time from uncoated and Pd-coated GaN NWs exposed to a series of H_2 concentrations (200-1500

ppm) in N_2 for 10 min at RT, Pd-coated GaN NWs exhibited the significantly improved sensitivity to low ppm level H_2 by a factor of up to 11. Notably, Pd-coated GaN NWs showed gradually increased response from 7.4% to 9.1% as the increase of H_2 concentration in the range of 200-1500 ppm in N_2 after a 10 min exposure. Gas detection mechanism was attributed to the change in atomic H concentration at the interface upon H_2 and air exposure, causing the change in the resistance. In addition, these sensors exhibited low power consumption (＜0.6 mW) at 300 K. Similar approach was also employed to study the H_2 sensing characteristics of Pt-coated MOCVD-grown InN NBs.[473] By increasing the H_2 concentration from 20 to 300 ppm in N_2 ambient, the relative reponse gradually increased from 1.2 % to 4 %. Moreover, Pt-coated InN NB sensors were also operated at low power levels (~0.5 mW). Zhong et al.[474] studied a Pt-coated porous GaN nanonetwork Schottky diode type H_2 sensor and its performance. This Schottky diode based on porous GaN nanonetwork was able to perform well at RT in detecting H_2 gas with concentrations from 320 to 10000 ppm, and the relative response was ~23% in 10000 ppm H_2.

Recently, Patsha et al.[476] reported CVD GaN NWs without any metal clusters and functional groups on the CH_4 sensing. Intentional lattice oxygen defects were created on the surfaces of GaN NWs. GaN NWs with different O impurity concentrations showed the response of reduction in reistance, under the exposure with CH_4, as shown in Figure 54(g)-(i). It was proposed that the presence of $2(O_N)$ and V_{Ga}-$3O_N$ defect complexes resulted in the variation of CH_4 gas sensing behavior of O-rich GaN NW ensemble. A locoliaed charge transfer processes contributed the global gas sensing behavior. Therefore, for III-nitride nanostructure-based sensing devices without decoration of metal particles, the sensor response could be optimized by controlling the surface defects.

4.7.2 Nanogenerators

The concept of the nanogenerators was first introduced by Wang et al. through examining the piezoelectric properties of ZnO NWs with an AFM.[477] The mechanical energy was converted into electrical energy by means of piezoelectric ZnO NW arrays. The presence of polar surfaces and the lack of center symmetry, which results in a piezoelectric

effect, make ZnO one of the hottest candidates for nanogenerators. Group-III nitride nanostructures also have an outstanding piezoelectric property owing to their WZ crystal structures, similar to that of ZnO. The coupling of piezoelectric and semiconducting properties creates a strain field and charge separation across the NW as a result of its bending. Therefore, an output power can be generated by scanning an AFM tip in contact mode across 1D group-III nitride nanostructures. For example, Wang et al.[155] reported the piezoelectric performance of a family of CVD-grown group-III nitride nanostructures, including AlN and AlGaN nanocones, GaN NRs and InN nanocones, as shown in Figure 55. Piezoelectric responses of the nanocone/NR quasi-aligned arrays were examined using AFM in contact mode with a conducting Pt-coated tip. Sharp voltage pulses were detected for all of the nanostructures, except for AlN, and the corresponding output voltage were 4, 7, and 60 mV for AlGaN, GaN, and InN, respectively. The voltage pulses approximately occurred when the AFM tip scanned across the nanocones/NRs. This indicated that the discharge took place when the tip contacted with the compressed side of the 1D nanostructures.

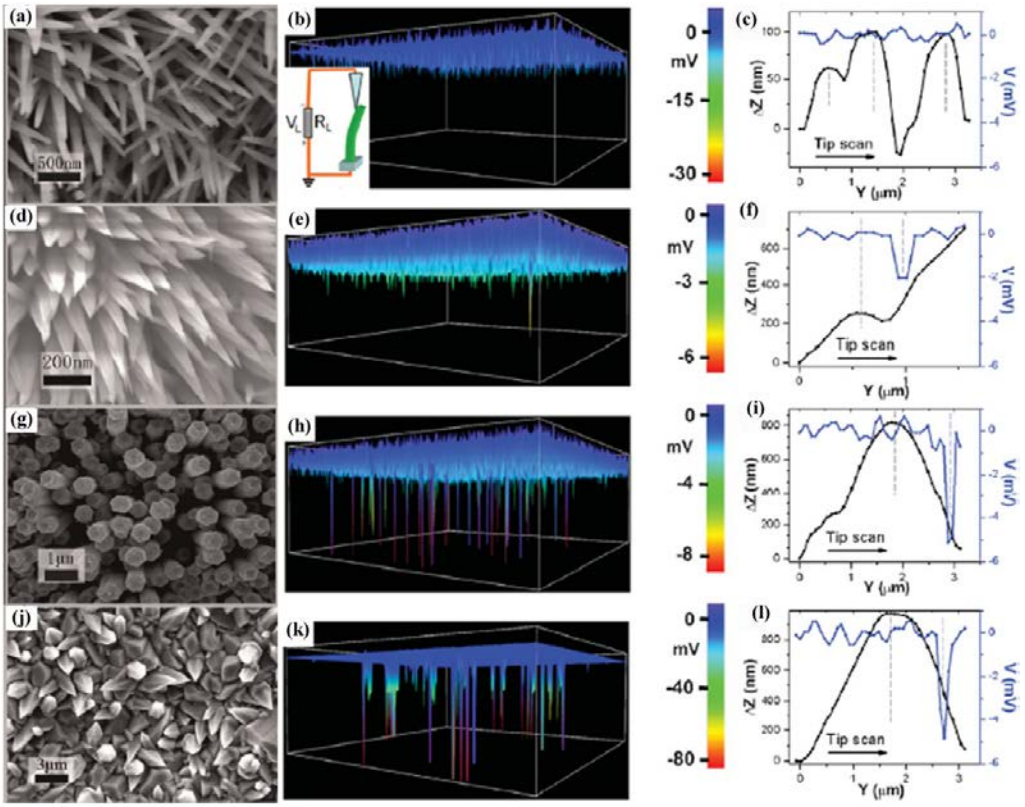

Figure 55 Typical SEM image, 3D electric signal images (middle), and corresponding voltage profiles and line-scan topography profiles (right, blue/right, black respectively) of the

group-III nitride nanostructures: (a)-(c) AlN, (d)-(f) AlGaN, (g)-(i) GaN, (j)-(l) InN.[155]

Liu et al.[478] investigated the piezoelectric nanogenerators (NG) based on PAMBE grown p-type and intrinsic InN NWs. The p-type InN NW based NGs showed 160% more output current and 70% more output power than the intrinsic InN NW based NGs. The higher output power of the *p*-type reflected better piezoelectric energy conversion efficiency than intrinsic NGs. The higher output current of *p*-type NGs reflected much lower impedance than intrinsic NGs. Both results were due to lower electrostatic losses in p-type NGs enabled by a more advantageous NW morphology, longer and narrower NWs and increased NW area density, resulting from Mg doping.

5. Summary and future outlook

In this review, we have presented a comprehensive view on the synthesis and properties of group-III nitride nanostructures. The unique properties of well controlled group-III nitride nanostructures have paved the way for the applications in the fields of microelectronics and optoelectronics, energy storage, sensors, and environmental science and engineering. Specifically, III-nitride-nanostructures showed great potentials in (1) LEDs in the full color range from DUV to NIR through tuning bandgap of Al/(Ga/In)/N nanostructures and constructing special *p*-*n* homo/heterostructures, (2) DUV to NIR lasers with ultralow threshold, small scale, (3) high-responsivity PDs operated in a broad spectra range from DUV to NIR, (4) high-efficinecy and stable artificial photocatalysis (water splitting and CO_2 reduction) uder UV, visible, and NIR light irradiation, and so on.

Although great efforts have been put into the controlled growth of nitride nanostructures with high quality and desired properties, there are still a number of challenges need to be addressed, for examples:

(1) To control accurately growth of single-phase nitrides ternary alloys in the entire composition range, to restrain the spontaneous tendency of the phase separation in nitrides ternary alloys, especially AlInN.

(2) To optimize the performance of diverse optoelectronic devices. Fundamental physics and in-depth understanding of processes occurring during nanostructures growth and

device operation are needed. Further experimental and theoretical studies on the electrical and thermal transport, carrier injection efficiency, and lateral band bending of such nano- or sub-micron scale structures without degrading the electronic and optical performance of devices requires to be addresed.

In summary, research activities in last decade have made remarkable progress, leading to enormous knowledge pool of group-III nitride nanostructures and figuring out of the key challenges. However, the achievements are limited as compared with those of more popular electronic and optoelectronic materials, especially ZnO nanostructures. The outstanding progress, emerging unique properties and potential applications verify that group-III nitride nanostructucures are indeed promising candidates for optoelectronics. We hope that the systematic investigation of a “synthesis-property-application” triangle for group-III nitride nanostructures will inspire more research efforts to settle the current challenges, promote an intense interest to the general study on inorganic semiconducting nanostructures.

Declaration of Competing Interest

The authors declare that they have no competing interest.

Acknowledgements

The present work was supported by the National Natural Science Foundation of China (Grant No 51572092) and the Hong Kong Polytechnic University grant (1-ZVGH).

References

[1] P. Lawaetz, Stability of the wurtzite structure, Physical Review B 5(10) (1972) 4039-4045.

[2] D. Schikora, M. Hankeln, D. As, K. Lischka, T. Litz, A. Waag, T. Buhrow, F. Henneberger, Epitaxial growth and optical transitions of cubic GaN films, Physical Review B 54(12) (1996) R8381-R8384.

[3] J. Schörmann, S. Potthast, D. As, K. Lischka, In situ growth regime characterization of cubic GaN using reflection high energy electron diffraction, Applied Physics Letters 90(4) (2007) 041918.

[4] S. Uehara, T. Masamoto, A. Onodera, M. Ueno, O. Shimomura, K. Takemura, Equation of state of

the rocksalt phase of III–V nitrides to 72 GPa or higher, Journal of Physics and Chemistry of Solids 58(12) (1997) 2093-2099.

[5] J. Wu, When group-III nitrides go infrared: New properties and perspectives, Journal of Applied Physics 106(1) (2009) 011101.

[6] S. Strite, H. Morkoc, GaN, AlN and InN- a review, Journal of Vacuum Science & Technology B 10(4) (1992) 1237-1266.

[7] Y. Taniyasu, M. Kasu, T. Makimoto, An aluminium nitride light-emitting diode with a wavelength of 210 nanometres, Nature 441(7091) (2006) 325-328.

[8] S.D. Hersee, X. Sun, X. Wang, The controlled growth of GaN nanowires, Nano Letters 6(8) (2006) 1808-1811

[9] Y.-L. Chang, Z. Mi, F. Li, Photoluminescence properties of a nearly intrinsic single InN nanowire, Advanced Functional Materials. 20(23) (2010) 4146-4151

[10] A.R. Denton, N.W. Ashcroft, Vegard's law, Physical Review A 43(6) (1991) 3161-3164.

[11] C. Caetano, L. Teles, M. Marques, A. Dal Pino Jr, L. Ferreira, Phase stability, chemical bonds, and gap bowing of InxGa1-xN alloys: comparison between cubic and wurtzite structures, Physical Review B 74(4) (2006) 045215.

[12] P.G. Moses, C.G. Van de Walle, Band bowing and band alignment in InGaN alloys, Applied Physics Letters 96(2) (2010) 021908.

[13] Z. Dridi, B. Bouhafs, P Ruterana, First-principles investigation of lattice constants and bowing parameters in wurtzite $Al_xGa_{1-x}N$, $In_xGa_{1-x}N$ and $In_xAl_{1-x}N$ alloys, Semiconductor Science and Technology 18(9) (2003) 850-856.

[14] R.R. Pelá, C. Caetano, M. Marques, L.G. Ferreira, J. Furthmüller, L.K. Teles, Accurate band gaps of AlGaN, InGaN, and AlInN alloys calculations based on LDA-1/2 approach, Applied Physics Letters 98(15) (2011) 151907.

[15] S. Chattopadhyay, A. Ganguly, K.-H. Chen, L.-C. Chen, One-dimensional group III-nitrides: growth, properties, and applications in nanosensing and nano-optoelectronics, Critical Reviews in Solid State and Materials Sciences 34(3-4) (2009) 224-279.

[16] F. Chen, X. Ji, Z. Lu, Y. Shen, Q. Zhang, Structural and Raman properties of compositionally tunable $Al_xGa_{1-x}N$ ($0.66 \leq x \leq 1$) nanowires, Materials Science and Engineering: B 183 (2014) 24-28.

[17] F. Chen, X. Ji, Z. Lu, Y. Shen, Q. Zhang, Shape-controlled synthesis of one-dimensional $Al_xGa_{1-x}N$ nanotower arrays: structural characteristics and growth mechanism, Journal of Physics D: Applied Physics 47(6) (2014) 065311.

[18] F. Chen, X. Ji, Q. Zhang, Radial AlN nanotips on carbon fibers as flexible electron emitters, Carbon 81 (2015) 124-131.

[19] F. Chen, X. Ji, Q. Zhang, Morphology-controlled synthesis and structural characterization of

ternary $Al_xGa_{1-x}N$ nanostructures by chemical vapor deposition, CrystEngComm 17(6)(2015) 1249-1257.

[20] F. Chen, X. Ji, Q. Zhang, Enhanced field emission properties from AlN nanowires synthesized on conductive graphite substrate, Journal of Alloys and Compounds 646 (2015) 879-884.

[21] T.I. Kamins, R.S. Williams, Y. Chen, Y.L. Chang, Y.A. Chang, Chemical vapor deposition of Si nanowires nucleated by $TiSi_2$ islands on Si, Applied Physics Letters 76(5) (2000) 562-564.

[22] X. Weng, R.A. Burke, J.M. Redwing, The nature of catalyst particles and growth mechanisms of GaN nanowires grown by Ni-assisted metal-organic chemical vapor deposition, Nanotechnology 20(8) (2009) 164-171.

[23] W.C. Hou, L.Y. Chen, W.C. Tang, F.C.N. Hong, Control of seed detachment in Au-assisted GaN nanowire growths, Crystal Growth & Design 11(4) (2011) 990-994.

[24] C. Liu, Z. Hu, Q. Wu, X. Wang, Y. Chen, H. Sang, J. Zhu, S. Deng, N. Xu, Vapor-solid growth and characterization of aluminum nitride nanocones, Journal of the American Chemical Society 127(4) (2005) 1318-1322.

[25] J. Zheng, Y. Yang, B. Yu, X. Song, X. Li, [0001] oriented aluminum nitride one-dimensional nanostructures: Synthesis, structure evolution, and electrical properties, ACS Nano 2(1) (2008) 134-142.

[26] J. Zheng, X. Song, B. Yu, X. Li, Asymmetrical AlN nanopyramids induced by polar surfaces, Applied Physics Letters 90(19) (2007) 193121.

[27] W. Lei, D. Liu, P. Zhu, X. Chen, Q. Zhao, G. Wen, Q. Cui, G. Zou, Ferromagnetic Sc-doped AlN sixfold-symmetrical hierarchical nanostructures, Applied Physics Letters 95(16) (2009) 162501.

[28] S.D. Hersee, X. Sun, X. Wang, The controlled growth of GaN nanowires, Nano Letters 6(8) (2006) 1808-1811.

[29] F. Schuster, M. Hetzl, S. Weiszer, J.A. Garrido, M. de la Mata, C. Magen, J. Arbiol, M. Stutzmann, Position-controlled growth of GaN nanowires and nanotubes on diamond by molecular beam epitaxy, Nano Letters 15(3) (2015) 1773-1779.

[30] H.-D. Xiao, J.-Q. Liu, C.-N. Luan, Z.-W. Ji, J.-S. Cui, Structure and growth mechanism of quasi-aligned GaN layer-built nanotowers, Applied Physics Letters 100(21) (2012) 213101.

[31] Y.-H. Ko, J.-H. Kim, S.-H. Gong, J. Kim, T. Kim, Y.-H. Cho, Red emission of InGaN/GaN double heterostructures on GaN nanopyramid structures, ACS Photonics 2(4) (2015) 515-520.

[32] T. Stoica, R. Meijers, R. Calarco, T. Richter, H. Lüth, MBE growth optimization of InN nanowires, Journal of Crystal Growth 290(1) (2006) 241-247.

[33] P.-C. Wei, L.-C. Chen, K.-H. Chen, Surface diffusion controlled formation of high quality vertically aligned InN nanotubes, Journal of Applied Physics 116(12) (2014) 124301

[34] S. Zhao, B.H. Le, D.P. Liu, X.D. Liu, M.G. Kibria, T. Szkopek, H. Guo, Z. Mi, p-Type InN nanowires, Nano Letters 13(11) (2013) 5509-5513.

[35] P. Wang, Y. Yuan, C. Zhao, X. Wang, X. Zheng, X. Rong, T. Wang, B. Sheng, Q. Wang, Y. Zhang,

L. Bian, X. Yang, F. Xu, Z. Qin, X. Li, X. Zhang, B. Shen, Lattice-polarity-driven epitaxy of hxagonal semiconductor nanowires, Nano Letters 16(2) (2016) 1328-1334.
[36] C. He, Q. Wu, X. Wang, Y. Zhang, L. Yang, N. Liu, Y. Zhao, Y. Lu, Z. Hu, Growth and characterization of ternary AlGaN alloy nanocones across the entire composition range, ACS Nano 5(2) (2011) 1291-1296.
[37] T. Kuykendall, P. Ulrich, S. Aloni, P. Yang, Complete composition tunability of InGaN nanowires using a combinatorial approach, Nature Materials 6(12) (2007) 951-956.
[38] H.M. Kim, Y.H. Cho, H. Lee, S.I. Kim , S.R. Ryu, D.Y. Kim, T.W. Kang , K.S. Chung, High-brightness light emitting diodes using dislocation-free indium gallium nitride/gallium nitride multiquantum-well nanorod arrays, Nano Letters 4(6) (2004) 1059-1062.
[39] Q. Li, K.R. Westlake, M.H. Crawford, S.R. Lee, D.D. Koleske, J.J. Figiel, K.C. Cross, S. Fathololoumi, Z. Mi, G.T. Wang, Optical performance of top-down fabricated InGaN/GaN nanorod light emitting diode arrays, Optics Express 19(25) (2011) 25528-25534.
[40] Y.J. Hwang, C.H. Wu, C. Hahn, H.E. Jeong, P. Yang, Si/InGaN core/shell hierarchical nanowire arrays and their photoelectrochemical properties, Nano Letters 12(3) (2012) 1678-82.
[41] L. Du, Q. Wu, X. Pei, T. Sun, Y. Zhang, L. Yang, X. Wang, Z. Hu, Morphology and composition evolution of one-dimensional InxAl1-xN nanostructures induced by the vapour pressure ratio, CrystEngComm 18(2) (2016) 213-217
[42] J. Kamimura, T. Kouno, S. Ishizawa, A. Kikuchi, K. Kishino, Growth of high-In-content InAlN nanocolumns on Si (111) by RF-plasma-assisted molecular-beam epitaxy, Journal of Crystal Growth 300(1) (2007) 160-163.
[43] H. Li, G. Zhao, S. Kong, D. Han, H. Wei, L. Wang, Z. Chen, S. Yang, Morphology and composition-controlled growth of polar c-axis and nonpolar m-axis well-aligned ternary III-nitride nanotube arrays, Nanoscale 7(39) (2015) 16481-16492.
[44] C.L. Hsiao, R. Magnusson, J. Palisaitis, P. Sandstrom, P.O. Persson, S. Valyukh, L. Hultman, K. Jarrendahl, J. Birch, Curved-lattice epitaxial growth of InxAl1-xN nanospirals with tailored chirality, Nano Letters 15(1) (2015) 294-300.
[45] H. Li, R. Wu, J. Li, Y. Sun, Y. Zheng, J. Jian, Growth of AlN nanobelts, nanorings and branched nanostructures, Journal of Alloys and Compounds 509(5) (2011) 2111-2115.
[46] S.-C. Shi, C.-F. Chen, S. Chattopadhyay, Z.-H. Lan, K.-H. Chen, L.-C. Chen, Growth of single-crystalline wurtzite aluminum nitride nanotips with a self-selective apex angle, Advanced Functional Materials 15(5) (2005) 781-786.
[47] S.-C. Shi, S. Chattopadhyay, C.-F. Chen, K.-H. Chen, L.-C. Chen, Structural evolution of AlN nano-structures: Nanotips and nanorods, Chemical Physics Letters 418(1) (2006) 152-157.
[48] X. Ji, J. Deng, W. Zhou, P. Chen, F. Chen, Field emission properties of AIN nanostructures, Journal of Nanoscience and Nanotechnology 12(8) (2012) 6531-6533.
[49] M. He, I. Minus, P. Zhou, S.N. Mohammed, J.B. Halpern, R. Jacobs, W.L. Sarney, L. Salamanca-Riba, R. Vispute, Growth of large-scale GaN nanowires and tubes by direct reaction of Ga

with NH_3, Applied Physics Letters 77(23) (2000) 3731-3733.
[50] M. He, P. Zhou, S.N. Mohammad, G.L. Harris, J.B. Halpern, R. Jacobs, W.L. Sarney, L. Salamanca-Riba, Growth of GaN nanowires by direct reaction of Ga with NH_3, Journal of Crystal Growth 231(3) (2001) 357-365.
[51] S. Han, W. Jin, T. Tang, C. Li, D. Zhang, X. Liu, J. Han, C. Zhou, Controlled growth of gallium nitride single-crystal nanowires using a chemical vapor deposition method, Journal of Materials Research 18(02) (2003) 245-249.
[52] H. Xu, Z. Liu, X. Zhang, S. Hark, Synthesis and optical properties of InN nanowires and nanotubes, Applied Physics Letters 90(11) (2007) 3105.
[53] G. Xu, Z. Li, J. Baca, J. Wu, Probing nucleation mechanism of self-catalyzed InN nanostructures, Nanoscale Research Letters 5(1) (2009) 7-13.
[54] L. Hong, Z. Liu, X. Zhang, S. Hark, Self-catalytic growth of single-phase AlGaN alloy nanowires by chemical vapor deposition, Applied Physics Letters 89(19) (2006) 193105
[55] S. Keating, M. Urquhart, D. McLaughlin, J. Pearce, Effects of substrate temperature on indium gallium nitride nanocolumn crystal growth, Crystal Growth & Design 11(2) (2010) 565-568.
[56] J.A. Haber, P.C. Gibbons, W.E. Buhro, Morphological control of nanocrystalline aluminum nitride: Aluminum chloride-assisted nanowhisker growth, Journal of the American Chemical Society 119(23) (1997) 5455-5456.
[57] J.A. Haber, P.C. Gibbons, W.E. Buhro, Morphologically selective synthesis of nanocrystalline aluminum nitride, Chemistry of Materials 10(12) (1998) 4062-4071.
[58] X. Ji, Q. Zhang, S. Lau, H. Jiang, J. Lin, Temperature-dependent photoluminescence and electron field emission properties of AlN nanotip arrays, Applied Physics Letters 94(17) (2009) 173106.
[59] X. Ji, Q. Zhang, Z. Ling, S. Lau, Stress and its effect on optical properties of AlN nanorods, Applied Physics Letters 95(23) (2009) 233105.
[60] F. Chen, T. Wang, L. Wang, X. Ji, Q. Zhang, Improved light emission of MoS2 monolayers by constructing AlN/MoS2 core-shell nanowires, Journal of Materials Chemistry C 5(39) (2017) 10225-10230.
[61] Z. Chen, C. Cao, W.S. Li, C. Surya, Well-aligned single-crystalline GaN nanocolumns and their field emission properties, Crystal Growth & Design 9(2) (2008) 792-796.
[62] Z. Chen, C. Cao, H. Zhu, Controlled growth of aluminum nitride nanostructures: aligned tips, brushes, and complex structures, The Journal of Physical Chemistry C 111(5) (2007) 1895-1899.
[63] F. Zhang, Q. Wu, Y. Zhang, J. Zhu, N. Liu, J. Yang, X. Wang, Z. Hu, Chemical vapor deposition growth of InN nanostructures: Morphology regulation and field emission properties, Applied Surface Science 258(24) (2012) 9701-9705.
[64] O. Ambacher, M. Brandt, R. Dimitrov, T. Metzger, M. Stutzmann, R. Fischer, A. Miehr, A. Bergmaier, G. Dollinger, Thermal stability and desorption of group III nitrides prepared by metal organic chemical vapor deposition, Journal of Vacuum Science & Technology B 14(6) (1996) 3532-3542.

[65] F. Chen, T. Wang, X. Ji, $Al_xGa_{1-x}N$-GaN core-shell nanorods: Synthesis and field emission properties, Superlattices and Microstructures 120 (2018) 272-278.
[66] F. Chen, X. Ji, Q. Zhang, Growth and composition-dependent optoelectronic properties of $Al_xGa_{1-x}N$ alloy nanowires arrays across the entire composition range on carbon cloth, Materials Research Express 3(7) (2016) 075011.
[67] T. Kuykendall, P. Pauzauskie, S. Lee, Y. Zhang, J. Goldberger, P. Yang, Metalorganic chemical vapor deposition route to GaN nanowires with triangular cross sections, Nano Letters 3(8) (2003) 1063-1066.
[68] C.G. Tu, C.Y. Su, C.H. Liao, C. Hsieh, Y.F. Yao, H.T. Chen, C.H. Lin, C.M. Weng, Y.W. Kiang, C.C. Yang, Regularly patterned multi-section GaN nanorod arrays grown with a pulsed growth technique, Nanotechnology 27(2) (2016) 025303.
[69] V. Cimalla, C. Foerster, D. Cengher, K. Tonisch, O. Ambacher, Growth of AlN nanowires by metal organic chemical vapour deposition, Physica Status Solidi B 243(7) (2006) 1476-1480.
[70] T.-T. Kang, X. Liu, R.Q. Zhang, W.G. Hu, G. Cong, F.-A. Zhao, Q. Zhu, InN nanoflowers grown by metal organic chemical vapor deposition, Applied Physics Letters 89(7) (2006) 071113.
[71] Y.H. Ra, R. Navamathavan, H.I. Yoo, C.R. Lee, Single nanowire light-emitting diodes using uniaxial and coaxial InGaN/GaN multiple quantum wells synthesized by metalorganic chemical vapor deposition, Nano Letters 14(3) (2014) 1537-1545.
[72] Y. Li, J. Xiang, F. Qian, S. Gradečak, Y. Wu, H. Yan, Dopant-free GaN/AlN/AlGaN radial nanowire heterostructures as high electron mobility transistors, Nano Letters 6(7) (2006) 1468-1473.
[73] J. Su, M. Gherasimova, G. Cui, H. Tsukamoto, J. Han, T. Onuma, M. Kurimoto, S. Chichibu, C. Broadbridge, Y. He, Growth of AlGaN nanowires by metalorganic chemical vapor deposition, Applied Physics Letters 87(18) (2005) 183108.
[74] L.W. Ji, Y.K. Su, S.J. Chang, T.H. Fang, T.C. Wen, S.C. Hung, Growth of ultra small self-assembled InGaN nanotips, Journal of Crystal Growth 263(1-4) (2004) 63-67.
[75] Y. Wang, K. Zang, S. Chua, M.S. Sander, S. Tripathy, C.G. Fonstad, High-density arrays of InGaN nanorings, nanodots, and nanoarrows fabricated by a template-assisted approach, The Journal of Physical Chemistry B 110(23) (2006) 11081-11087.
[76] W.-M. Chang, C.-H. Liao, C.-Y. Chen, C. Hsieh, T.-Y. Tang, Y.-W. Kiang, C.C. Yang, Spiral deposition with alternating indium composition in growing an InGaN nanoneedle with the vapor-liquid-solid growth mode, Journal of Nanomaterials 2012 (2012) 1-7.
[77] J. Song, B. Leung, Y. Zhang, J. Han, Growth, structural and optical properties of ternary InGaN nanorods prepared by selective-area metalorganic chemical vapor deposition, Nanotechnology 25(22) (2014) 225602.
[78] Y.H. Ra, R. Navamathavan, J.H. Park, C.R. Lee, Coaxial $In_xGa_{1-x}N$/GaN multiple quantum well nanowire arrays on Si(111) substrate for high-performance light-emitting diodes, Nano Letters 13(8) (2013) 3506-3516.
[79] S. Iijima, Helical microtubules of graphitic carbon, Nature 354(6348) (1991) 56-58.

[80] K. Hsu, K. Etemadi, E. Pfender, Study of the free-burning high-intensity argon arc, Journal of Applied Physics 54(3) (1983) 1293-1301.

[81] V. Tondare, C. Balasubramanian, S. Shende, D. Joag, V. Godbole, S. Bhoraskar, M. Bhadbhade, Field emission from open ended aluminum nitride nanotubes, Applied Physics Letters 80(25) (2002) 4813-4815.

[82] W. Lei, D. Liu, J. Zhang, B. Liu, P. Zhu, T. Cui, Q. Cui, G. Zou, AlN nanostructures: tunable architectures and optical properties, Chemical Communications (11) (2009) 1365-1367.

[83] W. Lei, D. Liu, J. Zhang, P. Zhu, Q. Cui, G. Zou, Direct synthesis, growth mechanism, and optical properties of 3D AlN nanostructures with urchin shapes, Crystal Growth & Design 9(3) (2009) 1489-1493.

[84] W. Lei, D. Liu, P. Zhu, X. Chen, J. Hao, Q. Wang, Q. Cui, G. Zou, One-step synthesis of AlN branched nanostructures by an improved DC arc discharge plasma method, CrystEngComm 12(2) (2010) 511-516.

[85] L. Shen, X. Li, J. Zhang, Y. Ma, F. Wang, G. Peng, Q. Cui, G. Zou, Synthesis of single-crystalline wurtzite aluminum nitride nanowires by direct arc discharge, Applied Physics A 84(1-2) (2006) 73-75.

[86] W. Han, P. Redlich, F. Ernst, M. Rühle, Synthesis of GaN-carbon composite nanotubes and GaN nanorods by arc discharge in nitrogen atmosphere, Applied Physics Letters 76(5) (2000) 652-654.

[87] A. Cho, J. Arthur, Molecular beam epitaxy, Progress in Solid State Chemistry 10 (1975) 157-191

[88] M. Yoshizawa, A. Kikuchi, M. Mori, N. Fujita, K. Kishino, Growth of self-organized GaN nanostructures on Al_2O_3 (0001) by RF-radical source molecular beam epitaxy, Japanese Journal of Applied Physics 36(4B) (1997) L459.

[89] O. Landré, V. Fellmann, P. Jaffrennou, C. Bougerol, H. Renevier, A. Cros, B. Daudin, Molecular beam epitaxy growth and optical properties of AlN nanowires, Applied Physics Letters 96(6) (2010) 061912.

[90] V. Consonni, M. Hanke, M. Knelangen, L. Geelhaar, A. Trampert, H. Riechert, Nucleation mechanisms of self-induced GaN nanowires grown on an amorphous interlayer, Physical Review B 83(3) (2011) 035310.

[91] A.P. Vajpeyi, A.O. Ajagunna, K. Tsagaraki, M. Androulidaki, A. Georgakilas, InGaN nanopillars grown on silicon substrate using plasma assisted molecular beam epitaxy, Nanotechnology 20(32) (2009) 325605.

[92] W. Guo, M. Zhang, A. Banerjee, P. Bhattacharya, Catalyst-free InGaN/GaN nanowire light emitting diodes grown on (001) silicon by molecular beam epitaxy, Nano Letters 10(9) (2010)

3355-3359.
[93] A. Pierret, C. Bougerol, S. Murcia-Mascaros, A. Cros, H. Renevier, B. Gayral, B. Daudin, Growth, structural and optical properties of AlGaN nanowires in the whole composition range, Nanotechnology 24(11) (2013) 115704.
[94] M. Tangi, P. Mishra, B. Janjua, T.K. Ng, D.H. Anjum, A. Prabaswara, Y. Yang, A.M. Albadri, A.Y. Alyamani, M.M. El-Desouki, B.S. Ooi, Bandgap measurements and the peculiar splitting of E2H phonon modes of $In_xAl_{1-x}N$ nanowires grown by plasma assisted molecular beam epitaxy, Journal of Applied Physics 120(4) (2016) 045701.
[95] S. Zhao, M.G. Kibria, Q. Wang, H.P. Nguyen, Z. Mi, Growth of large-scale vertically aligned GaN nanowires and their heterostructures with high uniformity on SiO_x by catalyst-free molecular beam epitaxy, Nanoscale 5(12) (2013) 5283-5287.
[96] T. Schumann, T. Gotschke, F. Limbach, T. Stoica, R. Calarco, Selective-area catalyst-free MBE growth of GaN nanowires using a patterned oxide layer, Nanotechnology 22(9) (2011) 095603.
[97] S. Albert, A. Bengoechea-Encabo, P. Lefebvre, F. Barbagini, M.A. Sanchez-Garcia, E. Calleja, U. Jahn, A. Trampert, Selective area growth and characterization of InGaN nano-disks implemented in GaN nanocolumns with different top morphologies, Applied Physics Letters 100(23) (2012) 231906.
[98] Ž. Gačević, D. Gomez Sanchez, E. Calleja, Formation mechanisms of GaN nanowires grown by selective area growth homoepitaxy, Nano Letters 15(2) (2015) 1117-1121.
[99] K.A. Bertness, A.W. Sanders, D.M. Rourke, T.E. Harvey, A. Roshko, J.B. Schlager, N.A. Sanford, Controlled nucleation of GaN nanowires grown with molecular beam epitaxy, Advanced Functional Materials 20(17) (2010) 2911-2915.
[100] Y.L. Chang, J.L. Wang, F. Li, Z. Mi, High efficiency green, yellow, and amber emission from InGaN/GaN dot-in-a-wire heterostructures on Si(111), Applied Physics Letters 96(1) (2010) 013106.
[101] H.P. Nguyen, S. Zhang, K. Cui, X. Han, S. Fathololoumi, M. Couillard, G.A. Botton, Z. Mi, p-Type modulation doped InGaN/GaN dot-in-a-wire white-light-emitting diodes monolithically grown on Si(111), Nano Letters 11(5) (2011) 1919-1924.
[102] H.P.T. Nguyen, K. Cui, S. Zhang, S. Fathololoumi, Z. Mi, Full-color InGaN/GaN dot-in-a-wire light emitting diodes on silicon, Nanotechnology 22(44) (2011) 445202.
[103] H.P.T. Nguyen, S. Zhang, K. Cui, A. Korinek, G.A. Botton, Z. Mi, High-efficiency InGaN/GaN dot-in-a-wire red light-emitting diodes, IEEE Photonics Technology Letters 24(4) (2012) 321-323.
[104] G. Tourbot, C. Bougerol, A. Grenier, M. Den Hertog, D. Sam-Giao, D. Cooper, P. Gilet, B. Gayral, B. Daudin, Structural and optical properties of InGaN/GaN nanowire heterostructures grown by PA-MBE, Nanotechnology 22(7) (2011) 075601.
[105] K. Hestroffer, R. Mata, D. Camacho, C. Leclere, G. Tourbot, Y.M. Niquet, A. Cros, C. Bougerol,

H. Renevier, B. Daudin, The structural properties of GaN/AlN core-shell nanocolumn heterostructures, Nanotechnology 21(41) (2010) 415702.
[106] L. Rigutti, G. Jacopin, L. Largeau, E. Galopin, A. De Luna Bugallo, F.H. Julien, J.C. Harmand, F. Glas, M. Tchernycheva, Correlation of optical and structural properties of GaN/AlN core-shell nanowires, Physical Review B 83(15) (2011) 155320.
[107] S.D. Carnevale, C. Marginean, P.J. Phillips, T.F. Kent, A.T.M.G. Sarwar, M.J. Mills, R.C. Myers, Coaxial nanowire resonant tunneling diodes from non-polar AlN/GaN on silicon, Applied Physics Letters 100(14) (2012) 142115.
[108] R.F. Allah, T. Ben, R. Songmuang, D. González, Imaging and analysis by transmission electron microscopy of the spontaneous formation of Al-rich shell structure in AlxGa1-xN/GaN nanowires, Applied Physics Express 5(4) (2012) 045002.
[109] K. Cui, S. Fathololoumi, M. Golam Kibria, G.A. Botton, Z. Mi, Molecular beam epitaxial growth and characterization of catalyst-free InN/InxGa1-xN core/shell nanowire heterostructures on Si(111) substrates, Nanotechnology 23(8) (2012) 085205.
[110] H.P. Nguyen, M. Djavid, S.Y. Woo, X. Liu, A.T. Connie, S. Sadaf, Q. Wang, G.A. Botton, I. Shih, Z. Mi, Engineering the carrier dynamics of InGaN nanowire white light-emitting diodes by distributed p-AlGaN electron blocking layers, Scientific Reports 5 (2015) 7744.
[111] J. Liu, X. Zhang, Y. Zhang, R. He, J. Zhu, Novel synthesis of AlN nanowires with controlled diameters, Journal of Materials Research 16(11) (2001) 3133-3138.
[112] L.W. Yin, Y. Bando, Y.C. Zhu, M.S. Li, C.-C. Tang, D. Golberg, Single-crystalline AlN nanotubes with carbon-layer coatings on the outer and inner surfaces via a multiwalled-carbon-nanotube template-induced route, Advanced Materials 17(2) (2005) 213-217.
[113] Y. Zhang, J. Liu, R. He, Q. Zhang, X. Zhang, J. Zhu, Synthesis of aluminum nitride nanowires from carbon nanotubes, Chemistry of Materials 13(11) (2001) 3899-3905.
[114] Q. Wu, Z. Hu, X. Wang, Y. Hu, Y. Tian, Y. Chen, A simple route to aligned AlN nanowires, Diamond and Related Materials 13(1) (2004) 38-41.
[115] J. Zhang, X. Peng, X. Wang, Y. Wang, L. Zhang, Micro-Raman investigation of GaN nanowires prepared by direct reaction Ga with NH3, Chemical Physics Letters 345(5) (2001) 372-376.
[116] N. Liu, Q. Wu, C. He, H. Tao, X. Wang, W. Lei, Z. Hu, Patterned growth and field-emission properties of AlN nanocones, ACS Applied Materials & Interfaces 1(9) (2009) 1927-1930.
[117] C. Ji, S. Jiang, Y. Zhang, H. Xing, Z. Yang, C. Wang, T. Yu, G. Zhang, GaN nanorod array as a precursor to enhance GaN: Mn ferromagnetism, RSC Advances 5(118) (2015) 97408-97412.
[118] L.W. Yin, Y. Bando, D. Golberg, M.S. Li, Growth of single-crystal indium nitride nanotubes and nanowires by a controlled-carbonitridation reaction route, Advanced Materials 16(20) (2004) 1833-1838
[119] W. Han, S. Fan, Q. Li, Y. Hu, Synthesis of gallium nitride nanorods through a carbon nanotube-confined reaction, Science 277(5330) (1997) 1287-1289
[120] X. Xu, X. Fang, H. Zeng, T. Zhai, Y. Bando, D. Golberg, One-dimensional nanostructures in

porous anodic alumina membranes, Science of Advanced Materials 2(3) (2010) 273-294.
[121] L. Zhao, W. Yang, Y. Luo, T. Zhai, G. Zhang, J. Yao, Nanotubes from isomeric dibenzoylmethane molecules, Chemistry–A European Journal 11(12) (2005) 3773-3778.
[122] J. Zhang, B. Xu, F. Jiang, Y. Yang, J. Li, Fabrication of ordered InN nanowire arrays and their photoluminescence properties, Physics Letters A 337(1) (2005) 121-126.
[123] G. Selvaduray, L. Sheet, Aluminium nitride: review of synthesis methods, Materials Science and Technology 9(6) (1993) 463-473.
[124] S. Chattopadhyay, S.C. Shi, Z.H. Lan, C.F. Chen, K.-H. Chen, L.-C. Chen, Molecular sensing with ultrafine silver crystals on hexagonal aluminum nitride nanorod templates, Journal of the American Chemical Society 127(9) (2005) 2820-2821.
[125] S.-C. Shi, C.F. Chen, S. Chattopadhyay, K.-H. Chen, B.-W. Ke, L.-C. Chen, L. Trinkler, B. Berzina, Luminescence properties of wurtzite AlN nanotips, Applied Physics Letters 89(16) (2006) 163127.
[126] Y. Gao, M. Hu, X. Chu, Q. Yan, Morphology evolution, growth mechanism and optical properties of AlN nanostructures, Journal of Materials Science: Materials in Electronics 24(10) (2013) 4008-4013.
[127] L. Yu, Z. Hu, Y. Ma, K. Huo, Y. Chen, H. Sang, W. Lin, Y. Lu, Evolution of aluminum nitride nanostructures from nanoflower to thin film on silicon substrate by direct nitridation of aluminum precursor, Diamond and Related Materials 16(8) (2007) 1636-1642.
[128] B. Liu, Y. Bando, C. Tang, F. Xu, D. Golberg, Quasi-aligned single-crystalline GaN nanowire arrays, Applied Physics Letters 87(7) (2005) 073106.
[129] B. Liu, Y. Bando, C. Tang, F. Xu, J. Hu, D. Golberg, Needlelike bicrystalline GaN nanowires with excellent field emission properties, The Journal of Physical Chemistry B 109(36) (2005) 17082-17085.
[130] Z. Ma, D. McDowell, E. Panaitescu, A.V. Davydov, M. Upmanyu, L. Menon, Vapor-liquid-solid growth of serrated GaN nanowires: shape selection driven by kinetic frustration, Journal of Materials Chemistry C 1(44) (2013) 7294-7302.
[131] Y. Tang, Z. Chen, H. Song, C. Lee, H. Cong, H. Cheng, W. Zhang, I. Bello, S. Lee, Vertically aligned p-type single-crystalline GaN nanorod arrays on n-type Si for heterojunction photovoltaic cells, Nano Letters 8(12) (2008) 4191-4195.
[132] C. Blomers, J.G. Lu, L. Huang, C. Witte, D. Grutzmacher, H. Luth, T. Schapers, Electronic transport with dielectric confinement in degenerate InN nanowires, Nano Letters 12(6) (2012) 2768-2772.
[133] G. Koley, Z. Cai, E.B. Quddus, J. Liu, M. Qazi, R.A. Webb, Growth direction modulation and diameter-dependent mobility in InN nanowires, Nanotechnology 22(29) (2011) 295701.
[134] E.B. Quddus, A. Wilson, R.A. Webb, G. Koley, Oxygen mediated synthesis of high quality InN nanowires above their decomposition temperature, Nanoscale 6(2) (2014) 1166-1172.
[135] T. Tang, S. Han, W. Jin, X. Liu, C. Li, D. Zhang, C. Zhou, B. Chen, J. Han, M. Meyyapan, Synthesis and characterization of single-crystal indium, Journal of Materials Research. 19(2) (2003)

423-426.

[136] X. Ji, S. Cheng, H. Hu, H. Li, Z. Wu, P. Yan, Effect of catalyst nanoparticle size on growth direction and morphology of InN nanowires, AIP Advances 2(2) (2012) 022150.

[137] S. Sahoo, M.S. Hu, C.W. Hsu, C.T. Wu, K.H. Chen, L.C. Chen, A.K. Arora, S. Dhara, Surface optical Raman modes in InN nanostructures, Applied Physics Letters 93(23) (2008) 233116.

[138] H. Liu, L. Shi, X. Geng, R. Su, G. Cheng, S. Xie, Reactant-governing growth direction of indium nitride nanowires, Nanotechnology 21(24) (2010) 245601.

[139] X. Chen, H. Liu, Q. Li, H. Chen, R. Peng, S. Chu, B. Cheng, Terahertz detectors arrays based on orderly aligned InN nanowires, Scitific Reports 5 (2015) 13199.

[140] S. Rafique, L. Han, H. Zhao, Chemical vapor deposition of m-plane and c-plane InN nanowires on Si (100) substrate, Journal of Crystal Growth 415 (2015) 78-83.

[141] V. Parameshwaran, X. Xu, B.M. Clemens, Crystallinity, surface morphology, and photoelectrochemical effects in conical InP and InN nanowires grown on silicon, ACS Applied Materials & Interfaces 8(33)(2016)21454-21464.

[142] A.K. Sivadasan, K.K. Madapu, S. Dhara, Light-matter interaction of single semiconducting AlGaN nanowire and noble metal Au nanoparticle in the sub-diffraction limit, Physical Chemistry Chemical Physics 18(34)(2016)23680-23685.

[143] A.K. Sivadasan, A. Patsha, S. Dhara, Optically confined polarized resonance Raman studies in identifying crystalline orientation of sub-diffraction limited AlGaN nanostructure, Applied Physics Letters 106(17) (2015) 173107.

[144] X.M. Cai, F. Ye, S.Y. Jing, D.P. Zhang, P. Fan, E.Q. Xie, CVD growth of InGaN nanowires, Journal of Alloys and Compounds 467(1-2) (2009) 472-476.

[145] C.-W. Hsu, A. Ganguly, C.-H. Liang, Y.-T. Hung, C.-T. Wu, G.-M. Hsu, Y.-F. Chen, C.-C. Chen, K.-H. Chen, L.-C. Chen, Enhanced emission of (In, Ga) nitride nanowires embedded with self-assembled quantum dots, Advanced Functional Materials 18(6) (2008) 938-942.

[146] W.-C. Tang, F.C.-N. Hong, Growths of indium gallium nitride nanowires by plasma-assisted chemical vapor deposition, Thin Solid Films 570 (2014) 315-320.

[147] F. Ye, X.M. Cai, X.M. Wang, E.Q. Xie, The growth and field electron emission of InGaN nanowires, Journal of Crystal Growth 304(2) (2007) 333-337.

[148] X.M. Cai, Y.H. Leung, K.Y. Cheung, K.H. Tam, A.B. Djurišić, M.H. Xie, H.Y. Chen, S. Gwo, Straight and helical InGaN core-shell nanowires with a high In core content, Nanotechnology 17(9) (2006) 2330-2333.

[149] Q. Wu, F. Zhang, X. Wang, C. Liu, Z. Hu, Y. Lu, Preparation and characterization of AlN-based hierarchical nanostructures with improved chemical stability, The Journal of Physical Chemistry C 111(34) (2007) 12639-12642.

[150] J.H. He, R.S. Yang, C.Y. L., C.L. J., L.J. Chen, Z.L. Wang, Aligned AlN Nanorods with multi-tipped surfaces-Growth, field-emission, and cathodoluminescence properties, Advanced Materials 18(5) (2006) 650-654.

[151] J.C. Johnson, H.-J. Choi, K.P. Knutsen, R.D. Schaller, P. Yang, R.J. Saykally, Single gallium

nitride nanowire lasers, Nature Materials 1(2) (2002) 106-110.
[152] B. Xu, D. Yang, F. Wang, J. Liang, S. Ma, X. Liu, Synthesis of large-scale GaN nanobelts by chemical vapor deposition, Applied Physics Letters 89(7) (2006) 074106.
[153] X. Cai, A. Djurisic, M. Xie, C. Chiu, S. Gwo, Growth mechanism of stacked-cone and smooth-surface GaN nanowires, Applied Physics Letters 87(18) (2005) 183103.
[154] H.K. Seong, Y. Lee, J.Y. Kim, Y.K. Byeun, K.S. Han, J.G. Park, H.J. Choi, Single-crystalline AlGaN: Mn nanotubes and their magnetism, Advanced Materials 18(22) (2006) 3019-3023.
[155] X. Wang, J. Song, F. Zhang, C. He, Z. Hu, Z. Wang, Electricity generation based on one-dimensional group-III nitride nanomaterials, Advanced Materials 22(19) (2010) 2155-2158.
[156] Z.J. Li, X.L. Chen, H.J. Li, Q.Y. Tu, Z. Yang, Y.P. Xu, B.Q. Hu, Synthesis and Raman scattering of GaN nanorings, nanoribbons and nanowires, Applied physics A: Materials Science & Processing 72(5) (2001) 629-632.
[157] E. Li, S. Song, D. Ma, N. Fu, Y. Zhang, Synthesis and field emission properties of helical GaN nanowires, Journal of Electronic Materials 43(5) (2014) 1379-1383.
[158] H.W. Seo, S.Y. Bae, J. Park, H. Yang, K.S. Park, S. Kim, Strained gallium nitride nanowires, Journal of Chemical Physics 116(21) (2002) 9492-9499.
[159] Y. Tang, H. Cong, Z. Wang, H. Cheng, Catalyst-seeded synthesis and field emission properties of flowerlike Si-doped AlN nanoneedle array, Applied Physics Letters 89(25) (2006) 253112.
[160] H. Cui, Y. Sun, C. Wang, Unusual growth direction and controllable wettability of W-catalyzed AlN nanowires, CrystEngComm 15(26) (2013) 5376-5381.
[161] C.Y. Nam, Jaroenapibal, P., Tham, D., Luzzi, D. E., Evoy, S., Fischer, J. E, Diameter-dependent electromechanical properties of GaN nanowires, Nano Letters 6(2) (2006) 153-158.
[162] D. Tham, C.Y. Nam, J.E. Fischer, Defects in GaN nanowires, Advanced Functional Materials 16(9) (2006) 1197-1202.
[163] Y.H. Park, R. Ha, T.E. Park, S.W. Kim, D. Seo, H.J. Choi, Magnetic InxGa1-xN nanowires at room temperature using Cu dopant and annealing, Nanoscale Research Letters 10(1) (2015) 2501.
[164] T. Kuykendall, P.J. Pauzauskie, Y. Zhang, J. Goldberger, D. Sirbuly, J. Denlinger, P. Yang, Crystallographic alignment of high-density gallium nitride nanowire arrays, Nature Materials 3(8) (2004) 524-528.
[165] C.C. Chen, C.C. Yeh, C.H. Chen, M.Y. Yu, H.L. Liu, J.J. Wu, K.H. Chen, L.C. Chen, J.Y. Peng, Y.F. Chen, Catalytic growth and characterization of gallium nitride nanowires, Journal of the American Chemical Society 123(12) (2001) 2791-2798.
[166] F. Liu, Z. Su, F. Mo, L. Li, Z. Chen, Q. Liu, J. Chen, S. Deng, N. Xu, Controlled synthesis of ultra-long AlN nanowires in different densities and in situ investigation of the physical properties of an individual AlN nanowire, Nanoscale 3(2) (2011) 610-618.
[167] H. Chen, X. Wu, X. Xiong, W. Zhang, L. Xu, J. Zhu, P.K. Chu, Formation mechanism and photoluminescence of AlN nanowhiskers, Journal of Physics D: Applied Physics 41(2) (2007) 025101.
[168] Y. Tang, H. Cong, Z. Wang, H.-M. Cheng, Synthesis of rectangular cross-section AlN nanofibers

by chemical vapor deposition, Chemical Physics Letters 416(1) (2005) 171-175.
[169] Y. Tang, H. Cong, Z. Chen, H. Cheng, An array of Eiffel-tower-shape AlN nanotips and its field emission properties, Applied Physics Letters 86(23) (2005) 233104.
[170] F. Liu, Z. Su, W. Liang, F. Mo, L. Li, S. Deng, J. Chen, N. Xu, Controlled growth and field emission of vertically aligned AlN nanostructures with different morphologies, Chinese Physics B 18(5) (2009) 2016-2023.
[171] S.Y. Bae, H.W. Seo, J. Park, H. Yang, J.C. Park, S.Y. Lee, Single-crystalline gallium nitride nanobelts, Applied Physics Letters 81(1) (2002) 126.
[172] H. Wang, G. Liu, W. Yang, L. Lin, Z. Xie, J. Fang, L. An, Bicrystal AlN zigzag nanowires, The Journal of Physical Chemistry C 111(46) (2007) 17169-17172.
[173] H. Wang, Z. Xie, Y. Wang, W. Yang, Q. Zeng, F. Xing, L. An, Single-crystal AlN nanonecklaces, Nanotechnology 20(2) (2009) 025611.
[174] X. Chen, J. Li, Y. Cao, Y. Lan, H. Li, M. He, C. Wang, Z. Zhang, Z. Qiao, Straight and smooth GaN nanowires, Advanced Materials 12(19) (2000) 1432-1434.
[175] Q. Wu, Z. Hu, X. Wang, Y. Chen, Y. Lu, Synthesis and optical characterization of aluminum nitride nanobelts, The journal of Physical Chemistry B 107(36) (2003) 9726-9729.
[176] M. Sun, X. Wu, C. He, P.K. Chu, Controllable growth of hierarchical AlN nanostructures based on dynamic equilibrium, CrystEngComm 13(21) (2011) 6337-6341.
[177] X. Wei, F. Shi, Synthesis and characterization of GaN nanowires by a catalyst assisted chemical vapor deposition, Applied Surface Science 257(23) (2011) 9931-9934.
[178] H. Yang, S. Yu, Y. Hui, S. Lau, Electroluminescence from AlN nanowires grown on p-SiC substrate, Applied Physics Letters 97(19) (2010) 191105.
[179] S.C. Lyu, O.H. Cha, E.K. Suh, H. Ruh, H.J. Lee, C.J. Lee, Catalytic synthesis and photoluminescence of gallium nitride nanowires, Chemical Physics Letters 367(1–2) (2003) 136-140.
[180] Q. Wu, Z. Hu, X. Wang, Y. Lu, K. Huo, S. Deng, N. Xu, B. Shen, R. Zhang, Y. Chen, Extended vapor-liquid-solid growth and field emission properties of aluminium nitride nanowires, Journal of Materials Chemistry 13(8) (2003) 2024-2027.
[181] C.-Y. Chang, G.-C. Chi, W.-M. Wang, L.-C. Chen, K.-H. Chen, F. Ren, S. Pearton, Transport properties of InN nanowires, Applied Physics Letters 87(9) (2005) 093112.
[182] T. Tang, S. Han, Wu Jin, X. Liu, C. Li, D. Zhang, C. Zhou, B. Chen, J. Han, M. Meyyapan, Synthesis and characterization of single-crystal indium nitride nanowires, Journal of Materials Research 19(2) (2004) 423-426.
[183] H. Harima, Properties of GaN and related compounds studied by means of Raman scattering, Journal of Physics: Condensed Matter 14 (2002) R967-R993.
[184] Y. Tian, Y. Jia, Y. Bao, Y. Chen, Macro-quantity synthesis of AlN nanowires via combined technique of arc plasma jet and thermal treatment, Diamond and Related Materials 16(2) (2007) 302-305.
[185] G. S. Cheng, B. Zhang, Y. Zhu, G. T. Fei, L. Li, C. Mo, Y. Mao, Large-scale synthesis of single crystalline gallium nitride nanowires, Applied Physics Letters 75(16) (1999) 2455-2457.

[186] M. Tangi, P. Mishra, B. Janjua, T.K. Ng, D.H. Anjum, A. Prabaswara, Y. Yang, A.M. Albadri, A.Y. Alyamani, M.M. Eldesouki, Bandgap measurements and the peculiar splitting of E2H phonon modes of $In_xAl_{1-x}N$ nanowires grown by plasma assisted molecular beam epitaxy, Journal of Applied Physics 120(4) (2016) 4535.
[187] V.Y. Davydov, I. Goncharuk, A. Smirnov, A. Nikolaev, W. Lundin, A. Usikov, A. Klochikhin, J. Aderhold, J. Graul, O. Semchinova, Composition dependence of optical phonon energies and Raman line broadening in hexagonal $Al_xGa_{1-x}N$ alloys, Physical Review B 65(12) (2002) 125203.
[188] D.G. Zhao, S.J. Xu, M.H. Xie, S.Y. Tong, H. Yang, Stress and its effect on optical properties of GaN epilayers grown on Si(111), 6H-SiC(0001), and c-plane sapphire, Applied Physics Letters 83(4) (2003) 677-679.
[189] M. Kazan, C. Zgheib, E. Moussaed, P. Masri, Temperature dependence of Raman-active modes in AlN, Diamond & Related Materials 15(4–8) (2006) 1169-1174.
[190] J.M. Hayes, M. Kuball, Y. Shi, J.H. Edgar, Temperature dependence of the phonons of bulk AlN, Japanese Journal of Applied Physics 39(39) (2000) L710-L712.
[191] L.D. Yao, S.D. Luo, X. Shen, S.J. You, L.X. Yang, et al., Structural stability and Raman scattering of InN nanowires under high pressure, Journal of Materials Research 25(12) (2010) 2330-2335.
[192] K.K. Madapu, S. Dhara, S. Polaki, S. Amirthapandian, A.K. Tyagi, Growth of InN quantum dots to nanorods: A competition between nucleation and growth rates, CrystEngComm 17(16) (2015) 135-141.
[193] X. Ji, S. Lau, S. Yu, H. Yang, T. Herng, J. Chen, Ferromagnetic Cu-doped AlN nanorods, Nanotechnology 18(10) (2007) 105601.
[194] A.A. Guda, S.P. Lau, M.A. Soldatov, N.Y. Smolentsev, V.L. Mazalova, X.H. Ji, A.V. Soldatov, Copper defects inside AlN:Cu nanorods-XANES and LAPW study, Journal of Physics: Conference Series 190(1) (2009) 012136.
[195] L.B. Jiang, Y. Liu, S.B. Zuo, W.J. Wang, Room-temperature ferromagnetism with high magnetic moment in Cu-doped AlN single crystal whiskers, Chinese Physics B 24(2) (2015) 414-418.
[196] Z. Fang, E. Robin, E. Rozas-Jiménez, A. Cros, F. Donatini, N. Mollard, J. Pernot, B. Daudin, Si Donor incorporation in GaN nanowires, Nano Letters 15(10) (2015) 6794-6801.
[197] W. Miao, Electrogenerated chemiluminescence and its biorelated applications, Chemical Reviews 108(7) (2008) 2506-2553.
[198] D. C. Yu, Q. Y. Zhang, A. Meijerink, Multi-photon quantum cutting in Gd_2O_2S: Tm^{3+} to enhance the photo-response of solar cells, Light: Science & Application, 4(2015) e344.
[199] Z. H. Jiang, Q. Y. Zhang, The structure of glass: a phase equilibrium diagram approach, Progress in Materials Science, 61(2014)144-215.
[200] Q. Y. Zhang, L. L. Hu, Z. H. Jiang, Thermodynamic study on elimination of platinum inclusions in phosphate laser glasses for inertial confinement fusion applications, Chinese Science Bulletin, 44(1999)664-668.

[201] O. Landré, V. Fellmann, P. Jaffrennou, C. Bougerol, H. Renevier, B. Daudin, Growth mechanism of catalyst-free [0001] GaN and AlN nanowires on Si by molecular beam epitaxy, Physica Status Solidi C- Current Topics in Solid State Physics 7(7-8) (2010) 2246–2248.

[202] H.W. Kim, M.A. Kebede, H.S. Kim, Temperature-controlled growth and photoluminescence of AlN nanowires, Applied Surface Science 255(16) (2009) 7221-7225.

[203] L. Yu, N. Liu, C. He, Q. Wu, Z. Hu, In-situ chloride-generated route to different AlN nanostructures on Si substrate, The Journal of Physical Chemistry C 113(32) (2009) 14245-14248.

[204] H.T. Chen, X.L. Wu, X. Xiong, W.C. Zhang, L.L. Xu, J. Zhu, P.K. Chu, Formation mechanism and photoluminescence of AlN nanowhiskers, Journal of Physics D Applied Physics 41(2) (2008) 369-374.

[205] C. Xu, J. Chun, B. Chon, T. Joo, D.E. Kim, In situ fabrication and blueshifted red emission of GaN:Eu nanoneedles, Nanotechnology 18(1) (2007) 015703.

[206] F. Liu, L.F. Li, T.Y. Guo, H.B. Gan, X.S. Mo, J. Chen, S.Z. Deng, N.S. Xu, Investigation on the photoconductive behaviors of an individual AlN nanowire under different excited lights, Nanoscale Research Letters 7(1) (2012) 1-5.

[207] F. Zhang, Q. Wu, X. Wang, N. Liu, J. Yang, Y. Hu, L. Yu, X. Wang, Z. Hu, J. Zhu, 6-fold-symmetrical AlN hierarchical nanostructures: synthesis and field-emission properties, Journal of Physical Chemistry C 113(10) (2009) 4053-4058.

[208] A. Aghdaie, H. Haratizadeh, S.H. Mousavi, S.A.J. Mohammadi, P.W.D. Oliveira, Effect of doping on structural and luminescence properties of AlN nanowires, Ceramics International 41(2) (2015) 2917-2922.

[209] L. Shen, T. Cheng, L. Wu, X. Li, Q. Cui, Synthesis and optical properties of aluminum nitride nanowires prepared by arc discharge method, Journal of Alloys and Compounds 465(1) (2008) 562-566.

[210] Y. Tang, H. Cong, F. Li, H.-M. Cheng, Synthesis and photoluminescent property of AlN nanobelt array, Diamond and Related Materials 16(3) (2007) 537-541.

[211] L. Jin, H. Zhang, R. Pan, P. Xu, J. Han, X. Zhang, Q. Yuan, Z. Zhang, X. Wang, Y. Wang, Observation of the long afterglow in AlN helices, Nano Letters 15(10) (2015) 6575-6581.

[212] H. Li, X. Ji, Z. Wu, H. Hu, D. Yan, R. Zhuo, J. Feng, B. Geng, P. Yan, Structure and optical investigation of faceted hexagonal aluminum nitride nanotube arrays, Applied Physics Express 7(6) (2014) 297-302.

[213] M. Lei, B. Song, X. Guo, Y.F. Guo, P.G. Li, W.H. Tang, Large-scale AlN nanowires synthesized by direct sublimation method, Journal of the European Ceramic Society 29(1) (2009) 195-200.

[214] J.K. Zettler, P. Corfdir, C. Hauswald, E. Luna, U. Jahn, T. Flissikowski, E. Schmidt, C. Ronning, A. Trampert, L. Geelhaar, Observation of dielectrically confined excitons in ultrathin GaN nanowires up to room temperature, Nano Letters 16(2) (2015)973-980.

[215] N.P. Reddy, S. Naureen, S. Mokkapati, K. Vora, N. Shahid, F. Karouta, H.H. Tan, C. Jagadish, Enhanced luminescence from GaN nanopillar arrays fabricated using a top-down process,

Nanotechnology 27(6) (2016) 065304.
[216] S.D. Hersee, A. Xinyu Sun, X. Wang, The controlled growth of GaN nanowires, Nano Letters 6(8) (2006) 1808-1811.
[217] V. Kumaresan, L. Largeau, A. Madouri, F. Glas, H. Zhang, F. Oehler, A. Cavanna, A. Babichev, L. Travers, N. Gogneau, Epitaxy of GaN nanowires on graphene, 16(8)(2016)4895-4902.
[218] Y.Q. Wang, R.Z. Wang, Y.J. Li, Y.F. Zhang, M.K. Zhu, B.B. Wang, H. Yan, From powder to nanowire: A simple and environmentally friendly strategy for optical and electrical GaN nanowire films, CrystEngComm 15(8) (2013) 1626-1634.
[219] H.-M. Kim, D.S. Kim, Y.S. Park, D.Y. Kim, T.W. Kang, K.S. Chung, Growth of GaN nanorods by a hydride vapor phase epitaxy method, Advanced Materials 14(13-14) (2002) 991-993.
[220] P. Uthirakumar, N. Han, S.H. Woo, E.K. Suh, C.H. Hong, Synthesis and optical properties of sword-like GaN nanorods clusters, Current Applied Physics 9(1) (2009) S114–S117.
[221] Y.L. Chang, Z. Mi, F. Li, Photoluminescence properties of a nearly intrinsic single InN nanowire, Advanced Functional Materials 20(20) (2010) 4146-4151.
[222] P.C. Wei, L.C. Chen, K.H. Chen, Surface diffusion controlled formation of high quality vertically aligned InN nanotubes, Journal of Applied Physics 116(12) (2014) 124301.
[223] M.A. Sánchez-García, J. Gral, E. Calleja, S. Lazic, J.M. Calleja, A. Trampert, Epitaxial growth and characterization of InN nanorods and compact layers on silicon substrates, Physica Status Solidi B-Basic Solid State Physics 243(7) (2010) 1490-1493.
[224] Z.H. Lan, W.M. Wang, C.L. Sun, S.C. Shi, C.W. Hsu, T.T. Chen, K.H. Chen, C.C. Chen, Y.F. Chen, L.C. Chen, Growth mechanism, structure and IR photoluminescence studies of indium nitride nanorods, Journal of Crystal Growth 269(1) (2004) 87–94.
[225] M.S. Hu, W.M. Wang, T.T. Chen, L.S. Hong, C.W. Chen, C.C. Chen, Y.F. Chen, K.H. Chen, L.C. Chen, Sharp infrared emission from single-crystalline indium nitride nanobelts prepared using guided-stream thermal chemical vapor deposition, Advanced Functional Materials 16(4) (2006) 537-541.
[226] M.S. Hu, G.M. Hsu, K.H. Chen, C.J. Yu, H.C. Hsu, L.C. Chen, J.S. Hwang, L.S. Hong, Y.F. Chen, Infrared lasing in InN nanobelts, Applied Physics Letters 90(12) (2007) 123109.
[227] C. Liang, L. Chen, J. Hwang, K. Chen, Y. Hung, Y. Chen, Selective-area growth of indium nitride nanowires on gold-patterned Si (100) substrates, Applied Physics Letters 81(1) (2002) 22-24.
[228] T. Tang, S. Han, W. Jin, X. Liu, C. Li, D. Zhang, C. Zhou, B. Chen, J. Han, M. Meyyapan, Synthesis and characterization of single-crystal indium nitride nanowires, Journal of Materials Research 19(2) (2004) 423-426.
[229] S. Luo, W. Zhou, Z. Zhang, L. Liu, X. Dou, J. Wang, X. Zhao, D. Liu, Y. Gao, L. Song, Synthesis of long indium nitride nanowires with uniform diameters in large quantities, Small 1(10) (2005) 1004–1009.
[230] R.S. Chen, T.H. Yang, H.Y. Chen, L.C. Chen, K.H. Chen, Y.J. Yang, C.H. Su, C.R. Lin, High-gain photoconductivity in semiconducting InN nanowires, Applied Physics Letters 95(16) (2009)

162112.

[231] J. Zhang, B. Xu, F. Jiang, Y. Yang, J. Li, Fabrication of ordered InN nanowire arrays and their photoluminescence properties, Physics Letters A 337(1-2) (2005) 121-126.

[232] H. Liu, S. Chu, R. Peng, M. Liu, Z. Chen, B. Jin, S. Chu, Synthesis, microstructure, growth mechanism and photoluminescence of high quality [0001]-oriented InN nanowires and nanonecklaces, CrystEngComm 17(26) (2015) 4818-4824.

[233] L.W. Yin, Y. Bando, D. Golberg, M.S. Li, Growth of single-crystal indium nitride nanotubes and nanowires by a controlled-carbonitridation reaction route, Advanced Materials 36(2) (2005) 1833-1838.

[234] S. Luo, W. Zhou, W. Wang, Z. Zhang, L. Liu, X. Dou, J. Wang, X. Zhao, D. Liu, Y. Gao, Template-free synthesis of helical hexagonal microtubes of indium nitride, Applied Physics Letters 87(6) (2005) 063109

[235] X.H. Ji, S.P. Lau, H.Y. Yang, S.F. Yu, Aligned InN nanofingers prepared by the ion-beam assisted filtered cathodic vacuum arc technique, Nanotechnology 16(12) (2005) 3069-3073.

[236] S. Zhao, Q. Wang, Z. Mi, S. Fathololoumi, T. Gonzalez, M.P. Andrews, Observation of phonon sideband emission in intrinsic InN nanowires: a photoluminescence and micro-Raman scattering study, Nanotechnology 23(41) (2012) 415706.

[237] L. Monteagudolerma, S. Valduezafelip, A. Núñezcascajero, A. Ruiz, M. Gonzálezherráez, E. Monroy, F.B. Naranjo, Morphology and arrangement of InN nanocolumns deposited by radio-frequency sputtering: Effect of the buffer layer, Journal of Crystal Growth 434 (2015) 13-18.

[238] H. Yang, J. Yin, W. Li, F. Gao, Y. Zhao, G. Wu, B. Zhang, G. Du, In-assisted growth of InN nanocolumn on Si(111) substrate by molecular beam epitaxy, Vacuum 128 (2016) 133-136.

[239] A.T.M.G. Sarwar, F. Yang, B.D. Esser, T.F. Kent, D.W. Mccomb, R.C. Myers, Self-assembled InN micro-mushrooms by upside-down pendeoepitaxy, Journal of Crystal Growth 443 (2016) 90-97.

[240] T. Kouno, M. Sakai, K. Kishino, A. Kikuchi, N. Umehara, K. Hara, Crystal structure and optical properties of a high-density InGaN nanoumbrella array as a white light source without phosphors, NPG Asia Materials 8(7) (2016) e289.

[241] S. Zhao, S.Y. Woo, S.M. Sadaf, Y. Wu, A. Pofelski, D.A. Laleyan, R.T. Rashid, Y. Wang, G.A. Botton, Z. Mi, Molecular beam epitaxy growth of Al-rich AlGaN nanowires for deep ultraviolet optoelectronics, APL Materials 4(8) (2016) 086115.

[242] Q. Wang, A. Connie, H. Nguyen, M. Kibria, S. Zhao, S. Sharif, I. Shih, Z. Mi, Highly efficient, spectrally pure 340 nm ultraviolet emission from AlxGa1-xN nanowire based light emitting diodes, Nanotechnology 24(34) (2013) 345201.

[243] H. Sekiguchi, K. Kishino, A. Kikuchi, Emission color control from blue to red with nanocolumn diameter of InGaN/GaN nanocolumn arrays grown on same substrate, Applied Physics Letters 96(23) (2010) 5071-5074.

[244] J. Kamimura, K. Kishino, A. Kikuchi, Low-temperature photoluminescence studies of In-rich InAlN nanocolumns, Physica Status Solidi (RRL)-Rapid Research Letters 6(3) (2012) 123-125.

[245] J. Wu, W. Walukiewicz, K.M. Yu, J.W.A. Iii, S.X. Li, E.E. Haller, H. Lu, W.J. Schaff, Universal

bandgap bowing in group-III nitride alloys, Solid State Communications 127(6) (2003) 411-414.
[246] R.E. Jones, R. Broesler, K.M. Yu, J.W.I. Ager, W. Walukiewicz, X. Chen, W.J. Schaff, Band gap bowing parameter of $In_{1-x}Al_xN$, Journal of Applied Physics 104(12) (2008)123501.
[247] B.T. Liou, S.H. Yen, Y.K. Kuo, Vegard's law deviation in band gap and bowing parameter of AlxIn1-xN, Applied Physics A 81(81) (2005) 651-655.
[248] S. Bellucci, A.I. Popov, C. Balasubramanian, G. Cinque, A. Marcelli, I. Karbovnyk, V. Savchyn, N. Krutyak, Luminescence, vibrational and XANES studies of AlN nanomaterials, Radiation Measurements 42(4-5) (2007) 708-711.
[249] B. Liu, Y. Bando, A. Wu, X. Jiang, B. Dierre, T. Sekiguchi, C. Tang, M. Mitome, D. Golberg, 352 nm ultraviolet emission from high-quality crystalline AlN whiskers, Nanotechnology 21(7) (2010) 589-594.
[250] H.M. Kim, T.W. Kang, K.S. Chung, Nanoscale ultraviolet-light-emitting diodes using wide-bandgap gallium nitride nanorods, Advanced Materials 15(7-8) (2003) 567-569.
[251] Q. Li, Y. Lin, J.R. Creighton, J.J. Figiel, G.T. Wang, Nanowire-templated lateral epitaxial growth of low-dislocation density nonpolar a-plane GaN on r-plane sapphire, Advanced Materials 21(23) (2009) 2416-2420.
[252] M. Heilmann, A.M. Munshi, G. Sarau, M. Göbelt, C. Tessarek, V.T. Fauske, A.T. van Helvoort, J. Yang, M. Latzel, B. Hoffmann, Vertically oriented growth of GaN nanorods on Si using graphene as atomically thin buffer layer, Nano Letters 16(6) (2016)3524-3532.
[253] G. Guzmán, M. Herrera, R. Silva, G.C. Vásquez, D. Maestre, Influence of oxygen incorporation on the defect structure of GaN microrods and nanowires. An XPS and CL study, Semiconductor Science & Technology 31(5) (2016) 055006.
[254] P.M. Coulon, M. Mexis, M. Teisseire, M. Jublot, P. Vennegues, M. Leroux, J. Zuniga-Perez, Dual-polarity GaN micropillars grown by metalorganic vapour phase epitaxy: Cross-correlation between structural and optical properties, Journal of Applied Physics 115(15) (2014) 153504.
[255] T.R. Kuykendall, M.V. Altoe, D.F. Ogletree, S. Aloni, Catalyst-directed crystallographic orientation control of GaN nanowire growth, Nano Letters 14(12) (2014) 6767-6773.
[256] G. Guzmán, M. Herrera, Cathodoluminescence of GaN nanorods and nanowires grown by thermal evaporation, Semiconductor Science & Technology 29(29) (2014) 387-392.
[257] B. Liu, F. Yuan, B. Dierre, T. Sekiguchi, S. Zhang, Y. Xu, X. Jiang, Origin of yellow-band emission in epitaxially grown GaN nanowire arrays, Acs Applied Materials & Interfaces 6(16) (2014) 14159-14166.
[258] M. Tangi, A. De, J. Ghatak, S.M. Shivaprasad, Electron mobility of self-assembled and dislocation free InN nanorods grown on GaN nano wall network template, Journal of Applied Physics 119(20) (2016) 032101.
[259] M. Lei, K. Huang, R. Zhang, H.J. Yang, X.L. Fu, Y.G. Wang, W.H. Tang, Catalyst-free chemical vapor deposition route to InN nanowires and their cathodoluminescence properties, Journal of Alloys

and Compounds 535(9) (2012) 50-52.
[260] A. Pierret, C. Bougerol, M.D. Hertog, B. Gayral, M. Kociak, H. Renevier, B. Daudin, Structural and optical properties of $Al_xGa_{1-x}N$ nanowires, Physica Status Solidi-Rapid Research Letters 7(10) (2013) 868-873.
[261] H.M. Kim, H. Lee, S.I. Kim, S.R. Ryu, T.W. Kang, K.S. Chung, Formation of InGaN nanorods with indium mole fractions by hydride vapor phase epitaxy, Physica Status Solidi B-Basic Solid State Physics 241(12) (2004) 2802–2805.
[262] C. Tessarek, S. Fladischer, C. Dieker, G. Sarau, B. Hoffmann, M. Bashouti, M. Göbelt, M. Heilmann, M. Latzel, E. Butzen, Self-catalyzed growth of vertically aligned InN nanorods by metal-organic vapor phase epitaxy, Nano Letters 16(6)(2016) 3415-3425.
[263] Y.H. Ra, R. Navamathavan, S. Kang, C.R. Lee, Different characteristics of InGaN/GaN multiple quantum well heterostructures grown on m- and r-planes of a single n-GaN nanowire using metalorganic chemical vapor deposition, Journal of Materials Chemistry C 2(15) (2014) 2692-2701.
[264] S. Albert, A. Bengoecheaencabo, M.A. Sanchezgarcia, E. Calleja, U. Jahn, Selective area growth and characterization of InGaN nanocolumns for phosphor-free white light emission, Journal of Applied Physics 113(11) (2013) 208-217.
[265] J. Ristic, E. Calleja, M.A. Sánchez-García, J.M. Ulloa, J. Sánchez-Páramo, J.M. Calleja, U. Jahn, A. Trampert, K.H. Ploog, Characterization of GaN quantum discs embedded in AlxGa1-xN nanocolumns grown by molecular beam epitaxy, Physical Review B 68(12) (2003)125305.
[266] Q. Liu, T. Tanaka, J. Hu, F. Xu, T. Sekiguchi, Green emission from c-axis oriented AlN nanorods doped with Tb, Applied Physics Letters 83(24) (2003) 4939-4941.
[267] M.G. Kibria, F.A. Chowdhury, S. Zhao, M.L. Trudeau, H. Guo, Z. Mi, Defect-engineered GaN:Mg nanowire arrays for overall water splitting under violet light, Applied Physics Letters 106(11) (2015) 113105.
[268] A.T. Connie, S. Zhao, S.M. Sadaf, I. Shih, Z. Mi, X. Du, J. Lin, H. Jiang, Optical and electrical properties of Mg-doped AlN nanowires grown by molecular beam epitaxy, Applied Physics Letters 106(21) (2015) 213105.
[269] S. Zhao, X. Liu, Z. Mi, Photoluminescence properties of Mg-doped InN nanowires, Applied Physics Letters 103(20) (2013) 20311.
[270] X. Ji, S. Lau, S. Yu, H. Yang, T. Herng, A. Sedhain, J. Lin, H. Jiang, K. Teng, J. Chen, Ultraviolet photoluminescence from ferromagnetic Fe-doped AlN nanorods, Applied physics letters 90(19) (2007) 193118.
[271] Y. Yang, Q. Zhao, X. Zhang, Z. Liu, C. Zou, B. Shen, D. Yu, Mn-doped AlN nanowires with room temperature ferromagnetic ordering, Applied Physics Letters 90(9) (2007) 092118.
[272] M.G. Kibria, F.A. Chowdhury, S. Zhao, M.L. Trudeau, H. Guo, Z. Mi, Defect-engineered GaN:Mg nanowire arrays for overall water splitting under violet light, Applied Physics Letters 106(11) (2015) 113105.
[273] F.L. Deepak, P.V. Vanitha, A. Govindaraj, C.N.R. Rao, Photoluminescence spectra and

ferromagnetic properties of GaMnN nanowires, Chemical Physics Letters 374(3) (2003) 314-318.
[274] Y. Huang, X. Duan, Y. Cui, C.M. Lieber, Gallium nitride nanowire nanodevices, Nano Letters 2(2) (2002) 101-104.
[275] V.M. Polyakov, F. Schwierz, F. Fuchs, J. Furthmuller, F. Bechstedt, Low-field and high-field electron transport in zinc blende InN, Applied Physics Letters 94(2) (2009) 022102.
[276] S. Wang, H. Liu, B. Gao, H. Cai, Monte Carlo calculation of electron diffusion coefficient in wurtzite indium nitride, Applied Physics Letters 100(14) (2012) 142105.
[277] S. Zhao, O. Salehzadeh, S. Alagha, K.L. Kavanagh, Probing the electrical transport properties of intrinsic InN nanowires, Applied Physics Letters 102(7) (2013) 073102.
[278] Y.-B. Tang, X.-H. Bo, J. Xu, Y.-L. Cao, Z.-H. Chen, H.-S. Song, C.-P. Liu, T.-F. Hung, W.-J. Zhang, H.-M. Cheng, Tunable p-Type conductivity and transport properties of AlN nanowires via Mg doping, ACS Nano 5(5) (2011) 3591-3598.
[279] Z Cai, S. Garzon, M.V.S. Chandrashekhar, R.A. Webb, G. Koley, Synthesis and properties of high-quality InN nanowires and nanonetworks, Journal of Electronic Materials 37(5) (2008) 585-592
[280] G. Cheng, E. Stern, D. Turner-Evans, M.A. Reed, Electronic properties of InN nanowires, Applied Physics Letters 87(25) (2005) 253103.
[281] G. Koley, Z. Cai, E.B. Quddus, J. Liu, M. Qazi, R.A. Webb, Growth direction modulation and diameter-dependent mobility in InN nanowires, Nanotechnology 22(29) (2011) 295701.
[282] T. Richter, H. Lüth, T. Schäpers, R. Meijers, K. Jeganathan, H.S. Estévez, R. Calarco, M. Marso, Electrical transport properties of single undoped and n-type doped InN nanowires, Nanotechnology 20(40) (2009) 17579-17584.
[283] N. Ma, X.Q. Wang, S.T. Liu, G. Chen, J.H. Pan, L. Feng, F.J. Xu, N. Tang, B. Shen, Hole mobility in wurtzite InN, Applied Physics Letters 98(19) (2011) 192114.
[284] J.R. Kim, H.M. So, J.W. Park, J.J. Kim, J. Kim, C.J. Lee, S.C. Lyu, Electrical transport properties of individual gallium nitride nanowires synthesized by chemical-vapor-deposition, Applied Physics Letters 80(19) (2002) 3548-3550.
[285] Z. Zhong, F. Qian, D. Wang, C.M. Lieber, Synthesis of p-type gallium nitride nanowires for electronic and photonic nanodevices, Nano Letters 3(3) (2003) 343-346.
[286] C.Y. Chang, G.C. Chi, W.M. Wang, L.C. Chen, K.H. Chen, F. Ren, S.J. Pearton, Electrical transport properties of single GaN and InN nanowires, Journal of Electronic Materials 35(4) (2006) 738-743.
[287] T. Kuykendall, P. Pauzauskie, S. Lee, Y.F. Zhang, A.J. Goldberger, P.D. Yang, Metalorganic chemical vapor deposition route to GaN nanowires with triangular cross sections, Nano Letters 3(8) (2003) 1063-1066.
[288] H.W. Seo, L.W. Tu, Q.Y. Chen, C.Y. Ho, Y.T. Lin, K.L. Wu, D.J. Jang, D.P. Norman, N.J. Ho, Photogated transistor of III-nitride nanorods, Applied Physics Letters 96(10) (2010) 101114.
[289] H.M. Kim, T.W. Kang, K.S. Chung, Nanoscale ultraviolet-light-emitting diodes using wide-bandgap gallium nitride nanorods, Advanced Materials 15(7-8) (2003) 567-569.
[290] X. Tang, G. Li, S. Zhou, Ultraviolet electroluminescence of light-emitting diodes based on single

n-ZnO/p-AlGaN heterojunction nanowires, Nano Letters 13(11) (2013) 5046-5050.
[291] S.G. Zhang, X.W. Zhang, F.T. Si, J.J. Dong, J.X. Wang, X. Liu, Z.G. Yin, H.L. Gao, Ordered ZnO nanorods-based heterojunction light-emitting diodes with graphene current spreading layer, Applied Physics Letters 101(12) (2012) 121104.
[292] T. Wang, H. Wu, Z. Wang, C. Chen, C. Liu, Ultralow emission threshold light-emitting diode of nanocrystalline ZnO/p-GaN heterojunction, IEEE Electron Device Letters 33(7) (2012) 1030-1032.
[293] A. Kikuchi, M. Kawai, M. Tada, K. Kishino, InGaN/GaN multiple quantum disk nanocolumn light-emitting diodes grown on (111) Si substrate, Japanese Journal of Applied Physics 43(12A) (2004) L1524--L1526.
[294] S.D. Carnevale, T.F. Kent, P.J. Phillips, M.J. Mills, S. Rajan, R.C. Myers, Polarization-induced pn diodes in wide-band-gap nanowires with ultraviolet electroluminescence, Nano Letters 12(2) (2012) 915-920.
[295] B.J. May, A.T.M.G. Sarwar, R.C. Myers, Nanowire LEDs grown directly on flexible metal foil, Applied Physics Letters 108(14) (2016) 2780-2786.
[296] A.T. Sarwar, B.J. May, M.F. Chisholm, G.J. Duscher, R.C. Myers, Ultrathin GaN quantum disk nanowire LEDs with sub-250 nm electroluminescence, Nanoscale 8(15) (2016) 8024-8032.
[297] S. Zhao, A.T. Connie, M.H.T. Dastjerdi, X.H. Kong, Q. Wang, M. Djavid, S. Sadaf, X.D. Liu, I. Shih, H. Guo, Aluminum nitride nanowire light emitting diodes: Breaking the fundamental bottleneck of deep ultraviolet light sources, Scientific Reports 5 (2015) 8332.
[298] S. Zhao, M. Djavid, Z. Mi, Surface Emitting, High efficiency near-vacuum ultraviolet light source with aluminum nitride nanowires monolithically grown on silicon, Nano Letters 15(10) (2015) 7006-7009.
[299] S. Zhao, S.M. Sadaf, S. Vanka, Y. Wang, R. Rashid, Z. Mi, Sub-milliwatt AlGaN nanowire tunnel junction deep ultraviolet light emitting diodes on silicon operating at 242 nm, Applied Physics Letters 109(20) (2016) 325.
[300] S. Sadaf, S. Zhao, Y. Wu, Y.-H. Ra, X. Liu, S. Vanka, Z. Mi, An AlGaN core–shell tunnel junction nanowire light-emitting diode operating in the ultraviolet-C band, Nano letters 17(2) (2017) 1212-1218.
[301] H. X. Jiang, J. Y. Lin, Hexagonal boron nitride for deep ultraviolet photonic devices, Semiconductor Science and Technology, 29(8) (2014) 084003.
[302] S. Majety, J. Li, X. K. Cao, R. Dahal, B. N. Pantha, J. Y. Lin, H. X. Jiang, Epitaxial growth and demonstration of hexagonal BN/AlGaN p-n junctions for deep ultraviolet photonics, Applied Physics Letters, 100(6) (2012) 061121.
[303] D. A. Laleyan, S. R. Zhao, S. Y. Woo, H. N. Tran, H. B. Le, T. Szkopek, H. Guo, G. A. Botton, Z. T. Mi, AlN/h-BN heterostructures for Mg dopant-Free deep ultraviolet photonics, Nano Letters, 17(6) (2017) 3738-3743.
[304] S. Zhao, H.P.T. Nguyen, M.G. Kibria, Z. Mi, III-Nitride nanowire optoelectronics, Progress in Quantum Electronics 44 (2015) 14-68.
[305] Y.H. Ra, R. Navamathavan, J.H. Park, C.R. Lee, High-quality uniaxial $In_xGa_{1-x}N$/GaN multiple

quantum well (MQW) nanowires (NWs) on Si(111) grown by metal-organic chemical vapor deposition (MOCVD) and light-emitting diode (LED) fabrication, ACS Applied Materials & Interfaces 5(6) (2013) 2111-2117.

[306] K. Kishino, K. Yamano, Green-light nanocolumn light emitting diodes with triangular-lattice uniform arrays of InGaN-based nanocolumns, IEEE Journal of Quantum Electronics 50(7) (2014) 538-547.

[307] A. Bengoechea-Encabo, S. Albert, D. Lopezromero, P. Lefebvre, F. Barbagini, A. Torrespardo, J.M. Gonzalezcalbet, M.A. Sanchezgarcia, E. Calleja, Light-emitting-diodes based on ordered InGaN nanocolumns emitting in the blue, green and yellow spectral range, Nanotechnology 25(43) (2014) 435203.

[308] E. Jang, S. Jun, H. Jang, J. Lim, B. Kim, Y. Kim, White-light-emitting diodes with quantum dot color converters for display backlights, Advanced Materials 22(28) (2010) 3076-80.

[309] J.H. Oh, S.J. Yang, Y.R. Do, Healthy, natural, efficient and tunable lighting: four-package white LEDs for optimizing the circadian effect, color quality and vision performance, Light Science & Applications 3 (2014) e141.

[310] E.F. Schubert, J.K. Kim, Solid-state light sources getting smart, Science 308(5726) (2005) 1274-8.

[311] C. Hahn, Z. Zhang, A. Fu, C.H. Wu, Y.J. Hwang, D.J. Gargas, P. Yang, Epitaxial growth of InGaN nanowire arrays for light emitting diodes, ACS Nano 5(5) (2011) 3970-3976.

[312] Y.J. Hong, C.H. Lee, J. Yoo, Y.J. Kim, J. Jeong, M. Kim, G.C. Yi, Emission color-tuned light-emitting diode microarrays of nonpolar $In_xGa_{1-x}N$/GaN multishell nanotube heterostructures, Scientific Reports 5 (2015) 289-302.

[313] S. Albert, A. Bengoecheaencabo, M.A. Sánchezgarcía, X. Kong, A. Trampert, E. Calleja, Selective area growth of In(Ga)N/GaN nanocolumns by molecular beam epitaxy on GaN-buffered Si(111): from ultraviolet to infrared emission, Nanotechnology 24(17) (2013) 2212-2217.

[314] D. Min, P. Donghwy, J. Jongjin, L. Kyuseung, N. Okhyun, Phosphor-free white-light emitters using in-situ GaN nanostructures grown by metal organic chemical vapor deposition, Scientific Reports 5 (2015) 17372.

[315] R. Wang, X. Liu, I. Shih, Z. Mi, High efficiency, full-color AlInGaN quaternary nanowire light emitting diodes with spontaneous core-shell structures on Si, Applied Physics Letters 106(26) (2015) 261104.

[316] Y.J. Hong, C.H. Lee, A. Yoon, M. Kim, H.K. Seong, H.J. Chung, C. Sone, Y.J. Park, G.C. Yi, Visible-color-tunable light-emitting diodes, Advanced Materials 23(29) (2011) 3284-3288.

[317] D.J. Kong, C.M. Kang, J.Y. Lee, J. Kim, D.S. Lee, Color tunable monolithic InGaN/GaN LED having a multi-junction structure, Optics Express 24(6) (2016) A667-A673.

[318] H. Li, P. Li, J. Kang, Z. Li, Z. Li, J. Li, X. Yi, G. Wang, Phosphor-free, color-tunable monolithic InGaN light-emitting diodes, Applied Physics Express 6(10) (2013) 825-831.

[319] Y. Tchoe, J. Jo, M. Kim, J. Heo, G. Yoo, C. Sone, G.C. Yi, Variable-color light-emitting diodes using GaN microdonut arrays, Advanced Materials 26(19) (2014) 3019–3023.

[320] R. Wang, H.P. Nguyen, A.T. Connie, J. Lee, I. Shih, Z. Mi, Color-tunable, phosphor-free InGaN

nanowire light-emitting diode arrays monolithically integrated on silicon, Optics Express 22(S7) (2014) A1768-A1775.
[321] Y.H. Ra, R. Wang, S.Y. Woo, M. Djavid, S.M. Sadaf, J. Lee, G.A. Botton, Z. Mi, Full-color single nanowire pixels for projection displays, Nano Letters 16(7)(2016)4608-4615.
[322] K. Kishino, K. Nagashima, K. Yamano, Monolithic integration of InGaN-based nanocolumn light-emitting diodes with different emission colors, Applied Physics Express 6(1) (2013) 128-133.
[323] F. Qian, S. Gradecak, Y. Li, C.Y. Wen, C.M. Lieber, Core/multishell nanowire heterostructures as multicolor, high-efficiency light-emitting diodes, Nano Letters 5(11) (2005) 2287-2291.
[324] K. Kishino, A. Kikuchi, H. Sekiguchi, S. Ishizawa, InGaN/GaN nanocolumn LEDs emitting from blue to red, Proceedings of SPIE 6473 (2007) 64730T.
[325] H.W. Lin, Y.J. Lu, H.Y. Chen, H.M. Lee, S. Gwo, InGaN/GaN nanorod array white light-emitting diode, Applied Physics Letters 97(7) (2010) 073101.
[326] W. Guo, M. Zhang, A. Banerjee, P. Bhattacharya, Catalyst-free InGaN/GaN nanowire light emitting diodes grown on (001) silicon by molecular beam epitaxy, Nano Letters 10(9) (2010) 3355-3359.
[327] H.P.T. Nguyen, S. Zhang, A.T. Connie, M.G. Kibria, Q. Wang, I. Shih, Z. Mi, Breaking the carrier injection bottleneck of phosphor-free nanowire white light-emitting diodes, Nano Letters 13(11) (2013) 5437-5442.
[328] H.P.T. Nguyen, M. Djavid, S.Y. Woo, X. Liu, A.T. Connie, S. Sadaf, Q. Wang, G.A. Botton, I. Shih, Z. Mi, Engineering the carrier dynamics of InGaN nanowire white light-emitting diodes by distributed p-AlGaN electron blocking layers, Scientific Reports 5 (2015) 7744.
[329] H.P.T. Nguyen, S. Zhang, K. Cui, X. Han, S. Fathololoumi, M. Couillard, G.A. Botton, Z. Mi, p-Type modulation doped InGaN/GaN dot-in-a-wire white-light-emitting diodes monolithically grown on Si(111), Nano Letters 11(5) (2011) 1919-1924.
[330] H.P.T. Nguyen, K. Cui, S. Zhang, S. Fathololoumi, Z. Mi, Full-color InGaN/GaN dot-in-a-wire light emitting diodes on silicon, Nanotechnology 22(44) (2011) 3096-3100.
[331] H.P.T. Nguyen, K. Cui, S. Zhang, M. Djavid, A. Korinek, G.A. Botton, Z. Mi, Controlling electron overflow in phosphor-free InGaN/GaN nanowire white light-emitting diodes, Nano Letters 12(3) (2012) 1317-1323.
[332] H.P.T. Nguyen, M. Djavid, K. Cui, Z. Mi, Temperature-dependent nonradiative recombination processes in GaN-based nanowire white-light-emitting diodes on silicon, Nanotechnology 23(19) (2012) 404-414.
[333] H.P.T. Nguyen, M. Djavid, Z. Mi, Nonradiative recombination mechanism in phosphor-free GaN-based nanowire white light emitting diodes and the effect of ammonium sulfide surface passivation, ECS Transactions 53(2) (2013) 93-100.
[334] A.T. Connie, H.P.T. Nguyen, S.M. Sadaf, I. Shih, Z. Mi, Engineering the color rendering index of phosphor-free InGaN/(Al)GaN nanowire white light emitting diodes grown by molecular beam epitaxy, Journal of vacuum science & technology B 32(2) (2014) 02C113.

[335] H.P.T. Nguyen, Q. Wang, Z. Mi, Phosphor-free InGaN/GaN Dot-in-a-wire white light-emitting diodes on copper substrates, Journal of Electronic Materials 43(4) (2014) 868-872.
[336] M.L. Lee, Y.H. Yeh, S.J. Tu, P.C. Chen, W.C. Lai, J.K. Sheu, White emission from non-planar InGaN/GaN MQW LEDs grown on GaN template with truncated hexagonal pyramids, Optics Express 23(7) (2015) 401-412.
[337] S.M. Sadaf, Y.H. Ra, H.P. Nguyen, M. Djavid, Z. Mi, Alternating-current InGaN/GaN tunnel junction nanowire white-light emitting diodes, Nano Letters 15(10) (2015) 6696-6701.
[338] K. Kishino, J. Kamimura, K. Kamiyama, Near-infrared InGaN nanocolumn light-emitting diodes operated at 1.46 μm, Applied Physics Express 5(3) (2012) 031001.
[339] B.H. Le, S. Zhao, N.H. Tran, Z. Mi, Electrically injected near-infrared light emission from single InN nanowire p-i-n diode, Applied Physics Letters 105(23) (2014) 231124.
[340] K. Kishino, S. Ishizawa, Selective-area growth of GaN nanocolumns on Si(111) substrates for application to nanocolumn emitters with systematic analysis of dislocation filtering effect of nanocolumns, Nanotechnology 26(22) (2015) 14-22.
[341] C. Zhao, T.K. Ng, N. Wei, A. Prabaswara, M.S. Alias, B. Janjua, C. Shen, B.S. Ooi, Facile formation of high-quality InGaN/GaN quantum-disks-in-nanowires on bulk-metal substrates for high-power light-emitters, Nano Letters 16(2) (2016) 1056-1063.
[342] C. Zhao, T.K. Ng, R.T. Elafandy, A. Prabaswara, G.B. Consiglio, I.A. Ajia, I.S. Roqan, B. Janjua, C. Shen, J. Eid, Droop-free, reliable, and high-power InGaN/GaN nanowire light-emitting diodes for monolithic metal-optoelectronics, Nano Letters 16(7) (2016) 4616-4623.
[343] S. X. Jin, J. Li, J. Z. Li, J. Y. Lin, H. X. Jiang, GaN microdisk light emitting diodes, Applied Physics Letters 76(5) (2000)631.
[344] J. Y. Lin, H. X. Jiang, Development of microLED, Applied Physics Letters 116(10)(2020) 100502.
[345] K. Kishino, N. Sakakibara, K. Narita, Takao Oto, Two-dimensional multicolor (RGBY) integrated nanocolumn micro-LEDs as a fundamental technology of micro-LED display, Applied Physics Express 13(1) (2020) 014003.
[346] R. Calarco, M. Marso, T. Richter, A.I. Aykanat, R. Meijers, V.D.H. A, T. Stoica, H. Lüth, Size-dependent photoconductivity in MBE-grown GaN-nanowires, Nano Letters 5(5) (2005) 981-984.
[347] A. Armstrong, G.T. Wang, A.A. Talin, Depletion-mode photoconductivity study of deep levels in GaN nanowires, Journal of Electronic Materials 38(4) (2009) 484-489.
[348] H.M. Huang, R.S. Chen, H.Y. Chen, T.W. Liu, C.C. Kuo, C.P. Chen, H.C. Hsu, L.C. Chen, K.H. Chen, Y.J. Yang, Photoconductivity in single AlN nanowires by subband gap excitation, Applied Physics Letters 96(6) (2010) 062104.
[349] W.Y. Weng, T.J. Hsueh, S.J. Chang, S.B. Wang, H.T. Hsueh, G.J. Huang, A high-responsivity GaN nanowire UV photodetector, IEEE Journal of Selected Topics in Quantum Electronics 17(4) (2011) 996-1001.
[350] X. Wang, Y. Zhang, X. Chen, M. He, C. Liu, Y. Yin, X. Zou, S. Li, Ultrafast, superhigh gain

visible-blind UV detector and optical logic gates based on nonpolar a-axial GaN nanowire, Nanoscale 6(20) (2014) 12009-12017.
[351] N. Erhard, A.T. Sarwar, F. Yang, D.W. Mccomb, R.C. Myers, A.W. Holleitner, Optical control of internal electric fields in band-gap graded InGaN nanowires, Nano Letters 15(1) (2015) 332-338.
[352] H. Wu, Y. Sun, D. Lin, R. Zhang, C. Zhang, W. Pan, GaN nanofibers based on electrospinning: faciles synthesis, controlled assembly, precise doping, and application as high performance UV photodetector, Advanced Materials 21(2) (2009) 227–231.
[353] W. Zheng, F. Huang, R. Zheng, H. Wu, Low-dimensional structure vacuum-ultraviolet-sensitive ($\lambda < 200$ nm) photodetector with fast-response-speed based on high-quality AlN micro/nanowire, Advanced Materials 27(26) (2015) 3921-3927.
[354] T. Richter, H.L.R. Meijers, R. Calarco, M. Marso, Doping concentration of GaN nanowires determined by opto-electrical measurements, Nano Letters 8(9) (2008) 3056-3059.
[355] A. Patsha, S. Amirthapandian, R. Pandian, S. Bera, A. Bhattacharya, S. Dhara, Direct evidence of Mg incorporation pathway in vapor-liquid-solid grown p-type nonpolar GaN nanowires, The Journal of Physical Chemistry C 118(41) (2014) 24165-24172.
[356] S. Kang, A. Mandal, J.H. Park, D.Y. Um, J.H. Chu, S.Y. Kwon, C.R. Lee, Effects of growth temperatures on the characteristics of n-GaN nanorods-graphene hybrid structures, Journal of Alloys and Compounds 644 (2015) 808-813.
[357] L. Rigutti, M. Tchernycheva, L.B.A. De, G. Jacopin, F.H. Julien, L.F. Zagonel, K. March, O. Stephan, M. Kociak, R. Songmuang, Ultraviolet photodetector based on GaN/AlN quantum disks in a single nanowire, Nano Letters 10(10) (2010) 2939-2943.
[358] A.L. Bugallo, M. Tchernycheva, G. Jacopin, L. Rigutti, F.H. Julien, S.T. Chou, Y.T. Lin, P.H. Tseng, L.W. Tu, Visible-blind photodetector based on p-i-n junction GaN nanowire ensembles, Nanotechnology 21(31) (2010) 315201.
[359] A.D.L. Bugallo, L. Rigutti, G. Jacopin, F.H. Julien, C. Durand, X.J. Chen, D. Salomon, J. Eymery, M. Tchernycheva, Single-wire photodetectors based on InGaN/GaN radial quantum wells in GaN wires grown by catalyst-free metal-organic vapor phase epitaxy, Applied Physics Letters 98(23) (2011) 1552-1556.
[360] F. González-Posada, R. Songmuang, H.M. Den, E. Monroy, Room-temperature photodetection dynamics of single GaN nanowires, Nano Letters 12(1) (2012) 172-176.
[361] J. Lähnemann, M.D. Hertog, P. Hille, M.A.D.L. Mata, T. Fournier, J. Schörmann, J. Arbiol, M. Eickhoff, E. Monroy, UV photosensing characteristics of nanowire-based GaN/AlN superlattices, Nano Letters 16(5) (2016) 3260-3267.
[362] T.E. Journot, V. Bouchiat, B. Gayral, J. Dijon, B.r.r. Hyot, Self-assembled UV photodetector made by direct epitaxial GaN growth on graphene, ACS Applied Materials & Interfaces 10(22) (2018) 18857-18862.
[363] K. Xu, C. Xu, Y. Xie, J. Deng, Y. Zhu, W. Guo, M. Xun, K.B. Teo, H. Chen, J. Sun, Graphene GaN-based schottky ultraviolet detectors, IEEE Transactions on Electron Devices 62(9) (2015)

2802-2808.
[364] A. Babichev, H. Zhang, P. Lavenus, F. Julien, A.Y. Egorov, Y. Lin, L. Tu, M. Tchernycheva, GaN nanowire ultraviolet photodetector with a graphene transparent contact, Applied Physics Letters 103(20) (2013) 201103.
[365] M.H. Huang, S. Mao, H. Feick, H. Yan, Y. Wu, H. Kind, E. Weber, R. Russo, P. Yang, ChemInform Abstract: Room-temperature ultraviolet nanowire nanolasers, Science 292(5523) (2001) 1897-1899.
[366] H.-J. Choi, J.C. Johnson, R. He, S.-K. Lee, F. Kim, P. Pauzauskie, J. Goldberger, R.J. Saykally, P. Yang, Self-organized GaN quantum wire UV lasers, The Journal of Physical Chemistry B 107(34) (2003) 8721-8725.
[367] S. Gradečak, F. Qian, Y. Li, H.-G. Park, C.M. Lieber, GaN nanowire lasers with low lasing thresholds, Applied Physics Letters 87(17) (2005) 173111.
[368] P.J. Pauzauskie, D.J. Sirbuly, P. Yang, Semiconductor nanowire ring resonator laser, Physical Review Letters 96(14) (2006) 143903.
[369] H.G. Park, F. Qian, C.J. Barrelet, Y. Li, Microstadium single-nanowire laser, Applied Physics Letters 91(25) (2007) 251115.
[370] F. Qian, Y. Li, S. Gradecak, H.G. Park, Y. Dong, Y. Ding, Z.L. Wang, C.M. Lieber, Multi-quantum-well nanowire heterostructures for wavelength-controlled lasers, Nature Materials 7(9) (2008) 701-706.
[371] T. Kouno, K. Kishino, K. Yamano, A. Kikuchi, Two-dimensional light confinement in periodic InGaN/GaN nanocolumn arrays and optically pumped blue stimulated emission, Optics Express 17(22) (2009) 20440-20447.
[372] R. Chen, H.D. Sun, T. Wang, K.N. Hui, H.W. Choi, Optically pumped ultraviolet lasing from nitride nanopillars at room temperature, Applied Physics Letters 96(24) (2010) 241101.
[373] M. Sakai, Y. Inose, K. Ema, T. Ohtsuki, Random laser action in GaN nanocolumns, Applied Physics Letters 97(15) (2010) 151109.
[374] S. Ishizawa, K. Kishino, R. Araki, A. Kikuchi, S. Sugimoto, Optically pumped green (530--560 nm) stimulated emissions from InGaN/GaN multiple-quantum-well triangular-lattice nanocolumn arrays, Applied Physics Express 4(5) (2011) 1166-1173.
[375] J. Heo, W. Guo, P. Bhattacharya, Monolithic single GaN nanowire laser with photonic crystal microcavity on silicon, Applied Physics Letters 98(2) (2011) 021110.
[376] C.Y. Wu, C.T. Kuo, C.Y. Wang, C.L. He, M.H. Lin, H. Ahn, S. Gwo, Plasmonic green nanolaser based on a metal-oxide-semiconductor structure, Nano Letters 11(10) (2011) 4256-4260.
[377] A. Das, J. Heo, M. Jankowski, W. Guo, L. Zhang, H. Deng, P. Bhattacharya, Room temperature ultralow threshold GaN nanowire polariton laser, Physical Review Letters 107(6) (2011) 066405.
[378] H. Xu, J.B. Wright, A. Hurtado, Q. Li, T.S. Luk, J.J. Figiel, K. Cross, G. Balakrishnan, L.F. Lester, I. Brener, Gold substrate-induced single-mode lasing of GaN nanowires, Applied Physics Letters 101(22) (2012) 221114.
[379] Y.J. Lu, J. Kim, H.Y. Chen, C. Wu, N. Dabidian, C.E. Sanders, C.Y. Wang, M.Y. Lu, B.H. Li, X.

Qiu, Plasmonic nanolaser using epitaxially grown silver film, Science 337(337) (2012) 450-453.
[380] Q. Li, J.B. Wright, W.W. Chow, T.S. Luk, I. Brener, L.F. Lester, G.T. Wang, Single-mode GaN nanowire lasers, Optics Express 20(16) (2012) 17873-17879.
[381] H. Xu, J.B. Wright, T.S. Luk, J.J. Figiel, K. Cross, L.F. Lester, G. Balakrishnan, G.T. Wang, I. Brener, Q. Li, Single-mode lasing of GaN nanowire-pairs, Applied Physics Letters 101(11) (2012) 113106.
[382] S.P. Chang, K.P. Sou, C.H. Chen, Y.J. Cheng, J.K. Huang, C.H. Lin, H.C. Kuo, C.Y. Chang, W.F. Hsieh, Lasing action in gallium nitride quasicrystal nanorod arrays, Optics Express 20(11) (2012) 12457-12462.
[383] H. Gao, A. Fu, S.C. Andrews, P. Yang, Cleaved-coupled nanowire lasers, Proceedings of the National Academy of Sciences of the United States of America 110(3) (2013) 865-869.
[384] J. Wright, S. Liu, G. Wang, Q. Li, A. Benz, D. Koleske, P. Lu, H. Xu, L. Lester, T. Luk, Multi-colour nanowire photonic crystal laser pixels, Scientific Reports 3(10) (2013) 2982.
[385] J. Heo, S. Jahangir, B. Xiao, P. Bhattacharya, Room-temperature polariton lasing from GaN nanowire array clad by dielectric microcavity, Nano Letters 13(6) (2013) 77-83.
[386] Q. Zhang, G. Li, X. Liu, F. Qian, Y. Li, T.C. Sum, C.M. Lieber, Q. Xiong, A room temperature low-threshold ultraviolet plasmonic nanolaser, Nature Communications 5 (2014) 4953.
[387] Y.J. Lu, C.Y. Wang, J. Kim, H.Y. Chen, M.Y. Lu, Y.C. Chen, W.H. Chang, L.J. Chen, M.I. Stockman, C.K. Shih, All-color plasmonic nanolasers with ultralow thresholds: autotuning mechanism for single-mode lasing, Nano Letters 14(8) (2014) 4381-4388.
[388] X. Wang, J. Tong, X. Chen, B. Zhao, Z. Ren, D. Li, X. Zhuo, J. Zhang, H. Yi, C. Liu, Highly ordered GaN-based nanowire arrays grown on patterned (100) silicon and their optical properties, Chemical Communications 50(6) (2013) 682-684.
[389] C. Li, S. Liu, A. Hurtado, J.B. Wright, H. Xu, T.S. Luk, J.J. Figiel, I. Brener, S.R.J. Brueck, G.T. Wang, Annular-shaped emission from gallium nitride nanotube lasers, ACS Photonics 2(8) (2015) 1025-1029.
[390] K.H. Li, Y.F. Cheung, H.W. Choi, Whispering gallery mode lasing in optically isolated III-nitride nanorings, Optics Letters 40(11) (2015) 2564-2567.
[391] H.T. Liu, H.L. Zhang, L. Dong, Y.J. Zhang, C.F. Pan, Growth of GaN micro/nanolaser arrays by chemical vapor deposition, Nanotechnology 27(35) (2016) 355201.
[392] C. Li, S. Liu, T.S. Luk, J.J. Figiel, I. Brener, S.R. Brueck, G.T. Wang, Intrinsic polarization control in rectangular GaN nanowire lasers, Nanoscale 8(10) (2016) 5682-5687.
[393] K. Kishino, S. Ishizawa, Spectrally-broadened multimode lasing based on structurally graded InGaN nanocolumn photonic crystals suitable for reduction of speckle contrast, Applied Physics Letters 109(7) (2016) F79.
[394] Y. Li, F. Qian, J. Xiang, C.M. Lieber, Nanowire electronic and optoelectronic devices, Materials

Today 9(10) (2006) 18-27.
[395] J.B. Wright, S. Campione, S. Liu, J.A. Martinez, H. Xu, T.S. Luk, Q. Li, G.T. Wang, B.S. Swartzentruber, L.F. Lester, Distributed feedback gallium nitride nanowire lasers, Applied Physics Letters 104(4) (2014) 041107.
[396] P. Berini, I.D. Leon, Surface plasmon-polariton amplifiers and lasers, Nature Photonics 6(1) (2011) 16-24.
[397] X. Duan, Y. Huang, R. Agarwal, C.M. Lieber, Single-nanowire electrically driven lasers, Nature 421(6920) (2003) 241-245.
[398] T. Frost, S. Jahangir, E. Stark, S. Deshpande, A. Hazari, C. Zhao, B.S. Ooi, P. Bhattacharya, Monolithic electrically injected nanowire array edge-emitting laser on (001) silicon, Nano Letters 14(8) (2014) 4535-4541.
[399] S. Jahangir, T. Frost, A. Hazari, L. Yan, E. Stark, T. Lamountain, J.M. Millunchick, B.S. Ooi, P. Bhattacharya, Small signal modulation characteristics of red-emitting (λ = 610 nm) III-nitride nanowire array lasers on (001) silicon, Applied Physics Letters 106(7) (2015) 391-396.
[400] K. Li, X. Liu, Q. Wang, S. Zhao, Z. Mi, Ultralow-threshold electrically injected AlGaN nanowire ultraviolet lasers on Si operating at low temperature, Nature Nanotechnology 10(2) (2015) 140-144.
[401] S. Zhao, S.Y. Woo, M. Bugnet, X. Liu, J. Kang, G.A. Botton, Z. Mi, Three-dimensional quantum confinement of charge carriers in self-organized AlGaN nanowires: A viable route to electrically injected deep ultraviolet lasers, Nano Letters 15(12) (2015) 7801-7807.
[402] S. Zhao, X. Liu, S.Y. Woo, J. Kang, G.A. Botton, Z. Mi, An electrically injected AlGaN nanowire laser operating in the ultraviolet-C band, Applied Physics Letters 107(4) (2015) 598.
[403] F.E. Osterloh, Inorganic nanostructures for photoelectrochemical and photocatalytic water splitting, Chemical Society Reviews 42(6) (2013) 2294-2320.
[404] T. Hisatomi, J. Kubota, K. Domen, ChemInform Abstract: Recent advances in semiconductors for photocatalytic and photoelectrochemical water splitting, Chemical Society Reviews 43(22) (2014) 7520-7535.
[405] M.G. Kibria, Z. Mi, Artificial photosynthesis using metal/nonmetal-nitride semiconductors: current status, prospects, and challenges, Journal of Materials Chemistry A 4(8) (2015) 2801-2820.
[406] K. Maeda, R. Kuriki, M. Zhang, X. Wang, O. Ishitani, The effect of the pore-wall structure of carbon nitride on photocatalytic CO2 reduction under visible light, Journal of Materials Chemistry A 2(36) (2014) 15146-15151.
[407] F.A. Chowdhury, Z. Mi, M.G. Kibria, M.L. Trudeau, Group III-nitride nanowire structures for photocatalytic hydrogen evolution under visible light irradiation, APL Materials 3(10) (2015) 104408.
[408] H.S. Jung, Y.J. Hong, Y. Li, J. Cho, Y.J. Kim, G.C. Yi, Photocatalysis using GaN nanowires, ACS Nano 2(4) (2008) 637-642
[409] D. Wang, A. Pierre, M.G. Kibria, K. Cui, X. Han, K.H. Bevan, H. Guo, S. Paradis, A.-R. Hakima, Z. Mi, Wafer-level photocatalytic water splitting on GaN nanowire arrays grown by molecular beam

epitaxy, Nano Letters 11(6) (2011) 2353-2357.
[410] M.G. Kibria, H.P. Nguyen, K. Cui, S. Zhao, D. Liu, H. Guo, M.L. Trudeau, S. Paradis, A.R. Hakima, Z. Mi, One-step overall water splitting under visible light using multiband InGaN/GaN nanowire heterostructures, ACS Nano 7(9) (2013) 7886-7893.
[411] M.G. Kibria, F.A. Chowdhury, S. Zhao, B. Alotaibi, M.L. Trudeau, H. Guo, Z. Mi, Visible light-driven efficient overall water splitting using p-type metal-nitride nanowire arrays, Nature Communications 6 (2015) 6797.
[412] M.G. Kibria, F.A. Chowdhury, M.L. Trudeau, H. Guo, Z. Mi, Dye-sensitized InGaN nanowire arrays for efficient hydrogen production under visible light irradiation, Nanotechnology 26(28) (2015) 285401.
[413] J.R. Bolton, S.J. Strickler, J.S. Connolly, Limiting and realizable efficiencies of solar photolysis of water, Nature 316(6028) (1985) 495-500.
[414] Z. Zhang, J.T. Yates, ChemInform Abstract: Band bending in semiconductors: chemical and physical consequences at surfaces and interfaces, Chemical Reviews 112(10) (2012) 5520-5551.
[415] M.G. Kibria, S. Zhao, F.A. Chowdhury, Q. Wang, H.P.T. Nguyen, M.L. Trudeau, H. Guo, Z. Mi, Tuning the surface Fermi level on p-type gallium nitride nanowires for efficient overall water splitting, Nature Communications 5 (2014) 3825.
[416] J.H. Yun, H.W. Cheng, C. Hahn, H.E. Jeong, P. Yang, Si/InGaN core/shell hierarchical nanowire arrays and their photoelectrochemical properties, Nano Letters 12(3) (2012) 1678-1682.
[417] J. Benton, J. Bai, T. Wang, Enhancement in solar hydrogen generation efficiency using a GaN-based nanorod structure, Applied Physics Letters 102(102) (2013) 93-96.
[418] J. Wallys, S. Hoffmann, F. Furtmayr, J. Teubert, M. Eickhoff, Electrochemical properties of GaN nanowire electrodes--influence of doping and control by external bias, Nanotechnology 23(16) (2012) 165701.
[419] B. Alotaibi, M. Harati, S. Fan, S. Zhao, H.P. Nguyen, M.G. Kibria, Z. Mi, High efficiency photoelectrochemical water splitting and hydrogen generation using GaN nanowire photoelectrode, Nanotechnology 24(17) (2013) 416-432.
[420] J. Kamimura, P. Bogdanoff, J. Lähnemann, C. Hauswald, L. Geelhaar, S. Fiechter, H. Riechert, Photoelectrochemical properties of (In,Ga)N nanowires for water splitting investigated by in situ slectrochemical mass spectroscopy, Journal of the American Chemical Society 135(28) (2013) 10242-10245.
[421] B. AlOtaibi, M. Harati, S. Fan, S. Zhao, H. Nguyen, M. Kibria, Z. Mi, High efficiency photoelectrochemical water splitting and hydrogen generation using GaN nanowire photoelectrode, Nanotechnology 24(17) (2013) 175401.
[422] B. Alotaibi, H.P.T. Nguyen, S. Zhao, M.G. Kibria, S. Fan, Z. Mi, Highly stable photoelectrochemical water splitting and hydrogen generation using a double-band InGaN/GaN core/shell nanowire photoanode, Nano Letters 13(9) (2013) 4356-4361.

[423] S. Fan, B. Alotaibi, S.Y. Woo, Y. Wang, G.A. Botton, Z. Mi, High efficiency solar-to-hydrogen conversion on a monolithically integrated InGaN/GaN/Si adaptive tunnel junction photocathode, Nano Letters 15(4) (2015) 2721-2726.
[424] J. Benton, J. Bai, T. Wang, Significantly enhanced performance of an InGaN/GaN nanostructure based photo-electrode for solar power hydrogen generation, Applied Physics Letters 103(13) (2013) 133904.
[425] J. Benton, J. Bai, T. Wang, Utilisation of GaN and InGaN/GaN with nanoporous structures for water splitting, Applied Physics Letters 105(22) (2014) 223902.
[426] L. Caccamo, J. Hartmann, C. Fàbrega, S. Estradé, G. Lilienkamp, J.D. Prades, M.W. Hoffmann, J. Ledig, A. Wagner, X. Wang, Band engineered epitaxial 3D GaN-InGaN core-shell rod arrays as an advanced photoanode for visible-light-driven water splitting, ACS Applied Materials & Interfaces 6(4) (2014) 2235-2240.
[427] M. Ebaid, J.H. Kang, S.H. Lim, Y.H. Cho, S.W. Ryu, Towards highly efficient photoanodes: The role of carrier dynamics on the photoelectrochemical performance of InGaN/GaN multiple quantum well coaxial nanowires, RSC Advances 5(30) (2015) 23303-23310.
[428] J.H. Park, A. Mandal, S. Kang, U. Chatterjee, J.S. Kim, B.G. Park, M.D. Kim, K.U. Jeong, C.R. Lee, Hydrogen generation using non-polar coaxial InGaN/GaN multiple quantum well structure formed on hollow n-GaN nanowires, Scientific Reports 6 (2016) 31996.
[429] N.U.H. Alvi, P.E.D.S. Rodriguez, P. Aseev, V.J. Gómez, A.U.H. Alvi, W.U. Hassan, M. Willander, R. Nötzel, InN/InGaN quantum dot photoelectrode: Efficient hydrogen generation by water splitting at zero voltage, Nano Energy 13 (2015) 291-297.
[430] B. Alotaibi, S. Fan, S. Vanka, M.G. Kibria, Z. Mi, A metal-nitride nanowire dual-photoelectrode device for unassisted solar-to hydrogen conversion under parallel illumination, Nano Letters 15(10) (2015) 6821-6828.
[431] S. Fan, I. Shih, Z. Mi, A monolithically integrated InGaN nanowire/Si tandem photoanode approaching the ideal bandgap configuration of 1.75/1.13 eV, Advanced Energy Materials 7(2) (2016) 1600952.
[432] Y. Wang, B. Alotaibi, F.A. Chowdhury, S. Fan, M.G. Kibria, L. Li, C.J. Li, Z. Mi, Photoelectrochemical reduction of carbon dioxide using Ge doped GaN nanowire photoanodes, APL Materials 3(11) (2015) 13518.
[433] B. Alotaibi, X. Kong, S. Vanka, S.Y. Woo, A. Pofelski, F. Oudjedi, S. Fan, M.G. Kibria, G.A. Botton, W. Ji, Photochemical carbon dioxide reduction on Mg-Doped Ga(In)N nanowire arrays under visible light irradiation, ACS Energy Letters 1(1) (2016) 246-252
[434] B. Alotaibi, S. Fan, D. Wang, J. Ye, Z. Mi, Wafer-level artificial photosynthesis for CO2 reduction into CH4 and CO using GaN nanowires, ACS Catalysis 5(9) (2015) 5342-5348.
[435] Y. Wang, S. Fan, B. Al Otaibi, Y. Wang, L. Li, Z. Mi, A monolithically integrated nanowire/Si solar cell photocathode for selective carbon dioxide reduction to methane, Chemistry-A European Journal 22(26) (2016) 8809-8813.
[436] X. Fang, Y. Bando, U.K. Gautam, C. Ye, D. Golberg, Inorganic semiconductor nanostructures

and their field-emission applications, Journal of Materials Chemistry 18(5) (2008) 509-522.

[437] R.H. Fowler, L. Nordheim, Electron emission in intense electric fields, Proceedings of the Royal Society of London A: Mathematical, Physical and Engineering Sciences, The Royal Society, 1928, 173-181.

[438] W. Sun, Y. Li, Y. Yang, Y. Li, C. Gu, J. Li, Morphology inducing selective plasma etching for AlN nanocone arrays: tip-size dependent photoluminescence and enhanced field emission properties, Journal of Materials Chemistry C 2(13) (2014) 2417-2422.

[439] Q. Wu, N. Liu, Y. Zhang, W. Qian, X. Wang, Z. Hu, Tuning the field emission properties of AlN nanocones by doping, Journal of Materials Chemistry C 3(5) (2015) 1113-1117.

[440] W. Qian, H. Lai, X. Pei, J. Jiang, Q. Wu, Y. Zhang, X. Wang, Z. Hu, Improving field emission by constructing CsI-AlN hybrid nanostructures, Journal of Materials Chemistry 22(35) (2012) 18578-18582.

[441] W. Qian, Y. Zhang, Q. Wu, C. He, Y. Zhao, X. Wang, Z. Hu, Construction of AlN-based core–shell Nanocone arrays for enhancing field emission, The Journal of Physical chemistry C 115(23) (2011) 11461-11465.

[442] Q. Zhao, S. Feng, Y. Zhu, X. Xu, X. Zhang, X. Song, J. Xu, L. Chen, D. Yu, Annealing effects on the field emission properties of AlN nanorods, Nanotechnology 17(11) (2006) S351-S354.

[443] F. Zhang, Q. Wu, X. Wang, N. Liu, J. Yang, Y. Hu, L. Yu, Z. Hu, Vertically aligned one-dimensional AlN nanostructures on conductive substrates: Synthesis and field emission, Vacuum 86(7) (2012) 833-837.

[444] Q. Zhao, J. Xu, X. Xu, Z. Wang, D. Yu, Field emission from AlN nanoneedle arrays, Applied Physics Letters 85(22) (2004) 5331-5333.

[445] Y. Tang, H. Cong, Z. Zhao, H. Cheng, Field emission from AlN nanorod array, Applied Physics Letters 86(15) (2005) 153104.

[446] Y. Tang, H. Cong, H.-M. Cheng, Field emission from honeycomblike network of vertically aligned AlN nanoplatelets, Applied Physics Letters 89(9) (2006) 093113.

[447] Q. Wang, T. Corrigan, J. Dai, R. Chang, A. Krauss, Field emission from nanotube bundle emitters at low fields, Applied Physics Letters 70(24) (1997) 3308-3310.

[448] S.-C. Shi, C.-F. Chen, S. Chattopadhyay, K.-H. Chen, L.-C. Chen, Field emission from quasi-aligned aluminum nitride nanotips, Applied Physics Letters 87(7) (2005) 073109.

[449] C. Liu, Z. Hu, Q. Wu, X. Wang, Y. Chen, W. Lin, H. Sang, S. Deng, N. Xu, Synthesis and field emission properties of aluminum nitride nanocones, Applied Surface Science 251(1) (2005) 220-224.

[450] Y. Tang, H. Cong, Z. Wang, H.-M. Cheng, Catalyst-seeded synthesis and field emission properties of flowerlike Si-doped AlN nanoneedle array, Applied Physics Letters 89(25) (2006) 253112.

[451] Y.K. Byeun, R. Telle, S.H. Jung, S.C. Choi, H.I. Hwang, The growth of one dimensional single-crystalline AlN nanostructures by HVPE and their field emission properties, Chemical Vapor Deposition 16(1-3) (2010) 72-79.

[452] C.C. Chen, C.C. Yeh, C.H. Chen, M.Y. Yu, H.L. Liu, J.J. Wu, K.H. Chen, L.C. Chen, J.Y. Peng, Y.F. Chen, Catalytic growth and characterization of gallium nitride nanowires, Journal of the American Chemical Society 123(12) (2001) 2791-2798.
[453] X. Xiang, H. Zhu, One-dimensional gallium nitride micro/nanostructures synthesized by a space-confined growth technique, Applied Physics A 87(87) (2007) 651-659.
[454] D.V. Dinh, S.M. Kang, J.H. Yang, S.W. Kim, D.H. Yoon, Synthesis and field emission properties of triangular-shaped GaN nanowires on Si(100) substrates, Journal of Crystal Growth 311(3) (2009) 495-499.
[455] D.K.T. Ng, M.H. Hong, L.S. Tan, Y.W. Zhu, C.H. Sow, Field emission enhancement from patterned gallium nitride nanowires, Nanotechnology 18(37) (2007) 14026-14029.
[456] G. Nabi, C. Cao, W.S. Khan, S. Hussain, Z. Usman, T. Mahmood, N.A.D. Khattak, S. Zhao, X. Xu, D. Yu, Synthesis, characterization, photoluminescence and field emission properties of novel durian-like gallium nitride microstructures, Materials Chemistry & Physics 133(2-3) (2012) 793-798.
[457] G. Nabi, C. Cao, W.S. Khan, S. Hussain, Z. Usman, N.A.D. Khattak, Z. Ali, F.K. Butt, S.H. Shah, M. Safdar, Preparation of grass-like GaN nanostructures: Its PL and excellent field emission properties, Materials Letters 66(1) (2012) 50-53.
[458] Z. Cui, E. Li, S. Wei, D. Ma, Optical and field emission properties of layer-structure GaN nanowires, Materials Research Bulletin 56(2) (2014) 80-85.
[459] G. Nabi, C. Cao, S. Hussain, W.S. Khan, R.R. Sagar, Z. Ali, F.K. Butt, Z. Usman, D. Yu, Synthesis, photoluminescence and field emission properties of well aligned/well patterned conical shape GaN nanorods, CrystEngComm 14(24) (2012) 8492-8498.
[460] W.S. Jang, S.Y. Kim, J. Lee, J. Park, J.P. Chan, C.J. Lee, Triangular GaN-BN core-shell nanocables: Synthesis and field emission, Chemical Physics Letters 422(1-3) (2006) 41-45.
[461] C. Lin, G. Yu, X. Wang, M. Cao, H. Lu, H. Gong, M. Qi, A. Li, Catalyst-free growth of well vertically aligned GaN needlelike nanowire array with low-field electron emission properties, The Journal of Physical Chemistry C 112(48) (2008) 18821-18824.
[462] L.T. Fu, Z.G. Chen, D.W. Wang, L. Cheng, H.Y. Xu, J.Z. Liu, H.T. Cong, G.Q. Lu, J. Zou, Wurtzite P-doped GaN triangular microtubes as field emitters, The Journal of Physical Chemistry C 114(21) (2010) 9627-9633.
[463] K.R. Wang, S.J. Lin, L.W. Tu, M. Chen, Q.Y. Chen, T.H. Chen, M.L. Chen, H.W. Seo, N.H. Tai, S.C. Chang, InN nanotips as excellent field emitters, Applied Physics Letters 92(12) (2008) 123105.
[464] L. Li, T. Zhai, Y. Bando, D. Golberg, Recent progress of one-dimensional ZnO nanostructured solar cells, Nano Energy 1(1) (2012) 91-106.
[465] Q. Zhang, H. Li, Y. Ma, T. Zhai, ZnSe Nanostructures: Synthesis, properties and applications, Progress in Materials Science 83 (2016) 472-535.
[466] H.P.T. Nguyen, Y.L. Chang, I. Shih, Z. Mi, InN p-i-n nanowire solar cells on Si, IEEE Journal of Selected Topics in Quantum Electronics 17(4) (2011) 1062-1069.
[467] J. Bai, C.C. Yang, M. Athanasiou, T. Wang, Efficiency enhancement of InGaN/GaN solar cells

with nanostructures, Applied Physics Letters 104(104) (2014) 051129.
[468] Y. Dong, B. Tian, T.J. Kempa, C.M. Lieber, Coaxial group III-nitride nanowire photovoltaics, Nano Letters 9(5) (2009) 2183-2187.
[469] A. Messanvi, H. Zhang, V. Neplokh, F.H. Julien, F. Bayle, M. Foldyna, C. Bougerol, E. Gautier, A. Babichev, C. Durand, Investigation of photovoltaic properties of single core-shell GaN/InGaN wires, ACS Applied Materials & Interfaces 7(39) (2015) 21898-21906.
[470] X.Y. Chen, C.T. Yip, M.K. Fung, A.B. Djurišić, W.K. Chan, GaN-nanowire-based dye-sensitized solar cells, Applied Physics A Materials Science & Processing 100(1) (2010) 15-19.
[471] O. Kryliouk, H.J. Park, H.T. Wang, B.S. Kang, T.J. Anderson, F. Ren, S.J. Pearton, Pt-coated InN nanorods for selective detection of hydrogen at room temperature, Journal of Vacuum Science & Technology B 23(5) (2005) 1891-1894.
[472] W. Lim, J.S. Wright, B.P. Gila, J.L. Johnson, A. Ural, T. Anderson, F. Ren, S.J. Pearton, Room temperature hydrogen detection using Pd-coated GaN nanowires, Applied Physics Letters 93(7) (2008) 072109.
[473] W. Lim, J.S. Wright, B.P. Gila, S.J. Pearton, F. Ren, W.T. Lai, L.C. Chen, M.S. Hu, K.H. Chen, Selective-hydrogen sensing at room temperature with Pt-coated InN nanobelts, Applied Physics Letters 93(20) (2008) 202109.
[474] A. Zhong, T. Sasaki, K. Hane, Platinum/porous GaN nanonetwork metal-semiconductor Schottky diode for room temperature hydrogen sensor, Sensors & Actuators A Physical 209(29) (2014) 52-56.
[475] V. Dobrokhotov, D.N. Mcilroy, M.G. Norton, A. Abuzir, W.J. Yeh, I. Stevenson, R. Pouy, J. Bochenek, M. Cartwright, L. Wang, Principles and mechanisms of gas sensing by GaN nanowires functionalized with gold nanoparticles, Journal of Applied Physics 99(10) (2006) 104302.
[476] A. Patsha, P. Sahoo, S. Amirthapandian, A.K. Prasad, A. Das, A.K. Tyagi, M.A. Cotta, S. Dhara, Localized charge transfer process and surface band bending in methane sensing by GaN nanowires, The Journal of Physical Chemistry C 119(36) (2016) 21251-21260.
[477] Z.L. Wang, J. Song, Piezoelectric nanogenerators based on zinc oxide nanowire arrays, Science 312(5771) (2006) 242-246.
[478] G. Liu, S. Zhao, R.D. Henderson, Z. Leonenko, E. Abdelrahman, Z. Mi, D. Ban, Nanogenerators based on vertically aligned InN nanowires, Nanoscale 8(4) (2016) 2097-2106.